

# Dynamic Wetting by Viscous Liquids: Effects of Softness, Wettability and Curvature of the Substrate and Influence of External Electric Fields

PhD Thesis

M. Phil. Longquan Chen | Matrikelnummer: 1606490

Maschinenbau, Technische Universität Darmstadt



TECHNISCHE  
UNIVERSITÄT  
DARMSTADT

---

# Dynamic Wetting by Viscous Liquids: Effects of Softness, Wettability and Curvature of the Substrate and Influence of External Electric Fields

Vom Fachbereich Maschinenbau  
an der Technischen Universität Darmstadt

zur

Erlangung des akademischen Grades eines Doktors der  
Ingenieurwissenschaften (Dr.-Ing.)

genehmigte

**Dissertation**

vorgelegt von

**M. Phil. Longquan Chen**

geboren in Mianyang, China

Berichterstatter: Prof. Dr.-Ing. Cameron Tropea (Technische Universität Darmstadt)

Mitberichterstatter: PD Dr.rer.nat. Elmar Bonaccorso (Technische Universität Darmstadt)

Prof. Dr. Hans-Jürgen Butt (Max-Planck-Institut für Polymerforschung)

Tag der Einreichung: 07.08.2013

Tag der mündlichen Prüfung: 19.11.2013

Darmstadt 2013

D17

---



---

## **Erklärung**

Hiermit erkläre ich, dass ich die vorliegende Arbeit, abgesehen von den in ihr ausdrücklich genannten Hilfen, selbständig verfasst habe.

Darmstadt, den 5. December 2013

Longquan Chen

---

---

## Acknowledgement

Firstly, I would like to address my formost and sincerest gratitude to my respected supervisor, PD Dr.rer.nat. Elmar Bonaccorso, for offering me the ticket to the past three years of scientific journey in his group. I appreciate him for his crucial comments and support which guided me in the right direction of research. His enormous knowledge, profound insights and enthusiastic passion of science inspired me to step forward. I am very grateful to Prof. Dr. Hans-Jürgen Butt and PD Dr. Günter Auernhammer from Max-Planck Institute for Polymer Research for their supervision as well. Their discussions and suggestions helped me to understand the research topic deeply.

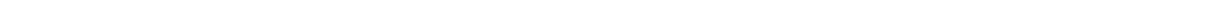
It was my great pleasure to establish collaborations with Prof. Martin E.R. Shanahan (Université Bordeaux, France), Prof. Dr. Nico van der Vegt (CSI, Technische Universität Darmstadt) and Dr. Kai Zhang (LOEWE Soft Control, Technische Universität Darmstadt). Their special view of science is interesting and I learned a lot from them. I would like to thank Prof. Dr.-Ing. Cameron Tropea and the Center of Smart Interfaces for financial support without which I could not finish my projects. Special acknowledgements are given to Prof. Zhigang Li (Hong Kong University of Science and Technology) for his encouragement in the past few years.

I acknowledge Dr. Dmytro Golovko and Dr. Lars-Oliver Heim for their help in the project of dynamic wetting of micron-sized particles. I thank Dr. Chunli Li for her simulation support of the electrospreading project. I also express my gratitude to all other members in the Experimental Interface Physics group, Xiang Wang, Marcus Lopes, Chin-Chi Hsu, Andreas Plog, Dr. Jörg Strutwolf, Oscar Leonardo Herrera Sandoval, Dr. Julien Petit, Prof. Zheng Wei and Dr. Tassilo Kaule for their support and friendship.

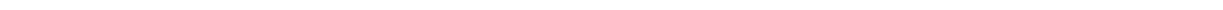
Finally, I want to give my deep thanks to my parents, my wife, Xiaoyan Peng and my cute boy, Hanwen Chen, for their unconditional dedicated love and support, which are the original power for my efforts.

---





*To my family...*



---

# Dynamic Wetting by Viscous Liquids: Effects of Softness, Wettability and Curvature of the Substrate and Influence of External Electric Fields

## Abstract

The wetting of solid surfaces by liquids is commonly observed in nature, and it is also a key to a number of industrial applications and biological processes. In the past two centuries, most studies about wetting were devoted mainly to equilibrium situations and thus to static measurements. However, in most cases the dynamic wetting is more relevant and it has received less attention. The goal of this thesis is to study the effects of softness, wettability and curvature of the substrate and influence of external electric fields on dynamic wetting of viscous liquids.

The thesis contains two main parts. The first part focuses on the early dynamic wetting of simple liquids on two types of surfaces that show different complexity: flat viscoelastic substrates and highly curved solid microparticles. On the viscoelastic substrates, a novel wetting stage dominated by inertia was found. The dynamics in this stage is characterized by the wetting radius,  $r = K't^\alpha$ , following a power law similarly as on rigid surfaces, with the exponent  $\alpha$  only depending on surface wettability. After the inertial wetting stage, spreading slows down and enters another stage dominated by the viscoelasticity of the substrate. The transition between inertial and viscoelastic stage is controlled by the surface “softness”. A simple theory was developed with Prof. Martin E.R. Shanahan to explain these findings. An early inertial wetting stage was also observed during the snap-in process, i.e. the wetting, of single colloidal particles into large water drops. The snap-in time is dependent on the capillary force and on inertia, but is independent on surface wettability. In contrast, the snap-in force is larger for hydrophilic and smaller for hydrophobic particles. A scaling model was proposed to describe the snap-in or early wetting of individual colloids.

---



---

The second part of the thesis is devoted to study the dynamic wetting of rigid flat surfaces by simple and viscous liquids. First, the early spreading of drops of aqueous electrolyte solutions on various wettable surfaces driven by electrostatic forces, which was termed “electrospreading”, was investigated. It was found that early electrospreading is only dominated by inertia and electrostatics. The wetting dynamics is not only dependent on surface wettability and applied electric potential, but also on the concentration of the electrolyte solutions. The electrostatic energy stored in the electric double layer near the solid-liquid interface served as an additional energy for driving drop spreading. Based on molecular dynamics simulation done by Dr. Chunli Li, a simple scaling model was presented to describe the wetting dynamics. Finally, a systematic study of dynamic wetting of various wettable surfaces by viscous liquids was carried out. Both surface wettability and liquid viscosity influence the inertial stage of wetting as well as the viscous stage. During the inertial wetting stage, the effective mass of the spreading drop is affected by surface wettability and liquid viscosity. This results in a slower spreading speed on hydrophobic surfaces, or of highly viscous liquids. Viscous wetting did not take place on all substrates, but only on those surfaces with equilibrium contact angles smaller than a critical value, which depended again on liquid viscosity. A scaling law was proposed to explain these experimental observations.

---

---

# Dynamic Wetting by Viscous Liquids: Effects of Softness, Wettability and Curvature of the Substrate and Influence of External Electric Fields

## Zusammenfassung

Die Benetzung fester Oberflächen durch Flüssigkeiten ist nicht nur in der Natur weit verbreitet sondern auch ein Schlüsselprozess in zahlreichen industriellen Anwendungen und biologischen Vorgängen. In den letzten zwei Jahrhunderten wurde in erster Linie die Benetzung im Gleichgewichtszustand untersucht und zu diesem Zweck statische Messverfahren eingesetzt. In vielen Fällen ist jedoch die Dynamik der Benetzung von Bedeutung, die bisher weniger untersucht wurde. Ziel meiner Arbeit ist die Untersuchung Einflusses von Weichheit, Benetzbarkeit und Wölbung des Substrats und der Einfluss eines externen elektrischen Feldes auf die dynamische Benetzung mit viskosen Flüssigkeiten.

Die Dissertation besteht aus zwei Hauptteilen. Der erste Teil beschäftigt sich mit der anfänglichen dynamischen Ausbreitung einfacher Flüssigkeiten auf zwei verschiedenen komplexen Oberflächen: Glatte, viskoelastische Oberflächen und feste Mikropartikel mit hoher Krümmung. Auf den viskoelastischen Oberflächen wurde ein neuer Benetzungsbereich gefunden, in dem das Benetzungsverhalten durch Trägheit bestimmt wird. Die Dynamik in diesem Bereich wird über den Benetzungsradius,  $r = K't^\alpha$ , charakterisiert, der einem ähnlichen Potenzgesetz wie auf festen Oberflächen folgt. Der Exponent  $\alpha$  hängt hier nur von der Benetzbarkeit der Oberfläche ab. Nach dem Trägheits-dominierten Benetzungsbereich wird die Ausbreitung langsamer und erreicht einen neuen Bereich, in dem sie durch die Viskoelastizität des Substrates kontrolliert wird. Der Übergang zwischen Trägheits- und Viskoelastizitäts-kontrolliertem Bereich wird durch die „Weichheit“ der Oberfläche bestimmt. Zusammen mit Prof. M.E.R. Shanahan wurde eine einfache Theorie zur Erklärung dieser experimentellen Ergebnisse entwickelt. Ein anfänglicher, Trägheits-kontrollierter Bereich wurde auch während des Einschnappvorgangs, d.h.

---

---

der Benetzung von einzelnen Kolloidpartikeln durch große Wassertropfen, beobachtet. Die Zeit für das Einschnappen hängt von der Kapillarkraft und der Trägheit ab, ist aber unabhängig von der Benetzbarkeit der Oberfläche. Andererseits ist Einschnappkraft für hydrophile Partikel größer als für hydrophobe. Ein Skalenmodell für die Beschreibung des Einschnappes und der anfänglichen Phasen der Benetzung einzelner Partikel wurde entwickelt.

Im zweiten Teil der Dissertation wird die dynamische Benetzung glatter, fester Oberflächen mit einfachen und viskosen Flüssigkeiten behandelt. Zuerst wurde die anfängliche Ausbreitung von Tropfen einer wässrigen Elektrolytlösung auf verschiedenen benetzbaren Oberflächen, die durch elektrostatische Kräfte getrieben wurde untersucht, ein Prozess der hier mit „Elektroausbreitung“ bezeichnet wird. Es konnte gezeigt werden, dass die anfängliche Elektroausbreitung nur durch Trägheit und Elektrostatik kontrolliert wird. Die Benetzungsdynamik hängt nicht nur von der Oberflächenbenetzbarkeit und dem angelegten elektrischen Potential, sondern auch von der Elektrolytkonzentration ab. Die gespeicherte elektrostatische Energie in der elektrischen Doppelschicht nahe der Grenzfläche zwischen Flüssigkeit und Feststoff dient als zusätzliche Energiequelle für das Ausbreiten der Tropfen. Basierend auf molekular-dynamischen Simulationen von Dr. Chunli Li wurde ein Skalenmodell zur Beschreibung der Benetzungsdynamik vorgestellt. Abschließend wurde eine systematische Untersuchung der dynamischen Benetzung vieler verschieden benetzbarer Oberflächen mit hochviskosen Flüssigkeiten durchgeführt. Es zeigte sich, dass sowohl die Oberflächenbenetzbarkeit als auch die Viskosität der Flüssigkeit sowohl den Trägheits-kontrollierten als auch den viskosen Bereich beeinflussen. Im Trägheits-kontrollierten Benetzungsbereich wird die effektive Masse des sich ausbreitenden Tropfens von der Benetzbarkeit der Oberfläche und der Viskosität der Flüssigkeit bestimmt. Dies führt zu einer geringeren Ausbreitungsgeschwindigkeit auf hydrophoben Oberflächen oder von hochviskosen Flüssigkeiten. Viskose Benetzung trat nicht auf allen Substraten, sondern nur auf solchen auf, die Gleichgewichts-Kontaktwinkel unterhalb eines kritischen Wertes hatten. Dieser kritische Wert hängt wiederum von der Viskosität der Flüssigkeit ab. Auch hier wurde ein Skalengesetz zur Erklärung der experimentellen Daten vorgeschlagen.

---

---

## Contents

<b>Lists of Figures</b> .....	IV
<b>Lists of Tables</b> .....	X
<b>List of Symbols and Abbreviations</b> .....	XI
<b>1 Brief Introduction about Wetting</b> .....	1
1.1 Surface tension and interfacial tensions .....	1
1.2 Laplace equation .....	3
1.3 Sessile drops on surfaces .....	3
1.3.1 Sessile drops on rigid surfaces.....	3
1.3.2 Sessile drops on soft substrates or surfaces .....	9
1.4 Dynamic wetting .....	11
1.4.1 Dynamic wetting on rigid surfaces .....	11
1.4.2 Dynamic wetting on soft substrates .....	17
 <b>Part I Effects of Substrate Softness and Curvature on Dynamic Wetting</b>	
<b>2 Early Dynamic Wetting on Soft Substrates</b> .....	19
2.1 Motiviatiion.....	19
2.2 Experiments .....	20
2.2.1 Soft substrates.....	20
2.2.2 Liquids .....	24
2.2.3 Experimental setup .....	25
2.2.4 Data analysis .....	26
2.3 Experimental results and discussion .....	26
2.3.1 Spreading process .....	26
2.3.2 Inertial wetting .....	29
2.3.3 Inerial wetting exponent .....	31
2.3.4 Inertial wetting time on “soft” PDMS substrates.....	33

---

2.3.5	Inertial wetting time on “rigid” PDMS surfaces .....	36
2.3.6	Effects of film thickness.....	38
2.4	Theoretical model.....	39
2.4.1	Inertial wetting .....	40
2.4.2	Viscoelastic wetting .....	42
2.4.3	Inertial to viscoelastic transition.....	44
2.5	Summary.....	47
<b>3</b>	<b>Dynamic Wetting of Micron-sized Particles.....</b>	<b>49</b>
3.1	Motivation.....	49
3.2	Experiments .....	50
3.2.1	Hydrophilic and hydrophobic colloidal probes .....	50
3.2.2	Spring constant of cantilevers .....	52
3.2.3	Experimental setup .....	54
3.3	Experimental results and discussion .....	55
3.3.1	The dynamic wetting/snap-in process .....	55
3.3.2	Snap-in time.....	59
3.3.3	Snap-in force.....	61
3.4	Summary.....	63
<b>Part II Effects of Surface Wettability, Liquid Viscosity and External Electric Field on Dynamic Wetting</b>		
<b>4</b>	<b>Early Dynamic Electrowetting of Aqueous Electrolyte Drops.....</b>	<b>64</b>
4.1	Motivation.....	64
4.2	Experiments .....	65
4.2.1	Surfaces .....	65
4.2.2	Liquids .....	66
4.2.3	Experimental setup .....	67

---

4.2.4	Drop spreading experiments and data analysis.....	67
4.3	Experimental results.....	68
4.3.1	Early spreading on randomly charged surface.....	68
4.3.2	Early spreading under electric potential.....	70
4.3.3	Drop recoiling.....	72
4.4	MD Simulation from CPC.....	73
4.4.1	MD Simulation method.....	73
4.4.2	Spreading of electrolyte nanodrops.....	74
4.4.3	Electric double layer near the interface.....	76
4.5	Scaling model.....	78
4.6	Summary.....	81
<b>5</b>	<b>Effects of Surface Wettability and Liquid Viscosity on Dynamic Wetting.....</b>	<b>82</b>
5.1	Motivation.....	82
5.2	Experiments.....	83
5.2.1	Surfaces and liquids.....	83
5.2.2	Observation of the wetting process.....	84
5.2.3	Data analysis.....	84
5.3	Results and discussion.....	86
5.3.1	Effects of surface wettability.....	86
5.3.2	Effects of liquid viscosity.....	87
5.3.3	Inertial wetting.....	87
5.3.4	Viscous wetting.....	93
5.4	Summary.....	96
<b>6</b>	<b>Conclusion.....</b>	<b>97</b>
<b>7</b>	<b>References.....</b>	<b>XCIX</b>
<b>8</b>	<b>Curriculum Vitae.....</b>	<b>CVII</b>

---

---

## Lists of Figures

---

Figure 1-1 A steel needle floats on the surface of water due to surface tension.....	1
Figure 1-2 Sketch of the molecular organization at the interface. The arrows are illustrations of intermolecular interactions. ....	2
Figure 1-3 Water drops sitting on a silicon surface with size $R_0 < 2.7 \text{ mm}$ (a)-(b) and with $R_0 > 2.7 \text{ mm}$ (c). The scale bar is 2.7 mm. The dashed line shows the spherical fittings and the dashed line denotes the solid surface.....	4
Figure 1-4 Sketch of a drop sitting on the solid substrate in its equilibrium state. ....	4
Figure 1-5 Schematic of advancing contact angle (a) and receding contact angle (b). The red dashed lines indicate the initial equilibrium shapes.....	6
Figure 1-6 A drop rests on a rough surface (a) and on a chemical heterogeneous surface (b). (c) The drop rests on top of the asperities (Cassie-Baxter state).....	7
Figure 1-7 Schematic of the zone near the three-phase contact line. The macroscopic spherical cap is connected to a thin film covering the substrate. ....	8
Figure 1-8 Schematic of the deformation induced by surface tension $\gamma$ and Laplace pressure $\Delta P$ on a bulk soft substrate (a) and on a thin soft film supported by a rigid substrate (b). ....	10
Figure 1-9 The initial state of a drop touching a solid surface.....	11
Figure 1-10 (a) Water droplets spread on four surfaces with different wettability. (b) Spreading radius vs. time for the spreading process in (a). The initial radius of all drops was $R_0 = 0.6 \text{ mm}$ . ....	12
Figure 1-11 Log-log plot of the experimental data in Figure 1-10b. ....	13
Figure 1-12 Spreading flow near the wedge of the drop for $\theta \ll 1$ .....	14
Figure 1-13 Schematic representation of the molecular-kinetic model of wetting.....	17
Figure 2-1 The thickness of PDMS film as a function of spin-coating rate. ....	20
Figure 2-2 Sketch of the measurement cell of the homemade piezo-rheometer [67].	21
Figure 2-3 (a) Plot of shear modulus $G$ of PDMS with different monomer/cross-linker ratios as a function of frequency $f$ . (b) The corresponding phase angle $\delta$ of PDMS in (a) as a function of frequency $f$ .....	22

Figure 2-4 Shear modulus $G$ and phase angle $\delta$ for five PDMS samples at 1Hz. Solid lines are guides for the eye.....	23
Figure 2-5 Plot of shear modulus $G$ as a function of frequency $f$ . .....	24
Figure 2-6 Setup for drop spreading experiments. ....	25
Figure 2-7 Spreading of 1.0 mm-radius water drop on five substrates with different softness: (a) hydrophobic glass surface, (b) PDMS substrate with $G = 204$ kPa, (c) PDMS substrate with $G = 5.8$ kPa, and (d) PDMS substrate with $G = 0.02$ kPa. The scale bar is 1.0 mm.....	27
Figure 2-8 (a) Spreading radius $r$ as a function of spreading time $t$ of the wetting of 1.0 mm-radius water drop on four surfaces in Fig. 2-7. (b) Log-log representation of the experimental data in (a) and the corresponding Pearson product-moment correlation coefficient, $\zeta$ , of $\log r$ and $\log t$ as a function of time (color solid lines). The black dashed lines are power law fittings and the color dashed lines show the different transition time $\tau_T$ or $\tau$ .....	28
Figure 2-9 (a) Plot of $r$ vs. $t$ for the fast wetting process of three drop sizes. (b) Rescaling of the plot by drop radius $R_0$ and characteristic inertial time $\tau_i = \sqrt{\frac{\rho R_0^3}{\gamma}}$ . The inset figure is the plot in log-log scale.....	30
Figure 2-10 Normalized spreading radius, $r/R_0$ , vs. the normalized spreading time, $t/(\mu R_0 \gamma)$ .....	31
Figure 2-11 (a) $\alpha$ for various liquids spreading on different soft substrates. (b) $\alpha$ plotted as a function of contact angle $\theta_{eq}$ .....	32
Figure 2-12 The equilibrium shape of water drops on the substrates with $G = 0.02$ , 5.8 and 204 kPa. ....	33
Figure 2-13 Transition times $\tau_T$ as function of $G$ and $\gamma$ for various liquid surface tensions on soft substrates (left) and inertial wetting times $\tau$ on hydrophobic glass for three different liquids (right). ....	34
Figure 2-14 Vertical component of surface tension force $\gamma_{\perp}$ during wetting on two soft substrates (a) $G = 0.02$ kPa and (b) $G = 5.8$ kPa. The radius of the drop is 1.0	



---

mm. The dashed and solid arrows indicate the time to reach the maximum $\gamma_{\perp}$ and the end of inertial wetting time between which $\Delta\tau$ is defined.....	35
Figure 2-15 The actual inertial time $\tau$ of various liquids is plotted as a function of the characteristic inertial time $\tau_i$ . The slope of the linear fitting is $2.6 \pm 0.14$ . ....	38
Figure 2-16 (a) The inertial exponent $\alpha$ of 1.0 mm-radius water drop spreading on PDMS films with three different thickness. The corresponding inertial wetting time $\tau_T$ is shown in (b).....	39
Figure 2-17 Schematic of a spreading drop on a surface with relevant notation. ....	40
Figure 2-18 Zoom-in view of the moving contact line on soft substrate. ....	42
Figure 2-19 (a) Spreading radii of water drops (colour symbols) on different viscoelastic substrates and asymptotic fits to the inertial (solid lines) and viscoelastic (dashed lines) parts of the curves. Only each 10 <sup>th</sup> data point is shown; (b) comparison of all calculated and measured $\tau_T$ as function of $G$ .....	46
Figure 3-1 The processes of putting particles on cantilevers.....	51
Figure 3-2 SEM image of a glass particle with radius $\sim 86 \mu\text{m}$ glued onto a cantilever. The picture in the inset was taken on the surface of the particle. ....	51
Figure 3-3 An inelastic bending of a soft cantilever with $k \approx 0.004 \text{ N/m}$ . The particle radius is $\sim 86 \mu\text{m}$ . ....	52
Figure 3-4 Schematic of the measurement of spring constant of colloidal probe. (a) The colloidal probe is pushed against the reference cantilever. (b) The colloidal probe is pushed against a rigid substrate.....	53
Figure 3-5 Schematic of the reversed particle interaction apparatus. ....	54
Figure 3-6 Snap-in process of a hydrophilic glass particle with radius of $\sim 60 \mu\text{m}$ at the water-air interface.....	55
Figure 3-7 Cantilever deflection versus time during wetting for a hydrophilic (black symbols) and a hydrophobic (red symbols) particle. (a) Particle wetting process from $t = 0$ to 6 s, showing a fast and a slow process; (b) Zoom-in from $t = 0$ to 100 ms, showing the start of the slow wetting process for $t > 1$ ms and the damped oscillations of the drop interface with a frequency $f_{Drop} \approx 200 \text{ kHz}$ ; (c) Zoom-in from $t = 0$ to 3 ms, showing the fast wetting process for $t < 1$ ms and	

---

the cantilever oscillations with a frequency $f_{CL} \approx 5$ kHz. The particle radius is $\sim 60 \mu\text{m}$ and the spring constant of the cantilever is $\sim 3.0$ N/m.....	57
Figure 3-8 Top: (a)-(f) Schematic of the snap-in process of a particle by the water-air interface. $U$ indicates the velocity of the particle. (g) Zoom in the initial contact area between the particle and water drop in (b). Bottom: Cantilever deflection versus time during the fast snap-in processes for a hydrophilic (black line) and a hydrophobic (red line) particle. The particle radius is $\sim 60 \mu\text{m}$ and the cantilever spring constant is $\sim 3.0$ N/m. The inset shows the snap-in time $t_s$ in more detail.....	58
Figure 3-9 The snap-in time $t_s$ of hydrophilic/hydrophobic particles with various sizes is plotted as a function of the characteristic inertial time $\tau_i$ . The solid line is the best fitting line with a slop of $1.2 \pm 0.13$ . The inset shows the relevant parameters. ....	61
Figure 3-10 Snap-in force of hydrophilic/hydrophobic particles measured with two types of cantilevers with different stiffness as a function of particle radius $R$ . The black and red solid lines represent the scaling capillary force $\gamma R \cos^2(\frac{\theta}{2})$ for hydrophilic and hydrophobic particles, respectively. ....	63
Figure 4-1 Sketch of the setup: a drop of initial radius $R_0$ hangs from a needle with inner radius $r_n = 400 \mu\text{m}$ . The needle is at a distance $d = 2$ mm from the surface. Between the needle and the surface a potential $\phi$ is applied.....	67
Figure 4-2 High-speed video images of water drops spreading on completely wetting (a) charged glass and (b) uncharged glass. The last image in Figure. 4-2 a&b is the zoom-in view of the initial contact area. $\beta$ is the angle formed between conical lower end of the drop and the glass surface. The scale bar is 1 mm. ...	68
Figure 4-3 Log-log plots of water drop spreading radius $r$ vs. spreading time $t$ of Figs. 4-2a and 4-2b.....	69
Figure 4-4 The spreading radius $r$ of a pure water drop vs. time $t$ (log-log scale) on a completely wetting surface for $\phi = 0, 50, 100, 200, 400$ V.....	70

---

Figure 4-5 (a) Exponent $\alpha'$ as function of the applied voltage $\phi$ for four wettable surfaces and for five aqueous electrolyte concentrations. (b) Relationship between exponent $\alpha$ and the wettability of the surfaces $\phi=0$ V. ....	71
Figure 4-6 A water drop recoils after contact with the surface with $\phi = 800$ V.....	72
Figure 4-7 Log-log plot of spreading radius $r$ vs. $t$ for the wetting case in Figure 4-6.	72
Figure 4-8 Snapshots of aqueous electrolyte nanodrops spreading on silicon surface without (a) and with (b) external electric field. Blue particles are $\text{Na}^+$ ions and green particles are $\text{F}^-$ ions.....	74
Figure 4-9 Spreading radius $r$ vs. spreading time $t$ : equilibrium of the drop reached after $\sim 600$ ps (a) without electric field ( $r_{eq} \approx 6.3$ nm) and (b) with electric field of $0.1$ V/nm ( $r_{eq} \approx 6.9$ nm). The two dashed black lines separate the regions of inertial spreading (I), viscous spreading (II), and equilibrium (III). The other lines are power law fits of the spreading radius. ....	75
Figure 4-10 Schematic of the electric double layer (left) and the corresponding electric potential (right) near a negatively charged surface. ....	76
Figure 4-11 Number density distribution of $\text{Na}^+$ (square) and $\text{F}^-$ (circle) in a water nanodrop with respect to the distance $d$ to the silicon surface at equilibrium, with (dashed lines) and without (solid lines) an applied electrical field of $0.1$ V/nm.....	77
Figure 4-12 $\alpha'^2 - \alpha^2$ vs. $\phi^2$ . , replotted from Fig. 4-5a with corresponding symbols. For clarity of representation, differently colored data sets are offset vertically by the value of $0.1$ . ....	80
Figure 5-1 Spreading radius $r$ and the linear correlation coefficient $\zeta$ between $\log r$ and $\log t$ as a function of time $t$ . The substrate is silicon oxide and the drop is water with $R_0 \approx 1.2$ mm. ....	85
Figure 5-2 Log-log plot of spreading radius $r$ as a function of time $t$ of water drops on five wettable surfaces. Drop radius was always $R_0 \approx 0.9$ mm. ....	86
Figure 5-3 Log-log plot of spreading radius $r$ as a function of time $t$ of various liquids on a partial surface ( $\theta_{eq} \approx 63^\circ$ ). Drop radius was always $R_0 \approx 0.9$ mm. ....	87
Figure 5-4 $\alpha$ as a function of $\theta_{eq}$ for drops with five different viscosity and three sizes.	88

---

Figure 5-5 (a)-(c) coefficient of power law $K'$ as function of $\theta_{eq}$ and $\mu$ for three drop sizes. (d) Normalized inertial coefficient $C$ as a function of $\theta_{eq}$ and $\mu$ . The dashed lines are guides for the eye.....	89
Figure 5-6 Schematic of the change of the drop surface profile during spreading. ....	90
Figure 5-7 (a) The extension of the velocity field $l$ as a function of spreading time $t$ for water on various wettable surfaces. (b) The extension of the velocity field $l$ as a function of spreading time $t$ for different liquids on a completely wetting surface. The dashed colour lines in (a) and (b) indicate the maximum length scale $l_M$ . (c) The time $t_M$ needed to reach the maximum length scale as a function of $\theta_{eq}$ and liquid viscosity. (d) $l_M$ as a function of $\theta_{eq}$ and liquid viscosity. Drop radius was always $R_0 \approx 0.9$ mm.....	91
Figure 5-8 (a) Inertial wetting time $\tau$ as a function of $\theta_{eq}$ for four liquids with different viscosity on completely wetting surfaces. The drop size $R_0$ is 1.2 mm (b) $\tau$ as a function of $\tau_i$ for various liquids with different drop sizes.....	93
Figure 5-9 Wetting phase diagram of drops spreading on solid surfaces as a function of liquid viscosity $\mu$ and equilibrium contact angle $\theta_{eq}$ . Symbol shapes indicate different drop size $R_0$ : (■, □) 1.2 mm, (●, ○) 0.9 mm and (▲, Δ) 0.5 mm. The open symbols denote that one stage was observed and the closed symbols denote that two stages were observed. The red dashed line represents $\theta_C = \sin^{-1} \frac{2\varepsilon_{ac}}{1+\varepsilon_{ac}^2}$ .....	95

---

---

## Lists of Tables

---

Table 2-1 Physical properties and contact angles on rigid PDMS ( $G=510$ kPa @ 1Hz) of droplets of various liquids. ....	25
Table 2-2 The fitting parameters for water, 60% glycerol/water and 10% ethanol/water drops spreading on PDMS substrates. ....	48
Table 4-1 Equilibrium, advancing, and receding contact angles of water on the four silicon substrates modified by different silanes.....	66
Table 4-2 Properties of the five electrolyte solutions. The electrical permittivity as a function of electrolyte concentration was calculated with an empirical expression from Ref.137.....	66
Table 4-3 The thickness of the electric double layer for five aqueous NaF solutions...	77
Table 5-1 Physical properties of the liquids and corresponding equilibrium contact angles on substrates modified by different types of coatings. ....	84

---



---

## List of Symbols and Abbreviations

---

$A$ surface area (m <sup>2</sup> )	$L_C$ capillary length (m)
$A_{ac}$ actual surface area (m <sup>2</sup> )	$L$ length (m)
$A_H$ Hamaker constant (J)	$L^*$ characteristic length (m)
$A_{pr}$ projected surface area (m <sup>2</sup> )	$m_P$ mass of particle (kg)
$c$ concentration (mol/kg)	$m$ mass (kg)
$C'$ capacitance per unit area (F/m <sup>2</sup> )	$\Delta M_P$ momentum (N·s)
$C_{ref}$ sensitivity with pushing the reference cantilever	$n$ number of the molecules
$C_R$ sensitivity with pushing a rigid edge	$\Delta P$ Laplace pressure (Pa)
$d$ thickness (m)	$r$ spreading radius (m)
$d_{EDL}$ thickness of the electric double layer (m)	$r_{eq}$ equilibrium contact radius (m)
$D$ cantilever deflection (m)	$R_0$ initial drop size (m)
$E$ free energy (J)	$R^*$ characteristic spreading radius (m)
$f$ frequency (Hz)	$Re$ Reynolds number
$f_i$ solid fraction of component $i$	$t$ spreading time (s)
$F_C$ capillary force (N)	$t_S$ snap-in time (s)
$F_S$ snap-in force (N)	$T$ absolute temperature (K)
$g$ gravitational acceleration (m/s <sup>2</sup> )	$V$ volume (m <sup>3</sup> )
$G$ shear modulus (Pa)	$u$ spreading velocity (m/s)
$G'$ storage modulus (Pa)	$U$ spreading speed (m/s)
$G''$ loss modulus (Pa)	$U^*$ characteristic velocity (m/s)
$G_u$ unrelaxed shear modulus (Pa)	$\phi$ applied potential (V)
$G_r$ relaxed shear modulus (Pa)	$v$ vertical velocity (m/s)
$h$ height (m)	$V^*$ characteristic vertical velocity (m/s)
$H^*$ characteristic height (m)	$w$ width (m)
$k$ spring constant (N/m)	$\theta$ dynamic contact angle
$k_B$ Boltzmann constant (J/K)	$\theta_{Ad}$ advancing contact angle
$k_{ref}$ spring constant of reference cantilever (N/m)	$\theta_C$ critical contact angle
	$\theta_{CB}$ Cassie-box angle
	$\theta_{eq}$ equilibrium contact angle
	$\theta_H$ contact angle hysteresis

$\theta_{Re}$ receding contact angle	$\varepsilon_{i-j}$ Lennard-Jones well depth (J/mol)
$\theta_W$ Wenzel contact angle	$\varepsilon_0$ permittivity of vacuum (F/m)
$\theta_Y$ Young's angle	$\varepsilon_l$ relative permittivity of liquid (F/m)
$\tau_T$ inertial wetting time on soft substrates (s)	$\sigma_{i-j}$ Lennard-Jones size parameter (m)
$\tau$ inertial wetting time on rigid surfaces (s)	$\mu$ viscosity (Pa·s)
$\tau_i$ characteristic inertial time (s)	$\alpha$ wetting exponent
$\tau_v$ characteristic viscous time (s)	$\alpha'$ electrospreading exponent
$\tau_R$ relaxation time (s)	$\lambda$ molecular displacement (m)
$\gamma$ surface tension (N/m) or (J/m <sup>2</sup> )	$\lambda_c$ wave length (m)
$\gamma_{LS}$ liquid-solid interfacial tension (N/m) or (J/m <sup>2</sup> )	$\delta$ phase angle
$\gamma_{SG}$ solid-gas interfacial tension (N/m) or (J/m <sup>2</sup> )	$\omega$ angular frequency (rad/s)
$\rho$ liquid density (kg/m <sup>3</sup> )	$\beta$ cone angle
$\rho_P$ density of particle (kg/m <sup>3</sup> )	EDL electric double layer
$\rho_C$ density of cantilever (kg/m <sup>3</sup> )	$\zeta$ Pearson product-moment correlation coefficient
$\epsilon$ roughness factor	IPIA inverted particle interaction apparatus
$\epsilon$ cutoff length (m)	CPC Computational Physical Chemistry Group
$\epsilon_a$ drop aspect ratio	MD Molecular Dynamics
$\epsilon_{ac}$ critical drop aspect ratio	MKT Molecular Kinetic Theory
	LSM least square method

---

# 1 Brief Introduction about Wetting

---

Wetting of solid surfaces by liquids is one of the most common phenomena in our daily life, from taking a bath in the morning, to washing dishes after dinner, to painting a wall, and so on. Actually, wetting also plays a key role for many industrial applications, such as oil recovery, drainage of water from highways, cooling of industrial reactors, printing, and ink-jet printing. Moreover, wetting is very crucial for biological systems as well. For example, the liquid thin film between the toe-pad of a tree frog and a surface generates an attractive capillary interaction, by which the frog can adhere and move along various surfaces. Thus, understanding the underlying physics of wetting at the liquid-solid-vapor interfaces can improve our life quality and help technological development. The aim of this chapter is to give a brief introduction on the basics of wetting. Specifically, I will first introduce the concept of interfacial tensions, then discuss static wetting, and finally dynamic wetting.

---

## 1.1 Surface tension and interfacial tensions

---

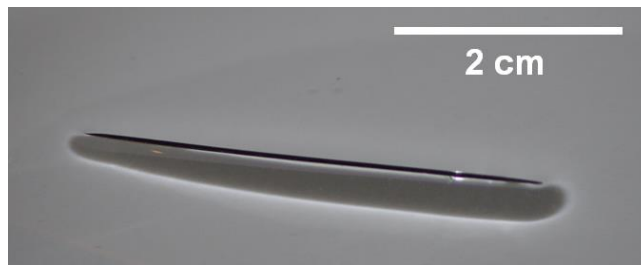


Figure 1-1 A steel needle floats on the surface of water due to surface tension.

Surface tension is an important physical property of liquids and it is responsible for all wetting phenomena. One beautiful phenomenon owing to the surface tension of water is that some small objects - though with high density like a steel needle - (Fig. 1-1), can float on the surface of water. The unit of surface tension ( $\gamma$ ) is force per unit length (N/m) or equivalently energy per unit area ( $\text{J/m}^2$ ). As a result, the surface tension can be understood from both mechanical and thermodynamic points of view.

*Mechanical explanation.* The origin of surface tension is due to the cohesive forces among liquid molecules. Here, we consider a liquid drop in a vapor ambient. In



the bulk liquid, each molecule is attracted by neighbor molecules in all directions, which leads to a net force of zero (Fig. 1-2). In contrast, at the interface of the liquid with the surrounding vapor, the attraction force between liquid molecules and gas molecules is much weaker than the cohesive force among liquid molecules, which results in a net force at the interface pointing inwards. This force on a unit length is surface tension, and it drives the interface to minimize its total area.

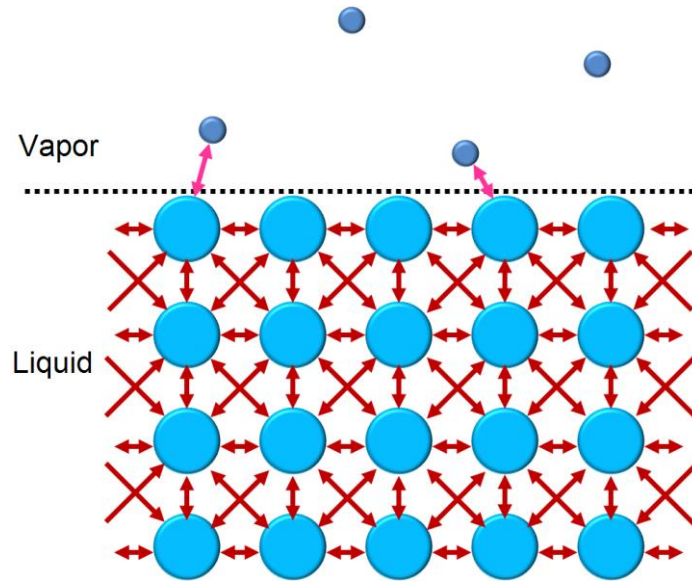


Figure 1-2 Sketch of the molecular organization at the interface. The arrows are illustrations of intermolecular interactions.

*Thermodynamic explanation.* Surface tension can also be interpreted in terms of free energy. Inside the liquid, each liquid molecule is surrounded by others from any direction, and thus it stays in the lowest state of free energy. In contrast, at the interface, half of the neighbors are missing for a liquid molecule compared to the one in the bulk liquid, which results in a higher free energy. Therefore, the surface tension can be defined as the increase of free energy  $E$  by the increase unit of surface area  $A$ , while other parameters are constant [1]:

$$\gamma = \left[ \frac{\partial E}{\partial A} \right]_{T,V,n} \quad (1.1)$$

where  $T$  is the absolute temperature,  $V$  is the volume of the system and  $n$  is the total number of molecules. In the course of thermodynamics, equation (1.1) can be used to define any interfacial tension, such as the two other interfacial tensions encountered

---

in wetting: the liquid-solid interfacial tension  $\gamma_{LS}$  and the solid-vapor interfacial tension  $\gamma_{SV}$ .

---

## 1.2 Laplace equation

---

Due to surface tension, a liquid drop in air or a gas bubble in a liquid tends to adopt a spherical shape to minimize its total surface energy. Due to the curved interface a pressure difference is generated across the interface between the “inside” and the “outside” of a drop or a bubble. This pressure difference was considered by Laplace in 1805 [2]. Thus, it is called *Laplace pressure* and takes the form

$$\Delta P = \frac{2\gamma}{R_0} \quad (1.2)$$

where  $R_0$  is the radius of the drop/bubble. Equation (1.2) indicates that the smaller the drop/bubble is, the bigger is the pressure difference. The derivation of equation (1.2) can be done with the principle of virtual work. Considering the interface of a spherical drop/bubble (initial radius is  $R_0$ ) moves a small distance of  $\delta R_0$ , the change of total energy is from the mechanical work done by the pressure and the change of surface energy,  $\delta E = \Delta P dV + \gamma dA$ . Where  $dV = 4\pi R_0^2 dR_0$  and  $dA = 8\pi R_0 dR_0$ . At equilibrium, the change of the total energy equals zero and equation (1.2) is obtained. The general form of Laplace pressure is

$$\Delta P = \gamma \left( \frac{1}{R_1} + \frac{1}{R_2} \right) \quad (1.3)$$

Here,  $R_1$  and  $R_2$  are the principle radii of curvature.

---

## 1.3 Sessile drops on surfaces

---

---

### 1.3.1 Sessile drops on rigid surfaces

---

When a liquid drop is brought into contact with a solid surface, the drop spreads on the surface to minimize the free energy of the whole system. Eventually, the drop sits on the surface in a minimum energy state, as shown in Fig. 1-3 (in this case, a water drop on a silicon surface). There are two properties of the final state.

First, the shape of the liquid-vapor interface is approximated as a truncated sphere (or spherical cap, Fig. 1-3a-b) if gravity can be neglected, i.e. the surface force

is larger than the gravity. This is due to surface tension, as discussed in the previous section. For a drop with a radius  $R_0$ , the surface force is proportional to  $\gamma R_0$  and gravity scales as  $\rho g R_0^3$ . One finds that the surface force dominates if

$$R_0 < L_C = \sqrt{\frac{\gamma}{\rho g}} \quad (1.4)$$

where  $\rho$  is the liquid density and  $g$  is the acceleration due to gravity.  $L_C$  is the so called *capillary length*. For water at room temperature and standard pressure,  $L_C \approx 2.7$  mm. Drops larger than  $L_C$  form puddles flattened by gravity (Fig. 1-3c).

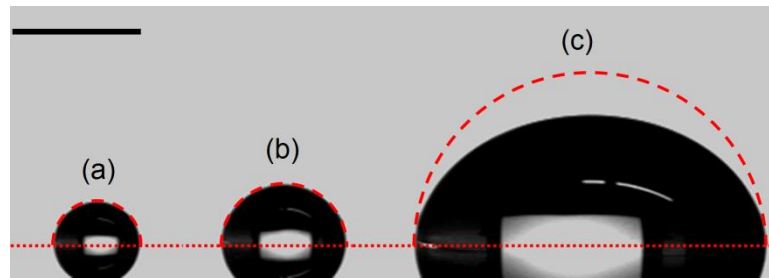


Figure 1-3 Water drops sitting on a silicon surface with size  $R_0 < 2.7$  mm (a)-(b) and with  $R_0 > 2.7$  mm (c). The scale bar is 2.7 mm. The dashed line shows the spherical fittings and the dotted line denotes the solid surface.

The second property is that the drop wets the surface with a contact radius  $r_{eq}$ .  $r_{eq}$  is the distance between the center of the drop and the triple phase contact line (TPCL) where solid-liquid-vapor meet (see Fig. 1-4). It is a parameter characterizing the interaction between the liquid and surface. If the volume of drops is similar, a large  $r_{eq}$  indicates that the liquid “likes” the surface and a small  $r_{eq}$  means the liquid “hates” the surface. However, if the volume of drops is different, it is more difficult to compare the interaction between drops and surfaces.

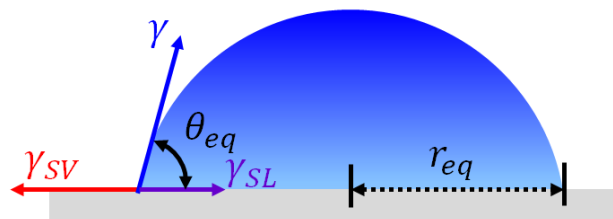


Figure 1-4 Sketch of a drop sitting on the solid substrate in its equilibrium state.

The widely accepted parameter that is normally used to describe the wettability of surfaces is the *contact angle*  $\theta$ . The contact angle is defined as the angle at which a liquid-vapor interface meets with the solid surface. It is only determined by the liquid-vapor ( $\gamma$ ), solid-vapor ( $\gamma_{SV}$ ) and liquid-solid ( $\gamma_{LS}$ ) interfacial tensions (Fig. 1-4). While the drop is in the equilibrium state, the net force due to these three interfacial tensions in the horizontal plane is zero and *Young's equation* [3] is obtained,

$$\cos \theta_{eq} = \frac{\gamma_{SV} - \gamma_{SL}}{\gamma} \quad (1.5)$$

where  $\theta_{eq}$  denotes the equilibrium contact angle. Equation (1.5) is only valid for ideal surfaces, which are rigid, smooth at the atomic scale, and chemically homogenous.

For a small drop ( $R_0 < L_C$ ) in equilibrium on a surface, one can relate the equilibrium contact radius  $r_{eq}$  to the equilibrium contact angle  $\theta_{eq}$  with

$$r_{eq} = R_0 \sin \theta_{eq} \left[ \frac{4}{(1 - \cos \theta_{eq})^2 (2 + \cos \theta_{eq})} \right]^{1/3} \quad (1.6)$$

Taking the limit  $\theta_{eq} \rightarrow 0^\circ$ , one finds  $r_{eq} \rightarrow \infty$ , which means that the interaction of liquid and surface is so strong that the liquid tends to wet the surface completely. If  $\theta_{eq} \rightarrow 180^\circ$ , one obtains  $r_{eq} \rightarrow 0$ , which reflects that the surface extremely repels the liquid. Therefore, one can use  $\theta_{eq}$  to define the degree of surface wettability. Indeed, a solid surface is called hydrophilic when the water contact angle  $\theta_{eq}$  is smaller than  $90^\circ$  [1]. If the water contact angle  $\theta_{eq} > 90^\circ$ , the solid surface is called hydrophobic [4]. In recent years, surfaces with water contact angle larger than  $150^\circ$  have been defined as superhydrophobic surfaces [5].

### *Drops on Physical or Chemical Heterogeneous Surfaces*

In nature, surfaces are not ideal. They are normally decorated by physical structures or different chemical moieties. The physical or chemical heterogeneity of real surfaces leads to the so called *contact angle hysteresis*. As sketched in Fig. 1-5a, the contact angle measured when the maximum volume of liquid is added to the drop without the contact radius increasing, is called advancing contact angle,  $\theta_{Ad}$ .  $\theta_{Ad}$  has a value equal to or larger than  $\theta_{eq}$ ,  $\theta_{Ad} \geq \theta_{eq}$ . On the other hand, the contact angle measured as the maximum volume is withdrawn from the drop without the contact

line retreating is defined as receding contact angle,  $\theta_{Re}$ , and  $\theta_{Re} \leq \theta_{eq}$  (Fig. 1-5b). The contact angle hysteresis,  $\theta_H$ , is the difference between the advancing and receding contact angle [6]

$$\theta_H = \theta_{Ad} - \theta_{Re} \quad (1.7)$$

The contact angle hysteresis characterizes the homogeneity of surfaces. The larger the value of  $\theta_H$  the more heterogeneous the surface is.

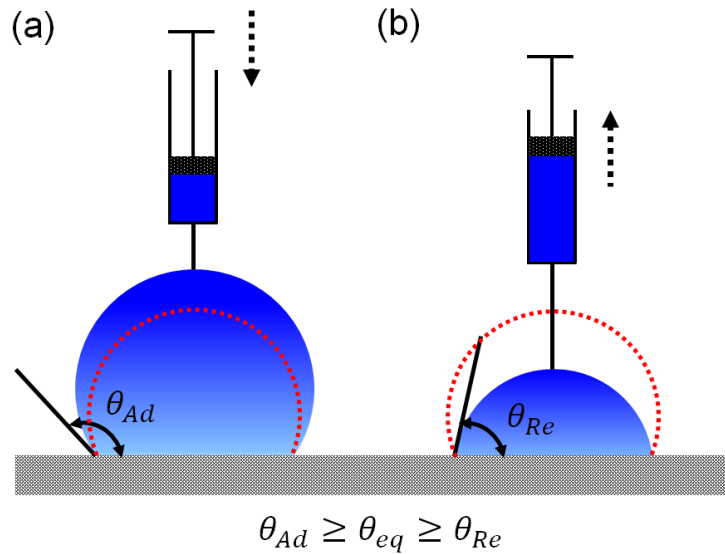


Figure 1-5 Schematic of advancing contact angle (a) and receding contact angle (b). The red dotted lines indicate the initial equilibrium shapes.

Since Young's equation is only valid for ideal surfaces, it cannot be used to predict precisely equilibrium contact angles on real surfaces. Wenzel was probably the first to modify Young's equation by considering surface roughness [7]. He considered the contribution of surface energy due to roughness and introduced a roughness factor  $\epsilon$  - which is the ratio of actual surface area ( $A_{ac}$ ) and projected surface area ( $A_{pr}$ ) - into Young's equation. Wenzel's equation takes the form

$$\cos \theta_W = \epsilon \frac{\gamma_{SV} - \gamma_{SL}}{\gamma} = \epsilon \cos \theta_Y, \quad \text{with } \epsilon = A_{ac}/A_{pr} \quad (1.8)$$

The roughness factor,  $\epsilon$ , normally has a value larger than 1 (for flat surface,  $\epsilon = 1$ ).  $\theta_W$  is the equilibrium contact angle on rough surfaces (also called *Wenzel angle*, Fig. 1-6a).  $\theta_Y$  is the intrinsic contact angle of a liquid on the flat surface of the same material, which can be determined by Young's equation. Equation (1.8) shows that

the surface wettability can be tuned by roughening the surface. If the material is hydrophilic ( $\theta_Y < 90^\circ$ ), the increased roughness makes the surface even more hydrophilic, i.e. the larger the roughness factor  $\epsilon$ , the smaller the Wenzel contact angle  $\theta_W$ . On the contrary, if the material is intrinsically hydrophobic ( $\theta_Y > 90^\circ$ ), a large value of  $\epsilon$  can make the surface even more hydrophobic ( $\theta_W > \theta_Y$ ) or even superhydrophobic ( $\theta_W > 150^\circ$ ).

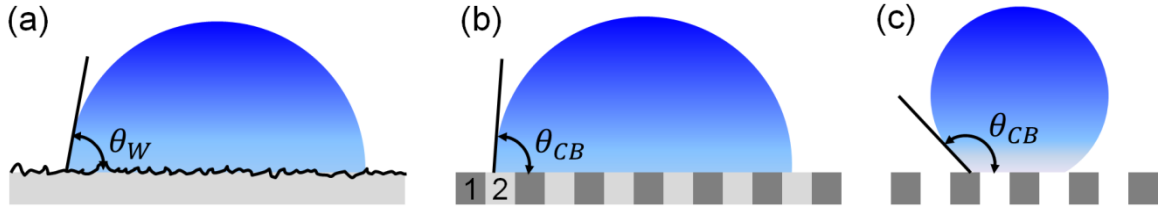


Figure 1-6 A drop rests on a rough surface (a) and on a chemical heterogeneous surface (b). (c) The drop rests on top of the asperities (Cassie-Baxter state).

Later, Cassie and Baxter extended Wenzel's analysis to porous surfaces formed by regularly aligned fibers [8]. They considered the different interfacial energies generated by two "chemical" components: the solid fibers and the air between fibers. They proposed the primary form of the Cassie-Baxter equation for chemical heterogeneous surfaces. However, a relatively rigorous derivation was achieved only much later [1, 9-11]. Fig. 1-6b shows a smooth solid surface made with a mixed chemical compositions, material 1 and 2, which have liquid contact angles of  $\theta_1$  and  $\theta_2$  on smooth surfaces, respectively. If the liquid contact line is displaced by a small distance  $dl$ , the change of the surface energy per unit length is

$$dE = f_1(\gamma_{LS-1} - \gamma_{SV-1})dl + f_2(\gamma_{LS-2} - \gamma_{SV-2})dl + \cos \theta_{CB}\gamma dl \quad (1.9)$$

where  $f_i$ ,  $\gamma_{LS-i}$ ,  $\gamma_{SV-i}$  are respectively the length fraction, liquid-solid and solid-vapor interfacial tensions for each chemical species, and  $f_1 + f_2 = 1$ .  $\theta_{CB}$  is the equilibrium contact angle of this surface and is also called *Cassie-Baxter angle*. The total surface energy reaches the lowest state when the contact line is in equilibrium, i.e.  $\frac{dE}{dl} = 0$ . Equation (1.9) simplifies to the below modified expression of Young's equation

$$\cos \theta_{CB} = f_1 \cos \theta_1 + (1 - f_1) \cos \theta_2 \quad (1.10)$$

Equation (1.10) is the Cassie-Baxter equation. Now, we consider the case that component 2 is air, which is the situation for water drops on some natural rough surface such as lotus leaf (Fig. 1-6c). Then,  $\theta_2$  has a value of  $\sim 180^\circ$  and the equation takes the form

$$\cos \theta_{CB} = f_1 (1 + \cos \theta_1) - 1 \quad (1.11)$$

The above relation is the key equation that indicates how to fabricate superhydrophobic surfaces [5, 11, 12]. First, the base material should be hydrophobic ( $\theta_A > 90^\circ$ ). Second, the solid fraction of the roughness needs to be very small ( $f_1 \ll 1$ ). However, it is noted that the derivation of equation (1.11) is based on one strong assumption: the drop rests on top of the surface asperities, i.e. it is in the Cassie-Baxter state. A drop being initially in the Cassie-Baxter state could jump to the Wenzel state if the surface roughness is not high enough [13], and eventually this will result in the failure of superhydrophobicity. Chen *et al.* carried out a systematic study of the geometric effects of roughness on superhydrophobicity and proposed a third dimensionless number, bulk aspect ratio, which compares the size, height and spacing of the surface asperities to achieve superhydrophobicity [14, 15]. They found that in addition to a small solid fraction the stable superhydrophobic surfaces should have a bulk aspect ratio larger than 4.

#### *Precursor Film*

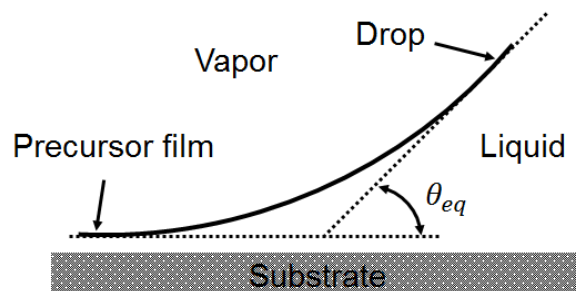


Figure 1-7 Schematic of the zone near the three-phase contact line. The macroscopic spherical cap is connected to a thin film covering the substrate.

When the thickness of the drop thins down to submicroscopic dimensions, the long-range van der Waals force between the molecules of the liquid and the solid

---

outweigh other forces. Instead of a sharp extrapolation of the liquid-vapor interface to the surface, the contact line extends via a thin film of a few nanometer thickness farther out than the macroscopic drop itself [1, 16-22] (Fig. 1-7). This thin film is called *precursor film* and its width can reach up to few hundred micrometers on nanostructured hydrophilic surfaces [23]. Till now, most experimental observation of precursor films were reported for completely wetting surfaces only [1, 16-22] ( $\theta_{eq} \ll \sim 57.3^\circ$  or 1 radian). On partially wetting surfaces the existence of a precursor film is still controversial.

---

### 1.3.2 Sessile drops on soft substrates or surfaces

---

Soft substrates are an important class of substrates in our living world. From small objects like proteins, organelles, single cells, or connective tissues to large systems such as plant leaves, organs or entire animal: all are made of “soft materials”. Actually, all life forms are built upon and organized around soft biogenic materials. Investigations of wetting phenomena on soft substrates appear to be very crucial and urgent, also for understanding the world around us [24].

Unlike rigid substrates, a sessile drop can deform a soft substrate, as illustrated in Fig. 1-8a. Two forces related to capillarity lead to the deformation. First, the vertical component of the liquid surface tension is applied to the surface near the contact line and causes a “wetting ridge” with a height of the order of [25-28]

$$h \approx \frac{\gamma \sin \theta_{eq}}{G} \quad (1.12)$$

where  $G$  is the shear modulus of the soft material. This deformation is normally negligible for rigid substrates. Taking silicon, for example, the Young’s modulus is typically 130-190 GPa [29] which results in a wetting ridge of less than 1 pm. In contrast, biomaterials such as soft tissues have Young’s moduli of the order of 1 kPa [30-32] and the surface tension force leads to a wetting ridge of  $\sim 100 \mu\text{m}$ , which can influence significantly dynamic wetting processes [26, 27, 33-37], drop impact [38-40], dropwise condensation [41], and sessile drop evaporation [42, 43].

The second force is from the Laplace - or capillary - pressure. If the substrate is semi-infinite, the missing of a part of the spherical cap results in a net pressure, which



is applied perpendicular to the liquid-solid interface on the surface and leads to a quasi-spherical dimple underneath the drop (Fig. 1-8a). Since the Laplace pressure is inversely proportional to the size of the drop, the depth of the dimple is larger for small drops than that for large drops. However, if the thickness of the soft material is finite, the capillary force cannot be compensated by the soft film due to the appearance of the background rigid substrate. Eventually, the deformation under the drop is much shallower and the deformation profile is more complex (Fig. 1-8b) [44].

The observation of the “wetting ridge” was pioneered by Carré *et al.* [33] with an optical method and followed by several other authors [45-50]. Only recently, however, Pericet-Camara *et al.* characterized the entire deformation of sessile micro-drops on soft polydimethylsiloxane (PDMS) substrates using laser scanning confocal microscopy [44, 51]. They analyzed the profiles of the whole substrate deformation and also reported the influence of the finite film thickness and of the supporting rigid substrate [44].

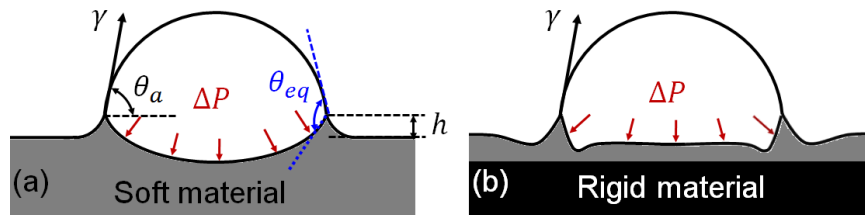


Figure 1-8 Schematic of the deformation induced by surface tension  $\gamma$  and Laplace pressure  $\Delta P$  on a bulk soft substrate (a) and on a thin soft film supported by a rigid substrate (b).

As a “wetting ridge” is pulled up by surface tension around the contact line and a dimple structure is formed underneath the drop by Laplace pressure, it is difficult to discern the actual position of contact line and the solid-liquid interface. The “apparent” equilibrium contact angle  $\theta_a$  which we observe on soft substrates with standard optical techniques differs from the Young’s angle  $\theta_Y$  [49] (Fig. 1-8a).  $\theta_a$  is not only determined by the liquid-solid chemical interaction, but also by the softness of the substrate. In other words, the “apparent” contact angle  $\theta_a$  cannot be used to characterize the surface chemical properties, i.e. its wettability, any more.

---

## 1.4 Dynamic wetting

---

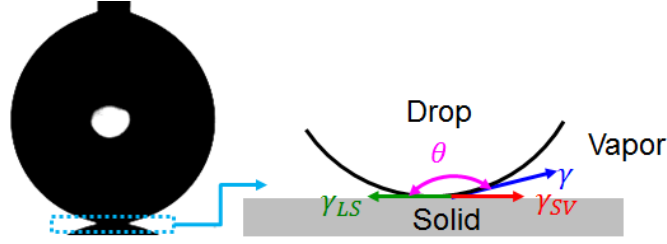


Figure 1-9 The initial state of a drop touching a solid surface.

The equilibrium state of a drop on a surface is reached when the liquid-solid-vapor interfacial tensions,  $\gamma$ ,  $\gamma_{LS}$ ,  $\gamma_{SV}$  are balanced, i.e. the drop attains a semi-spherical shape with an equilibrium contact angle of  $\theta_{eq}$ . How does a drop reach equilibrium after its first contact with a solid surface? Just after contact, the contact angle  $\theta$  is very large ( $\sim 180^\circ$ , see Fig. 1-9), which results in a net horizontal force per unit length of

$$F_C = \gamma_{SV} - \gamma \cos \theta - \gamma_{SL} = \gamma(\cos \theta_{eq} - \cos \theta) \quad (1.13)$$

This force pulls on the contact line and causes the liquid to spread on the surface until it reaches equilibrium, characterized by a contact angle  $\theta_{eq}$ .

---

### 1.4.1 Dynamic wetting on rigid surfaces

---

#### *Initial inertial wetting stage*

Just after contact, the capillary driving force,  $\gamma(\cos \theta_{eq} - \cos \theta)$ , is very large and leads to a high speed of spreading (in the order of 1 m/s). Both experimental studies and molecular dynamics simulations showed that the spreading radius,  $r$ , grew with spreading time  $t$  according to a power law  $r = Kt^{0.5}$  [52], which is independent of surface wettability and liquid viscosity (it is valid, however, only for relatively low viscosity liquids).  $K$  is a coefficient. This wetting stage lasts only  $\sim 100 \mu\text{s}$  and only weakly depends on drop size [52, 53]. There are two main forces resisting the spreading during this process: the kinetic energy of the moving drop and the viscous dissipation in the liquid. The Reynolds number,  $Re = \frac{\rho UR_0}{\mu}$ , which compares the inertial and the viscous force, is much larger than unity.  $\rho$ ,  $R_0$ , and  $\mu$  are

density, radius, and viscosity of the liquid drop.  $U$  is the speed of the moving contact line. Thus, inertia dominates the spreading. However, a complete model about fast drop spreading dynamics is still missing.

### Second inertial wetting stage

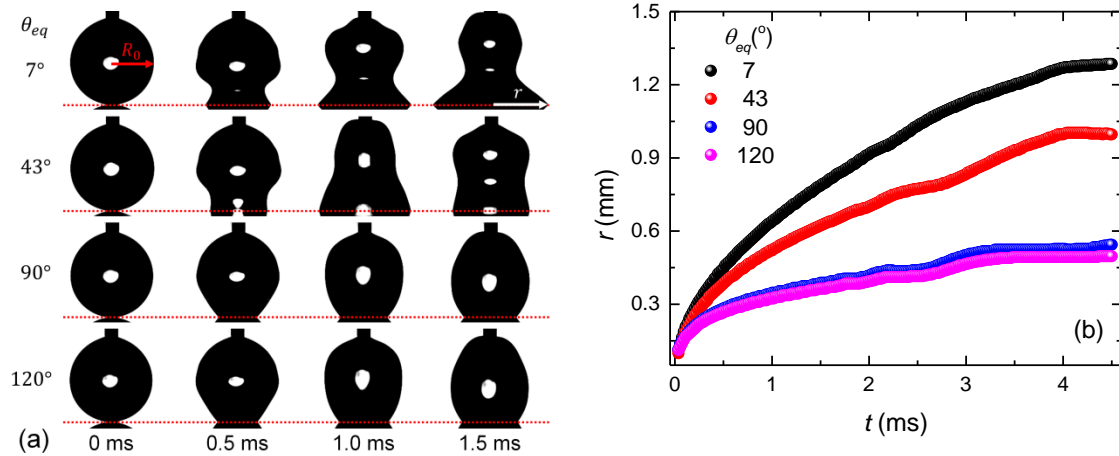


Figure 1-10 (a) Water droplets spread on four surfaces with different wettability. (b) Spreading radius vs. time for the spreading process in (a). The initial radius of all drops was  $R_0 = 0.6$  mm.

When  $t \geq 100\mu\text{s}$ , the spreading speed is still high ( $\sim 0.1$  m/s), and now depends on the surface wettability. Figure 1-10a shows water drops spreading on four surfaces with different wettability ( $\theta_{eq} \approx 7^\circ, 43^\circ, 90^\circ, 120^\circ$ ). On the hydrophilic surface with  $\theta_{eq} \approx 7^\circ$ , the liquid near the liquid-solid interface spreads faster than that above it. Within  $\sim 0.5\text{ms}$ , a dynamic contact angle smaller than  $90^\circ$  is formed. By contrast, spreading is slower on hydrophobic surfaces with  $\theta_{eq} \gtrsim 90^\circ$  and the drop has a dynamic contact angle larger than  $90^\circ$ . A transition to dynamic contact angle of  $90^\circ$  can be found on the surface with  $\theta_{eq} \approx 43^\circ$ . In general, the contact radius grows faster on hydrophilic than that on hydrophobic surfaces. This is clearly shown in the plot of spreading radii as a function of spreading time in Fig. 1-10b.

Figure 1-11 displays the same data of Fig. 1-10b in log-log scale. The spreading radius follows a power law growth with time,  $r = K't^\alpha$ . Each of these curves corresponds to a different  $\theta_{eq}$  and has a different exponent  $\alpha$ . For the most

hydrophilic surface ( $\theta_{eq} \approx 7^\circ$ ),  $\alpha \approx 0.5$ . For hydrophobic surfaces,  $\alpha$  is smaller than 0.5 and decreases monotonically with  $\theta_{eq}$ .

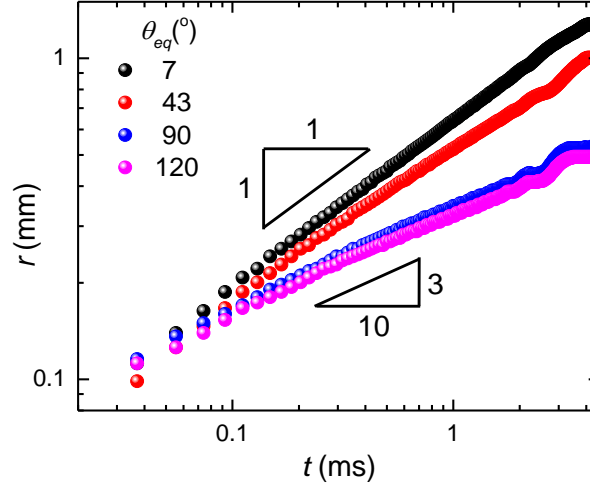


Figure 1-11 Log-log plot of the experimental data in Figure 1-10b.

This spreading stage is still dominated by inertia, but not yet by viscosity. This can be rationalized in two ways. On one hand, the Reynolds number is still much larger than one. On the other hand, the spreading up to this point lasted only up to 10 milliseconds, depending also on the drop size. This time is comparable to the characteristic inertial time,  $\sqrt{\frac{\rho R_0^3}{\gamma}}$ , and much different from the characteristic viscous time,  $\mu R_0/\gamma$ . A few theoretical models, though currently still partially empirical, were proposed to describe the spreading/wetting dynamics at this early time. Bianco *et al.* proposed a scaling law based on Newton's second law [54]. They found a power law with an exponent of 0.5 to describe the wetting on completely wetting surfaces. Bird *et al.* considered the energy dissipation during spreading [55] and derived a power law which relates  $\alpha$  with  $\theta_{eq}$ . They suggested that the change of surface energy during wetting was transferred into the kinetic energy of the moving drop, by which the governing equation is obtained

$$\int_V \frac{1}{2} \rho |u|^2 dV = \gamma [A(0) - A(t) + \pi r^2 \cos \theta_{eq}] \quad (1.14)$$

$u(r, t)$  is the velocity field at position  $r$  and at time  $t$ , and  $V$  is the "effective" volume of the moving drop.  $A(t)$  is the surface area of the liquid-vapor interface. Adapting a

self-similar velocity field to vary over the length of  $l_v \propto (\frac{\gamma t^2}{\rho})^{1/3}$  [56] and further assuming that the surface area of the spreading drop scales as  $r^2$ , i.e.  $A(0) - A(t) = \pi F(\theta_{eq})r^2$ , equation (1.14) is simplified to

$$\frac{t}{r} \frac{dr}{dt} \propto \sqrt{F(\theta_{eq}) + \cos \theta_{eq}} \quad (1.15)$$

$F(\theta_{eq})$  is an unknown function. Solving the above equation results in

$$r = K't^\alpha, \text{ with } \alpha = C \sqrt{F(\theta_{eq}) + \cos \theta_{eq}} \quad (1.16)$$

Equation (1.16) shows that the exponent of the power law depends only on the equilibrium contact angle  $\theta_{eq}$ . This matches with the experimental observations [55].

#### Viscous wetting stage

On strongly hydrophilic ( $\theta_{eq} \ll \sim 57.3^\circ$  or 1 radian) or completely wetting surfaces ( $\theta_{eq} \sim 0^\circ$ ), a third wetting stage was found after the two inertial stages. In this stage, the wetting speed is much slower than in the previous two stages, and  $Re < 1$ . There are two theories describing this wetting stage: the Hydrodynamic Model (HDM) and the Molecular Kinetic Theory (MKT).

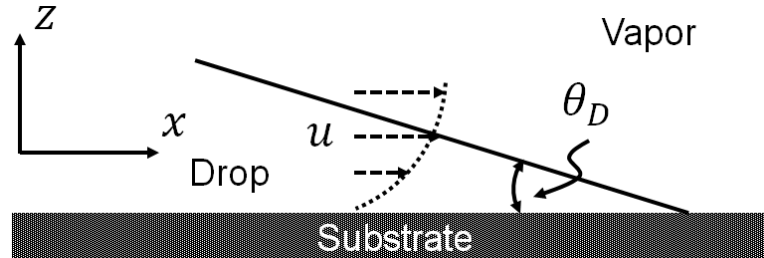


Figure 1-12 Spreading flow near the wedge of the drop for  $\theta \ll 1$ .

Huh and Scriven were probably the first to consider the complicated hydrodynamic problem of flow near the triple line of a liquid that spreads on a solid surface [57]. Since then, a larger number of researchers have started working on the problem, as is addressed in a classical review paper by de Gennes [18]. In the same paper, de Gennes developed a successful hydrodynamic model based on work of Huh and Scriven, in which the capillary driving force is compensated by the viscous dissipation in the liquid.

As illustrated in Fig. 1-12, the wedge of the drop was treated as a flat film ( $\theta \ll 1$ ), with a Poiseuille type of velocity field,  $u_z = u(z)$ . Assuming that the velocity of the contact line  $U$  is the average velocity in a film with a height  $e$  one can find that

$$u(z) = \frac{3U}{2e^2}(-z^2 + 2ez) \quad (1.17)$$

The viscous dissipation in the wedge is

$$T\dot{S} = \int_{x_{min}}^{x_{max}} dx \int_0^e \mu \left(\frac{du}{dz}\right)^2 dz \cong \frac{3\mu U^2}{\theta} \ln \left| \frac{x_{max}}{x_{min}} \right| \quad (1.18)$$

Where  $x_{max}$  is a cutoff length related to the macroscopic size of the drop,  $x_{max} \sim R_0$ , and  $x_{min}$  is a cutoff length close to molecular size.

One key assumption of this model is that a precursor film exists in front of the bulk contact line. Thus, the capillary driving energy is simplified to

$$F_c U = \gamma(1 - \cos \theta)U \cong \frac{\theta^2}{2} \gamma U \quad (1.19)$$

Balancing equations (1.18) and (1.19) and denoting  $\ln \left| \frac{x_{max}}{x_{min}} \right| = l$ , we obtain

$$U = \frac{dr}{dt} = \frac{\gamma}{6\mu l} \theta^3 \quad (1.20)$$

Neglecting the precursor film (the volume of the precursor film is much smaller than that of the drop), the volume of the drop can be expressed as  $V \approx \pi r^3 \theta$ . By differentiation one obtains

$$\frac{d\theta}{dt} = -\frac{\gamma}{\mu V^{1/3}} \theta^{13/3} \quad (1.21)$$

which ultimately leads to

$$\theta \approx \left(\frac{\mu V^{1/3}}{\gamma t}\right)^{3/10} \text{ or } r \propto V^{1/3} \left(\frac{\gamma t}{\mu}\right)^{1/10} \quad (1.22)$$

Equation (1.22) is also called *Tanner's law*, since he pioneered investigations of spreading drops on completely wettable surfaces [58]. Indeed, a power law of  $r \approx K'' t^{0.1}$  was observed in a number of experimental studies [54, 59-61].

One shortcoming of the hydrodynamic model is the divergence of the viscous dissipation when the cutoff length  $x_{min} \rightarrow 0$  (see equation 1.18). Thus, microscopic models were proposed as complementary theories. Blake and Haynes suggested that the motion of the contact line is controlled by thermally activated liquid

displacements [62]. As illustrated schematically in Fig. 1-13, there are  $n$  adsorption sites per unit area and the average length of each molecular displacement is  $\lambda$ . During drop spreading, liquid molecules are moving forward and backward with a defined “hopping” frequency. Applying Eyring’s theory of absolute reaction rates [63], the frequency of molecular displacements in the forward direction  $k_W^+$  and that in the backward direction  $k_W^-$  can be expressed as

$$k_W^+ = k_W^0 \exp\left(\frac{W}{2nk_B T}\right) \quad (1.23)$$

$$k_W^- = k_W^0 \exp\left(\frac{-W}{2nk_B T}\right) \quad (1.24)$$

$k_W^0$  is the frequency of molecular displacements at equilibrium (then  $k_W^- = k_W^+ = k_W^0$ ).  $W$  is the work done by the shear stress per unit displacement of unit length of the wetting line.  $k_B$  is the Boltzmann constant and  $T$  is the absolute temperature. The speed of wetting is therefore defined as

$$U = (k_W^+ - k_W^-)\lambda = 2k_W^0\lambda \sinh\left(\frac{W}{2nk_B T}\right) \quad (1.25)$$

As the shear stress is applied by the surface tension, equation (1.23) becomes

$$U = 2k_W^0\lambda \sinh\left[\frac{\gamma(\cos \theta_{eq} - \cos \theta)}{2nk_B T}\right] \quad (1.26)$$

The above model is called molecular kinetic theory (MKT model). In the MKT model,  $k_W^0$ ,  $n$ ,  $\lambda$  are three unknown parameters. This results in a limited applicability of the model. To match the theory with experiments, these unknown parameters need to be fitted based on the experimental data, and it was found that  $\lambda$  is always much larger than a molecular size [1]. If the term of  $\sinh$  in equation (1.26) is very small and the surface is very hydrophilic, equation (1.26) can be further simplified to a power law [64]

$$r \sim t^{1/7} \quad (1.27)$$

The different power laws between hydrodynamic model (Eq. 1.22) and molecular kinetic theory (Eq. 1.27) are due to the different dependence of wetting angle on wetting speed: HDM predicts that for small angles  $U \propto \theta^3$  (1.20) while MKT predicts that  $U \propto \theta^2$  (1.26).

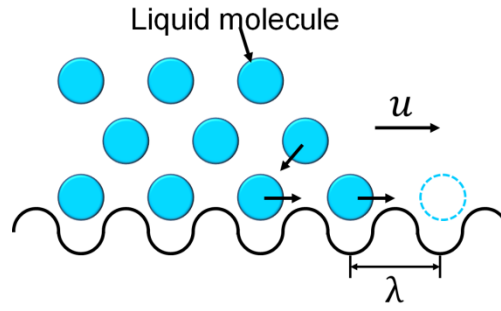


Figure 1-13 Schematic representation of the molecular-kinetic model of wetting.

### 1.4.2 Dynamic wetting on soft substrates

On soft substrates, an extremely slow stage ( $U < 10^{-4}$  m/s) was observed and it was found that it does follow neither the inertial nor the viscous wetting law. Since the spreading speed is extremely slow, inertia is negligible, and thus there are only two possible dissipation sources resisting the spreading. The first one is the viscous dissipation in the liquid, as discussed in the previous section. The second one is related to the “wetting ridge” generated by capillary forces. As the contact line moves, the “wetting ridge” also moves, which leads to a viscoelastic dissipation inside the soft substrate [26, 27, 33, 34, 37],  $\dot{E}\Delta$ , given by

$$\dot{E}\Delta \approx \frac{\gamma^2 U}{2\pi G \varepsilon} \left( \frac{U}{U^*} \right)^{\alpha''} \quad (1.28)$$

$\varepsilon$  is a cutoff distance near the contact line, which is of the order of 0.1-1  $\mu\text{m}$ . Where  $U^*$  is a characteristic speed.  $U^*$  and  $\alpha''$  are related to the rate-dependent viscoelastic dissipation of the solid. Now, the new energy balance equation is

$$\cos \theta_{eq} - \cos \theta \approx \frac{3\mu U l}{\gamma \theta} + \frac{\gamma}{2\pi G \varepsilon} \left( \frac{U}{U^*} \right)^{\alpha''} \quad (1.29)$$

If viscous dissipation dominates drop spreading, equation (1.29) recovers the viscous wetting law. On the other hand, if viscoelastic dissipation dominates drop spreading, we obtain another power law

$$\log(\cos \theta_{eq} - \cos \theta) \approx \alpha'' \log U + \log\left(\frac{\gamma}{2\pi G \varepsilon U^{\alpha''}}\right) \quad (1.30)$$

Carré and Shanahan were the first to study dynamic wetting on soft substrates [26, 27, 33, 34, 37]. Their experimental results showed that wetting was independent of





liquid viscosity, but dependent on the surface softness. They confirmed the viscoelastic wetting law shown in equation (1.29).





**Part I Effects of Substrate Softness and Curvature on Dynamic Wetting**





---

## 2 Early Dynamic Wetting on Soft Substrates<sup>1</sup>

---

In this chapter, the early dynamic wetting on soft substrates is studied. In the first step, dynamic wetting of various liquids with different surface tensions and viscosities on various viscoelastic soft substrates was investigated using a high speed camera. A novel fast wetting stage was found in the time scale 0.1–10 milliseconds. The wetting dynamics was dominated by inertia and followed a power law with the exponent depending on surface wettability, but not on substrate softness. On the other hand, the duration of this fast inertial wetting was controlled by the softness of the substrate. After the inertial stage, wetting entered into a slow viscoelasticity-dominated stage. In the second step, a simple model was developed with Prof. Martin E.R. Shanahan (Université Bordeaux, France) to describe the early dynamic wetting on soft viscoelastic substrates. The theoretically predicted transition time between the inertial and the viscoelastic stage matched the experimental data in the order of magnitude.

---

### 2.1 Motivation

---

Wetting phenomena on soft substrates are commonly encountered in our daily life, from washing hands, to painting a wall, to lubricating our eyes several times per minute, and so on. However, wetting dynamics on soft substrates is still not fully understood. In the late 20<sup>th</sup> century, Carré and Shanahan pioneered the study of wetting phenomena on soft substrates [26, 27, 33, 34, 37]. They found that the vertical component of surface tension of a drop leads to the deformation of substrate near the contact line. This deformation was called “wetting ridge”. When the drop spreads, the “wetting ridge” moves with the contact line and causes viscoelastic dissipation, which dominates and slows down the spreading by the so called “viscoelastic braking” [65]. Due to the low time resolution of the camera at that time, it was impossible for the authors to investigate the initial wetting stages just after the

---

<sup>1</sup> This chapter is based on “L.Q. Chen, G.K. Auernhammer, E. Bonaccorso, *Short time wetting dynamics on soft surfaces*, *Soft Matter* 7, 9084 2011” and “L. Q. Chen, E. Bonaccorso, M.E.R. Shanahan, *Inertial to viscoelastic transition in early drop spreading on soft surfaces*, *Langmuir* 29, 1893 2013”.

---

drop touched the soft substrate. Since an inertial wetting stage was reported on rigid surfaces [54, 55, 66], one natural question is whether it exists on soft substrates as well. If yes, how long does it last? Are there any effects of substrate softness on the duration of inertial wetting? How and to which extent does the substrate softness influence the inertial wetting? These questions lead me to carry out a systematic study of the early dynamic wetting on soft substrates.

---

## 2.2 Experiments

---

### 2.2.1 Soft substrates

---

#### *Fabrication of soft PDMS thin films*

The soft substrates were fabricated with polydimethylsiloxane (PDMS, Sylgard 184, Dow Corning, Wiesbaden, Germany). The polymer chain of the monomer can be branched or cross-linked by a curing agent. Through varying the mass ratio of the monomer and curing agent, the viscoelastic properties of the material can be controlled after a hard bake in an oven. In the experiments, monomer/curing agent ratios of 100:1, 75:1, 50:1, 20:1, and 10:1 were used. Since the chemical components of these PDMS are the same, the surface chemistry properties of them are always the same.

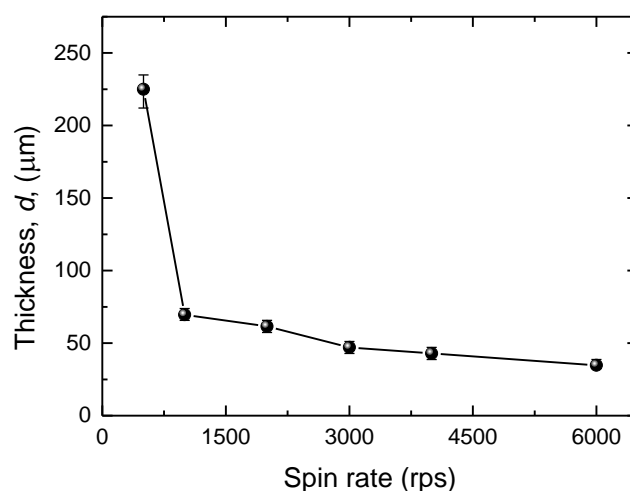


Figure 2-1 The thickness of PDMS film as a function of spin-coating rate.

Square glass slides with dimension of  $22 \times 22 \text{ mm}^2$  ( $500 \mu\text{m}$ -thickness) were first cleaned in acetone (Sigma-Aldrich, p.a.) and then in ethanol (Sigma-Aldrich, p.a.) in an ultrasonic bath for 5 min, respectively. After drying with purified nitrogen, well mixed PDMS solutions with different monomer/ curing agent ratios were spin-coated on these glass slides for 1 min. The PDMS coated films were cured overnight at  $70 \text{ }^\circ\text{C}$  in an oven. The thickness,  $d$ , of the films was controlled by the spin coating rate. Figure 2-1 shows the thickness of the PDMS film as a function of spin rate. By increasing the spin rate from 500 to 3,000 rpm, PDMS films with thickness of 30-200  $\mu\text{m}$  were prepared. The film thickness was measured with a  $\mu$ -Surf white-light confocal profiler (NanofocusAG, Oberhausen, Germany).

*Characterization of the soft materials at low frequency*

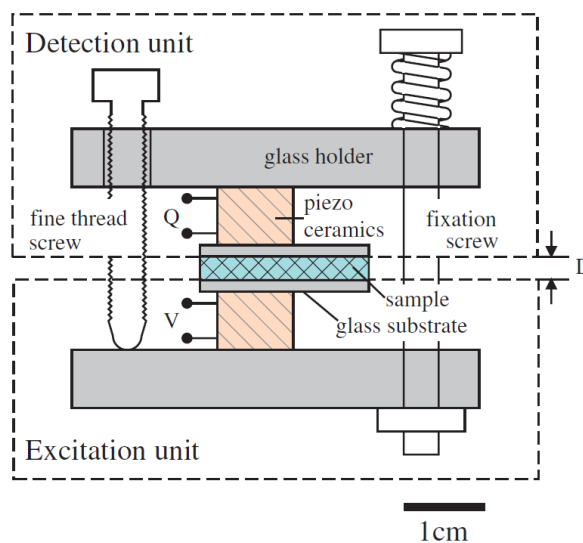


Figure 2-2 Sketch of the measurement cell of the homemade piezo-rheometer [67].

The shear modulus of the soft materials was measured with a homemade piezo-rheometer<sup>2</sup> in shear mode at 0.1~1000 Hz. Figure 2-2 illustrates the sketch of measurement cell. Two piezo-ceramic stacks ( $12 \times 20 \times 2 \text{ mm}^3$ , PICA™ Shear Piezo

<sup>2</sup> The measurements were done in the Max-Plank Institute for Polymer Research, Mainz. The piezo-rheometer was built by Marcel Roth and Miao Wang assisted me for the measurements.

Actuators; PICeramic, Lederhose, Germany) each of which was glued to a glass substrate on one side and a massive glass holder on the other side. The glass holders were fixed together defining a gap between the two glass substrates, in which the sample was filled. The gap size could be adjusted with three fine thread screws. The parallelism of the two plates can be checked by the Newton rings generated by interference of the light reflected by the surfaces of two plates. Detailed information and working principle of the setup could be found elsewhere [67].

Freshly mixed PDMS solution was filled between these two flat glass substrates with a gap width of 200  $\mu\text{m}$ . Then, the measurement cell was transferred into a vacuum desiccator for degasing. After 1 hour, the measurement cell with the sample was put in an oven and heated overnight at 70  $^{\circ}\text{C}$  (the same cross-linking condition as the fabrication of soft substrates). Before the measurements, the setup was calibrated using highly viscous gauge oil (100000BW, 100 Pa s, DKD). All measurements were carried out at 20  $^{\circ}\text{C}$  (the temperature for wetting experiments).

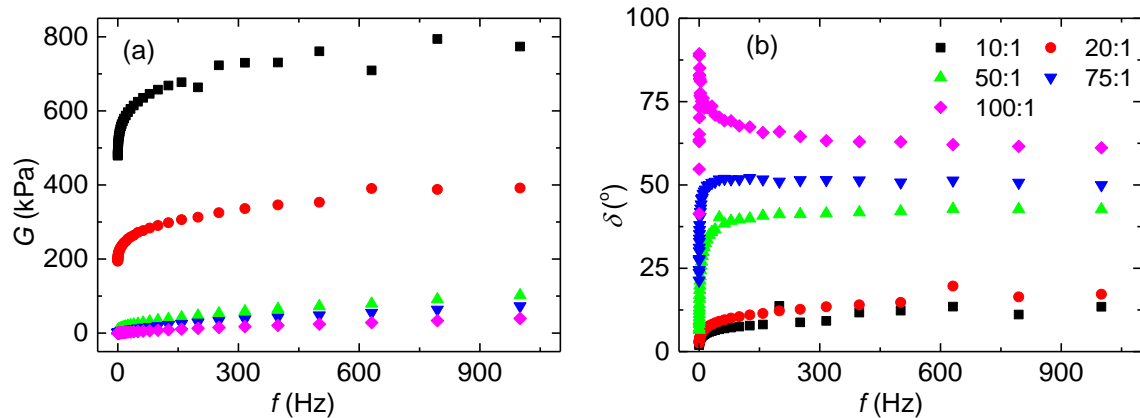


Figure 2-3 (a) Plot of shear modulus  $G$  of PDMS with different monomer/cross-linker ratios as a function of frequency  $f$ . (b) The corresponding phase angle  $\delta$  of PDMS in (a) as a function of frequency  $f$ .

Viscoelastic materials exhibit both viscous and elastic properties under oscillatory stress. In rheology measurements, the storage modulus  $G'$  - which characterizes the elastic property - and the loss modulus  $G''$  - which characterizes the viscous property - were measured. The shear modulus can be calculated with  $G = \sqrt{G'^2 + G''^2}$ . The storage modulus and loss modulus can be related with the phase



angle  $\delta$  ( $\tan \delta = G'/G''$ ,  $G' = G \cos \delta$  and  $G'' = G \sin \delta$ ).  $\delta$  is ideally  $0^\circ$  for purely elastic materials and  $90^\circ$  for purely viscous materials.

Figure 2-3a shows the shear modulus,  $G$ , as a function of frequency,  $f$ , for five PDMS materials which used in the experiments. Generally,  $G$  increases with  $f$  for all samples and PDMS is harder for small monomer/cross-linker ratios than that with large ratios. Figure 2-3b illustrates  $\delta$  as a function of  $f$ . All materials show a comparatively more viscous property under high frequency than under low frequency. PDMS is almost purely elastic ( $\delta$  close to  $0$ ) for mixing ratios close to 10:1 and it becomes more and more viscous with increasing the ratio of monomer/curing agent. In the experiments, the five materials were denoted by the shear modulus measured at 1Hz, as shown in Fig. 2-4.

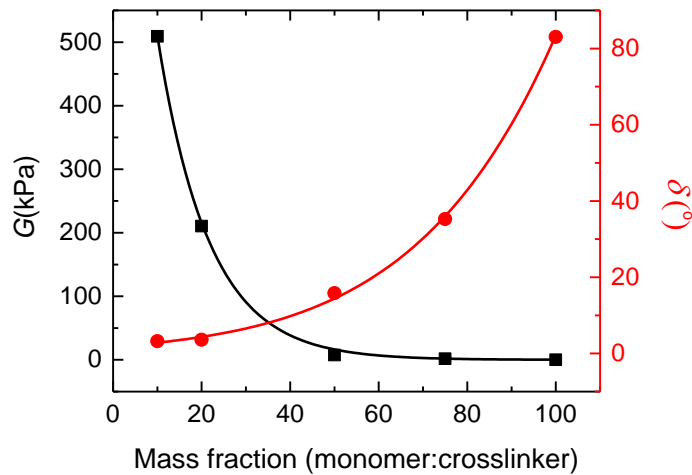


Figure 2-4 Shear modulus  $G$  and phase angle  $\delta$  for five PDMS samples at 1Hz. Solid lines are guides for the eye.

#### *Characterization of the soft materials at high frequency*

When a drop spreads on soft substrates, a stress is applied on the substrate by the surface tension of moving drop. The frequency of the stress can be related approximately to the spreading speed with  $f \approx U/2\pi\varepsilon$  [35]. In the inertial wetting stage,  $U$  is in the order of 1 m/s [35, 36, 55]. Taking a cutoff length of  $1 \mu m$ , the calculated frequency is  $\sim 8 \times 10^4$  Hz. Thus, it is essential to characterize these soft substrates under high frequency as well.

The storage modulus and loss modulus under high frequency were measured<sup>3</sup> using a commercial angular rheometer (ARES mechanical spectrometer, Rheometric Scientific). PDMS substrates with a thickness of  $\sim 1$  cm were cut into pieces of  $2 \times 2$  cm<sup>2</sup>. The mechanical properties were measured with an angular frequency of 0.1-100 rad/s between -140 °C and 20 °C. Then, the time-temperature superposition principles was employed to predict the influence of measurement frequency on dynamic viscoelastic properties up to  $10^8$  Hz at 20 °C. Figure 2-5 shows the shear modulus of the viscoelastic materials used in the experiments.

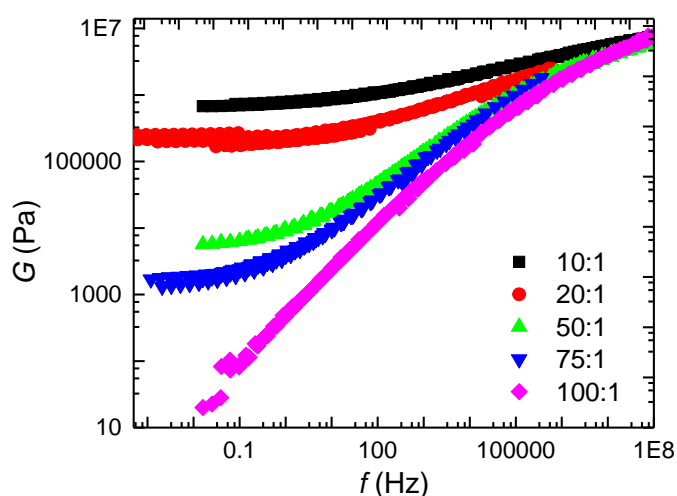


Figure 2-5 Plot of shear modulus  $G$  as a function of frequency  $f$ .

---

### 2.2.2 Liquids

---

Wetting experiments were done with deionized milliQ water, ethanol, deionized water/ethanol and deionized water/glycerol mixtures. These liquids have surface tensions ranging from 22.3 to 72.7 mN/m and viscosities in the range from 0.89 to 10.80 mPa s. The equilibrium contact angle of these liquids on the most rigid PDMS (monomer/curing agent ratio is 10:1) surfaces are between  $41^\circ$  and  $114^\circ$ . More detailed information about the liquids and the corresponding  $\theta_{eq}$  on rigid PDMS surface ( $G=510$  kPa @ 1Hz) are collected in Table 2.1.

---

<sup>3</sup> The measurements were done by Andreas Hanewald in the Max-Plank Institute for Polymer Research, Mainz.

Table 2-1 Physical properties and contact angles on rigid PDMS ( $G=510$  kPa @ 1Hz) of droplets of various liquids.

Liquids	$\rho$ (kg/m <sup>3</sup> )	$\gamma$ (mN/m) <sup>[68, 69]</sup>	$\mu$ (mPa·s, at 20°C) <sup>[68, 70]</sup>	$\theta_{eq}$ (°)
Water	1000	72.7	1.00	114±2
10 wt% ethanol/water	980	48.1	1.32	96±1
40 wt% ethanol/water	931	30.7	2.35	65±1
60 wt% glycerol/water	1154	67.2	10.20	92±3
Ethanol	785	22.3	0.89	41±2

### 2.2.3 Experimental setup

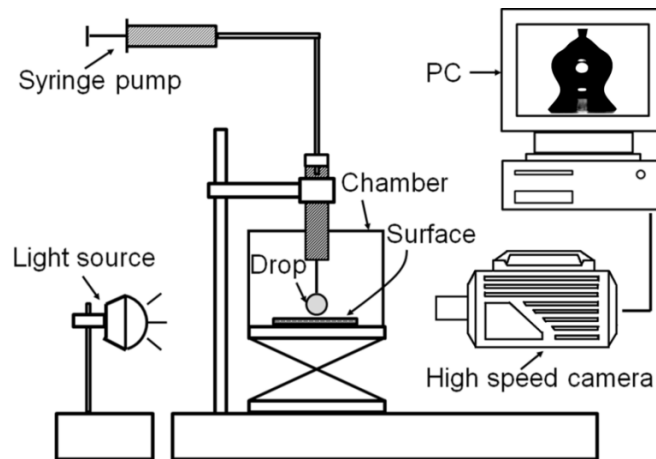


Figure 2-6 Setup for drop spreading experiments.

Figure 2-6 shows the scheme of the experimental setup. The PDMS substrate was placed on a vertical stage in a closed environmental chamber to prevent dust and acoustic vibrations which may affect the experiments. A steel needle with an inner diameter of 200-400  $\mu\text{m}$  was placed above the substrate at a defined distance for generating a droplet. The needle was silanized by 1,1,1,3,3,3-hexamethyldisilazane (Roth GmbH, Germany) in a desiccator at room temperature for 12 h to prevent drops wetting it. Applying a syringe pump, drops with controlled initial radius of 0.79, 0.89 and 1.00 mm were generated. The vertical stage was controlled by a micrometer screw and it moved the substrate quasi-statically toward the drop. A cold light source

with a diffuser was used to illuminate drop and substrate from the back. The drop wetting process was recorded using a high-speed video camera (FASTCAM SA-1, Photron Inc., USA) with a frame rate of 54,000 fps. The resolution of the recorded image was  $10 \mu\text{m}$  per pixel. For each experimental parameter, at least six spreading drop events were acquired. In total, I evaluated data of around 1,000 drop spreading movies.

---

## 2.2.4 Data analysis

---

The videos of the spreading drops were processed by a self-programmed MATLAB<sup>®</sup> (MathWorks Inc., USA) algorithm. Zooming in the vicinity of the contact area between drop and surface by cutting each frame at  $\pm 125 \mu\text{m}$  aside the rim of the drop, the contour of the drop was identified by thresholding the images. From each image, the contact diameter  $r$  and the contact angle  $\theta$  of the drop were extracted.

On rigid surfaces, it is well known that the early wetting dynamics is dominated by inertia and drop spreading follows a power law [54, 55]. Therefore, it is also interesting to check if the early wetting on soft substrates can be described with a power law of the type  $r \propto t^\alpha$  as well. Thus, the Pearson product-moment correlation coefficient,  $\zeta$ , was applied to check the power law relationship between  $r$  and  $t$ .

$$\zeta = \frac{\sum_{i=1}^n (r'_i - \bar{r}') (t'_i - \bar{t}')}{\sqrt{\sum_{i=1}^n (r'_i - \bar{r}')^2} \sqrt{\sum_{i=1}^n (t'_i - \bar{t}')^2}} \quad (2.1)$$

$$\text{with } r' = \log r, t' = \log t, \bar{r}' = \frac{1}{n} \sum_{i=1}^n r'_i, \bar{t}' = \frac{1}{n} \sum_{i=1}^n t'_i$$

$\zeta$  has a value between -1 and 1.  $\zeta$  equals to 1 or -1 corresponds to a very good linear relationship between  $\log r$  and  $\log t$ , i.e. a very strong power law relationship between  $r$  and  $t$ .

---

## 2.3 Experimental results and discussion

---

### 2.3.1 Spreading process

---

In order to check if there are some influences of substrate softness on dynamic wetting, a rigid hydrophobic surface was used as a reference surface in the

experiments. The hydrophobic surfaces were oxygen plasma treated glass slides further silanized with 1,1,1,3,3,3-hexamethyldisilazane, as described in the previous section. The equilibrium contact angle of water on these surfaces was  $\sim 110^\circ$ , which is close to that on rigid PDMS ( $\sim 114^\circ$ ).

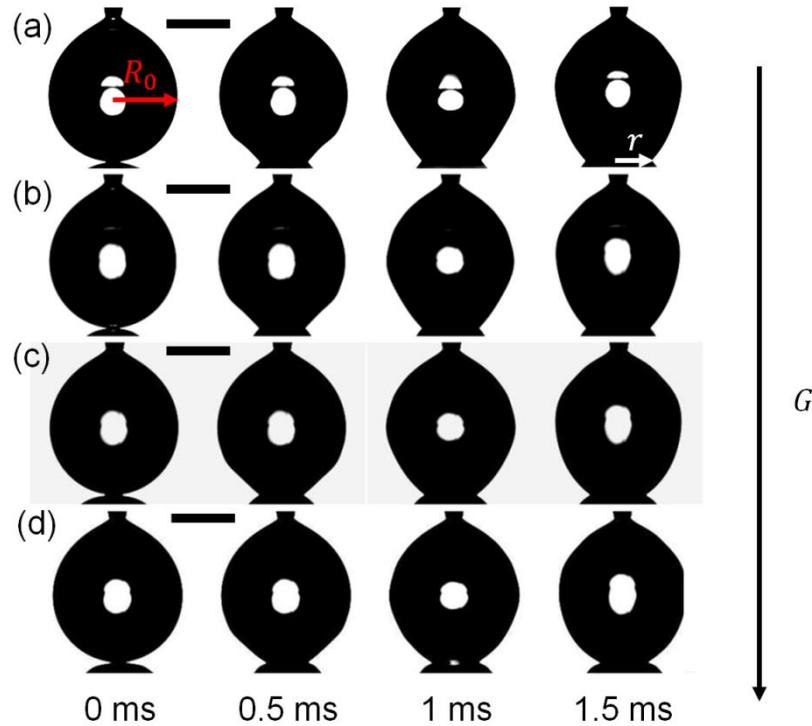


Figure 2-7 Spreading of 1.0 mm-radius water drop on five substrates with different softness: (a) hydrophobic glass surface, (b) PDMS substrate with  $G = 204$  kPa, (c) PDMS substrate with  $G = 5.8$  kPa, and (d) PDMS substrate with  $G = 0.02$  kPa. The scale bar is 1.0 mm.

Figure 2-7 shows the images of spreading water drops on the hydrophobic glass surface (Fig. 2-7a) and on three different soft substrates (Fig. 2-7b-d,  $\sim 200 \mu\text{m}$  thick). When droplets touched the four surfaces, they spread out spontaneously. The contact with the surface generated a capillary wave travelling along the surface of the droplet, as indicated by the arrows in Fig. 2-7a. On PDMS substrates with  $G \gtrsim 204$  kPa ( $\delta = 3.6^\circ$ ), the droplet spread continuously like that on the hydrophobic glass surface (Fig. 2-7a-b). On a relatively soft substrate with  $G = 5.8$  kPa ( $\delta = 15.8^\circ$ ), spreading was also continuous and fast at the beginning. After  $\sim 1$  ms, the moving of the contact line slowed down and proceeded with a stick/slip behavior. The stick/slip movement

was due to the formation of a so-called “wetting ridge” near the contact line, which will be discussed more in detail later. On the softest substrate ( $G = 0.02$  kPa and  $\delta = 83.1^\circ$ ) spreading almost stopped after  $\sim 0.5$  ms. Eventually, the wetted area was smaller on relatively soft than that on relatively rigid substrates for substrates with  $G \lesssim 204$  kPa (Fig. 2-7b-d). For PDMS substrates with  $G \gtrsim 204$  kPa, the wetted area was similar to that on hydrophobic glass surface (Fig. 2-7a-b).

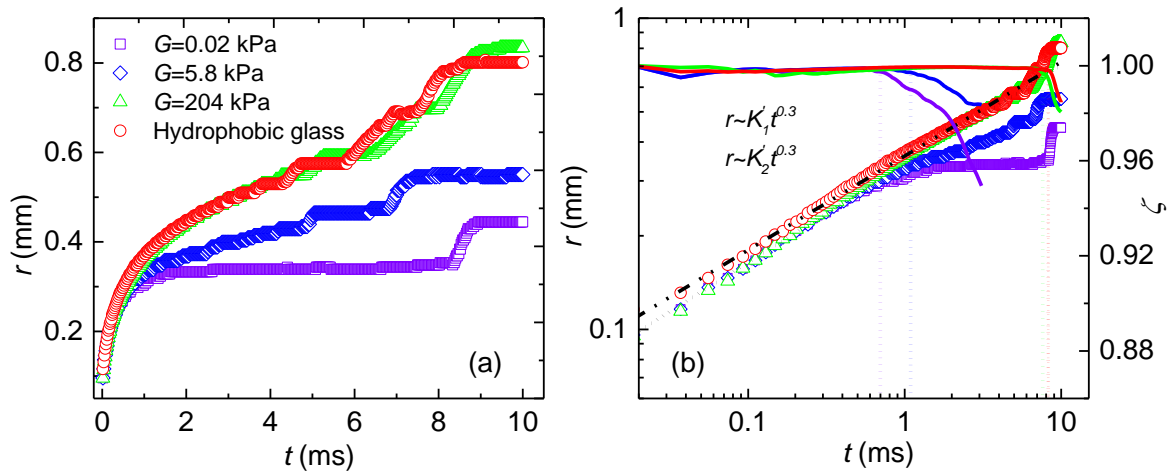


Figure 2-8 (a) Spreading radius  $r$  as a function of spreading time  $t$  of the wetting of 1.0 mm-radius water drop on four surfaces in Fig. 2-7. (b) Log-log representation of the experimental data in (a) and the corresponding Pearson product-moment correlation coefficient,  $\zeta$ , of  $\log r$  and  $\log t$  as a function of time (color solid lines). The black dashed lines are power law fittings and the color dashed lines show the different transition time  $\tau_T$  or  $\tau$ .

In order to quantify the effects of substrate softness on the wetting process, the spreading radius during wetting was extracted from the recorded images. As shown in Figure 2-8a, the initial spreading on all four surfaces was similar and the average spreading speed was  $U = \dot{r} \approx 0.5$  m/s in 1 ms. The spreading on relatively rigid PDMS substrates ( $G \gtrsim 210$  kPa) was similar to that on the hydrophobic glass surfaces (the data is almost overlapping, as shown in Fig. 2-8a). The duration of the fast wetting was  $\tau_T$  or  $\tau \sim 8$  ms ( $\tau_T$  for PDMS substrates and  $\tau$  for the hydrophobic glass surface). Afterwards, drops reached equilibrium. For soft PDMS substrates with  $G \lesssim 204$  kPa, the fast wetting lasted only  $\tau_T \lesssim 1$  ms, depending on substrate softness. Then,

spreading entered into another, slower stage. In this wetting stage,  $U \approx 0.007$  m/s and the motion of the TPCL proceeded with stick/slip behaviour (Fig. 2-7c-d & Fig. 2-8a).

The wetting dynamics on rigid surfaces always followed a power law,  $r = K't^\alpha$ , depending on the main driving and resistance forces [22, 36, 54, 55, 58, 59]. Thus, I checked if the early dynamics on soft substrates was similar. Figure 2-8b illustrates the linear correlation coefficient  $\zeta$  between  $\log r$  and  $\log t$  as a function of time  $t$ , for the data in Figure 2-8a.  $\zeta \approx 1$  when  $t \leq \tau_T$  or  $\tau$ , which indicates a nearly perfect power-law correlation between  $r$  and  $t$ . For  $t > \tau_T$  or  $\tau$ ,  $\zeta$  shows a sharp downward kink when the drop reached the equilibrium contact angle on hard substrates or when spreading switched to a new slow stage on soft substrates. Therefore, the spreading radius  $r$  for  $t \leq \tau_T$  or  $\tau$  was fitted as a power law of  $t$  with the least square method (LSM). It was found that the spreading radius grew according to  $r = K't^{0.3}$  on the hydrophobic and on the PDMS substrates (only the coefficients were slightly different), as shown in Fig. 2-8b. The exponent  $\alpha \approx 0.3$  is consistent with the inertial wetting dynamics on other hydrophobic surfaces with similar equilibrium contact angle  $\theta_{eq} \approx 110^\circ$  [55]. In summary, I found that the early wetting on PDMS substrates was similar to that on rigid hydrophobic surfaces and that wetting followed a power law within some characteristic time scales depending on the substrate softness.

---

### 2.3.2 Inertial wetting

---

The early wetting speed observed in the experiments was typically of the order of  $\sim 0.5$  m/s, which was much faster than the viscoelastic wetting velocity on soft substrates observed by Carré and Shanahan (of the order of  $10^{-4}$  m/s or less) [26, 27, 33, 34, 37, 65]. This indicates that the early wetting dynamics was independent of substrate softness and only viscosity or inertia resisted wetting. If inertia dominates the dynamics, i.e. the surface energy is transferred into the kinetic energy of the moving drop, the spreading radius could be expressed as  $r = g(F, m, t, \theta_{eq})$ .  $F$  is the capillary driving force, which scales as  $\gamma R_0$ ,  $m$  is the mass of the drop equal to  $\rho R_0^3$ , and  $g(\ )$  is some function. The characteristic time of any inertial processes is  $\tau_i = \sqrt{\frac{mL^*}{F}}$ , with  $L^*$  a characteristic length. For capillary driven inertial wetting, the

characteristic time should be  $\tau_i = \sqrt{\frac{\rho R_0^3}{\gamma}}$ . Thus, one could derive that inertial wetting follows

$$\frac{r}{R_0} = g\left(\frac{t}{\tau_i}, \theta_{eq}\right) \quad (2.2)$$

Similarly, one can derive that viscosity dominated wetting follows

$$\frac{r}{R_0} = g\left(\frac{t}{\tau_v}, \theta_{eq}\right) \quad (2.3)$$

Here,  $\tau_v = \frac{\mu R_0}{\gamma}$  is the characteristic viscous time.

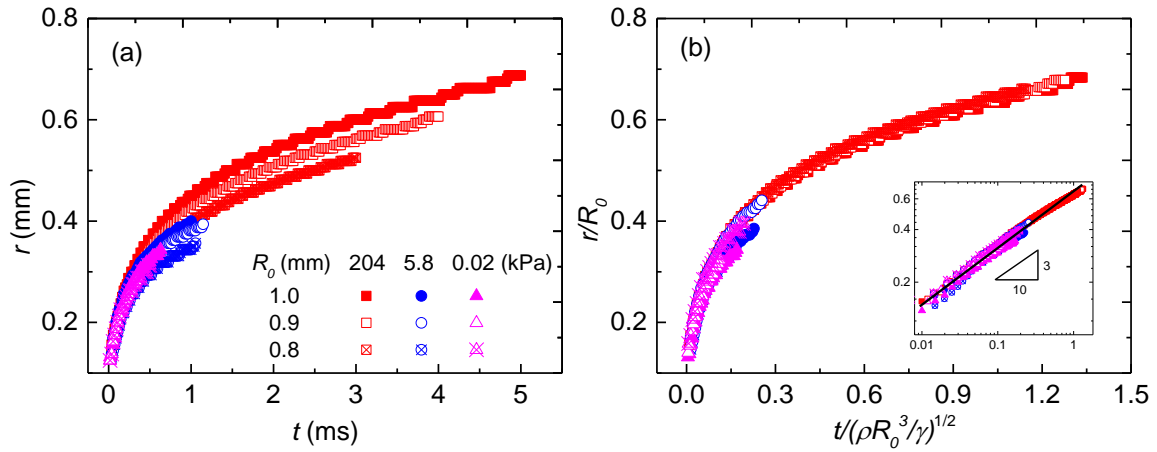


Figure 2-9 (a) Plot of  $r$  vs.  $t$  for the fast wetting process of three drop sizes. (b)

Rescaling of the plot by drop radius  $R_0$  and characteristic inertial time  $\tau_i = \sqrt{\frac{\rho R_0^3}{\gamma}}$ .

The inset figure is the plot in log-log scale.

Figure 2-9a shows the increase of the early spreading radius of water drops with different initial radii on three soft PDMS substrates when  $t \leq \tau_T$ . The spreading was faster for larger drops. By normalizing the spreading radius with the initial radius,  $R_0$ , and the spreading time with the characteristic inertial time,  $\tau_i = \sqrt{\frac{\rho R_0^3}{\gamma}}$ , all curves collapse onto one master curve, as shown in Fig. 2-9b. Similar results were reported by *Bird et al.* for water on different wettable surfaces [55]. In contrast, I cannot collapse the same data by normalization with the characteristic viscous time,  $\frac{\mu R_0}{\gamma}$ , as illustrated in Fig. 2-10. These results confirm that the early wetting dynamics



of drops on soft substrates is dominated by inertia and not by viscosity. Indeed, the spreading follows a power law with an exponent of 0.3 which is much larger than 0.1 for viscous wetting.

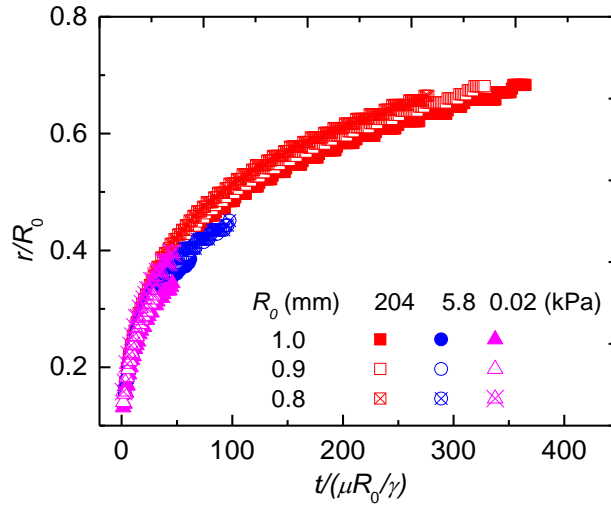


Figure 2-10 Normalized spreading radius,  $r/R_0$ , vs. the normalized spreading time,  $t/(\frac{\mu R_0}{\gamma})$ .

### 2.3.3 Inertial wetting exponent

In the inertial wetting stage, the exponent of the power law is only dependent on the chemical interaction between liquids and surfaces, i.e. on  $\theta_{eq}$ . During the spreading, the change of surface energy is transformed into the kinetic energy of the moving drop and is a motor for wetting. Thus, wetting on high energy surfaces should be faster than on low energy surfaces, i.e.  $\alpha$  decreases with increasing  $\theta_{eq}$ . In this experiment, it was difficult to modify the chemical properties of PDMS substrates while keeping similar mechanical properties. Therefore, I changed the surface tension of the wetting liquids instead of surface wettability, which was equivalent. Therefore, water/ethanol and water/glycerol mixtures with different mass proportions were used to obtain liquids with a wide range of surface tensions (from 22.3 to 72.7 mN/m), viscosities (from 0.89 to 10.8 mPa·s), and equilibrium contact angles (from 41 to 114°). The contact angles were measured on a “rigid” PDMS surface with  $G = 510$  kPa, as summarized in Table 2-1. Figure 2-11a shows the exponent  $\alpha$  for different

liquids spreading on different PDMS substrates during the early spreading stage. As expected, the exponent was similar for all liquids and independent on surface softness. Liquids with small surface tension showed a larger exponent than liquids with large surface tension, indicating that inertial spreading was faster for higher gains in surface energy, i.e. on more wettable liquids or surfaces. This is consistent with results on rigid surfaces [55]. It was further found that the exponent decreased with the equilibrium contact angle  $\theta_{eq}$ , as illustrated in Fig. 2-11b. These values match very closely those reported in the paper by Bird *et al.* on rigid surfaces. All exponents are smaller than 0.5, which is the value of  $\alpha$  for completely wetting surfaces or liquids [54, 55, 71].

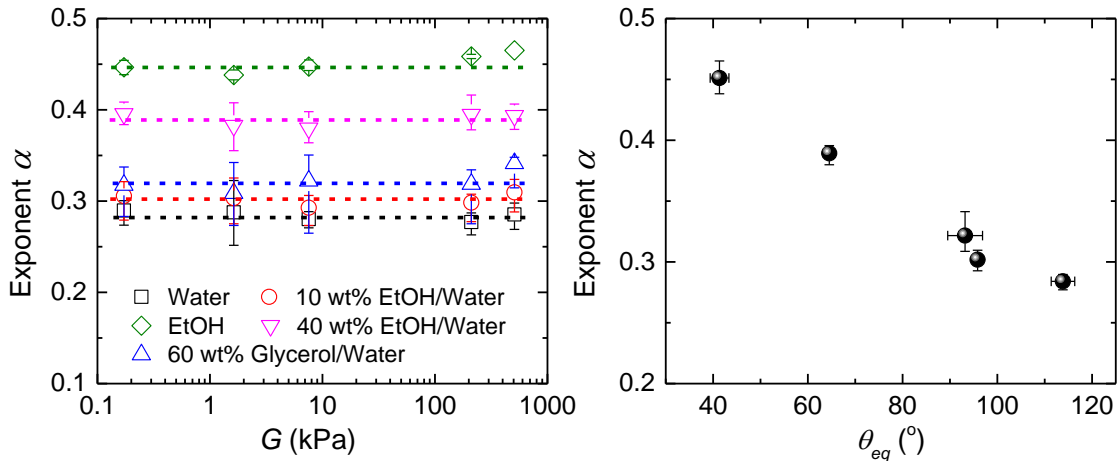


Figure 2-11 (a)  $\alpha$  for various liquids spreading on different soft substrates. (b)  $\alpha$  plotted as a function of contact angle  $\theta_{eq}$ .

When a drop is sitting on a soft substrate in equilibrium, a “wetting ridge” is formed near the contact line of the drop due to the vertical component of the liquid surface tension force,  $\gamma\sin\theta_{eq}$  [44, 51, 72-75], as sketched in Fig. 1-8a. Moreover, the Laplace, or capillary, pressure in the drop deforms the liquid-solid interface as well. Due to these deformations, the value of  $\theta_{eq}$  is difficult to determine with standard optical techniques on soft or deformable substrates, since it is very difficult to observe the actual solid-liquid-air contact line. In the experiment, I gently deposited a 4  $\mu\text{L}$  water droplet on three soft substrates. The equilibrium shape of the droplet when the “apparent” triple phase contact line stopped moving is shown in Fig. 2-12. On

relatively rigid substrates ( $G \gtrsim 5.8 \text{ kPa}$ ), the surface shape of the drop was still spherical. In contrast, on the softest substrate ( $G = 0.02 \text{ kPa}$ ), the drop was not spherical any more, especially for the area near the “apparent” contact line (Fig. 2-12). The measured macroscopic “apparent” equilibrium contact angles on the substrates with  $G = 0.02, 5.8$  and  $204 \text{ kPa}$  were  $\theta_{eq} = 23 \pm 3^\circ, 90 \pm 2^\circ$  and  $109 \pm 1^\circ$ , respectively. Intrinsically, these three surfaces should have similar  $\theta_{eq}$  for water since they have a similar chemical surface composition. Thus, measuring the equilibrium contact angle or trying to directly apply Young’s equation, yields poor information on the surface energy of soft substrates. Nevertheless, the early stage of spontaneous spreading showed similar dynamics (Fig. 2-11a) and was only dependent on wettability (Fig. 2-11b). Therefore, the wetting exponent  $\alpha$  could be used to characterize dynamically the wettability of soft substrates, for which Young’s equation cannot be directly applied.

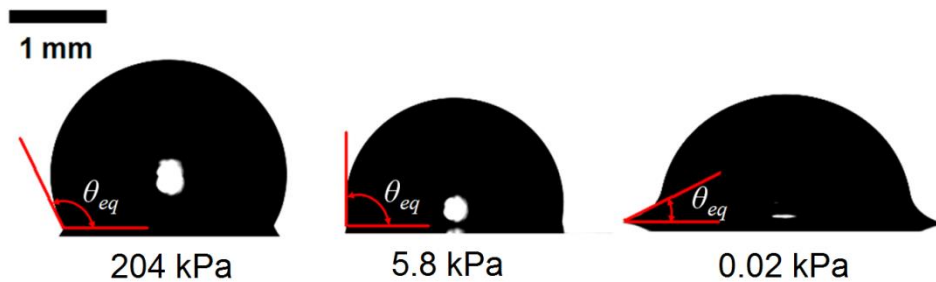


Figure 2-12 The equilibrium shape of water drops on the substrates with  $G = 0.02, 5.8$  and  $204 \text{ kPa}$ .

### 2.3.4 Inertial wetting time on “soft” PDMS substrates

In sections 2.3.1-2.3.3, it was concluded that the initial wetting dynamics on soft substrates was dominated by inertia, as it was for hard surfaces. However, I found that the surface softness strongly influenced the duration of early inertial spreading (see Fig. 2-8a & b). Figure 2-13 summarizes the inertial spreading time  $\tau_T$  of various liquids on all soft PDMS substrates and on hydrophobic glass surfaces. On the softest substrates ( $G \lesssim 5.8 \text{ kPa}$ ), this spreading time for a water drop was less than 1 ms. It did increase slightly with the shear modulus, up to  $\sim 8 \text{ ms}$  on the harder substrate

( $G = 204$  kPa). On substrates with  $G \gtrsim 204$  kPa,  $\tau_T$  was independent on the surface softness. For liquids with surface tension slightly smaller than water, like 60 wt% glycerol/water or 10 wt% ethanol/water, the trend was similar, though  $\tau_T$  was slightly larger. However, if the surface tension was much smaller (40 wt% ethanol/water or pure ethanol), the inertial spreading time was independent on surface softness. The duration of the inertial spreading time  $\tau_T$  was inversely proportional to the surface tension of the liquid, but in a non-trivial way.

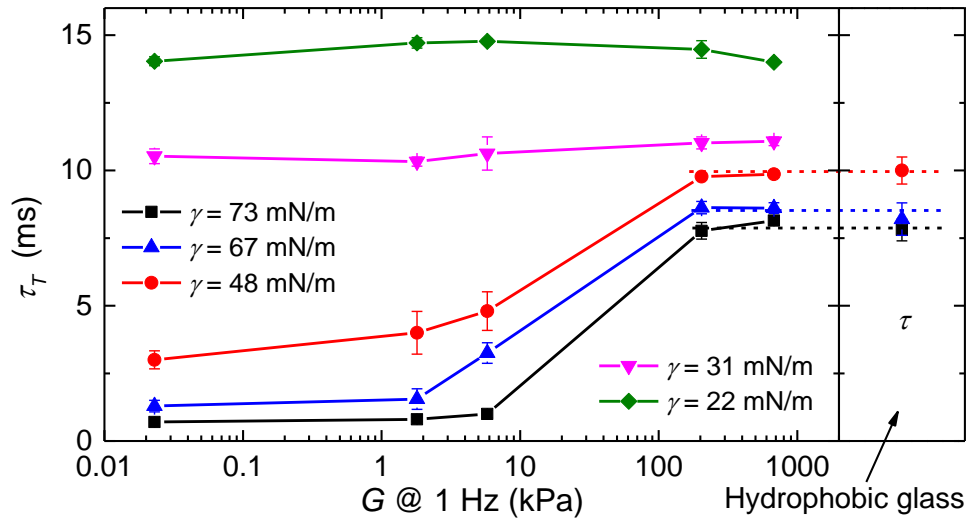


Figure 2-13 Transition times  $\tau_T$  as function of  $G$  and  $\gamma$  for various liquid surface tensions on soft substrates (left) and inertial wetting times  $\tau$  on hydrophobic glass for three different liquids (right).

The influence of substrate softness on  $\tau_T$  is remarkable. In a first step, I will give a qualitative explanation. I attribute this phenomenon to the balance between driving force for the formation of the ridge, i.e. the vertical component of the surface tension, and the viscous dissipation in the PDMS acting against a fast ridge formation. The height of the ridge depends on the vertical force and the time available to deform the surface. At any given point on the surface a ridge only forms if the contact line is close enough. In a simple picture, the height of the ridge should depend on the transit time of the contact line over a typical width of the ridge, i.e. on the speed of the contact line  $U = dr/dt \sim t^{\alpha-1}$ . The contact line velocity decreases with time. Upon first contact with the surface the contact angle of the drop is very large ( $\sim 160^\circ$ , see

Fig. 2-7). Since also the contact line speed is high, the “wetting ridge” due to the vertical component of the surface tension force  $\gamma_{\perp} = \gamma \sin\theta$  is still small and the drop is not hindered in its spontaneous spreading under the action of the horizontal force  $\gamma(\cos\theta - \cos\theta_{eq})$ . With ongoing spreading, the contact angle decreases and the horizontal force decreases; the vertical component of surface tension force increases, the contact line speed decreases, and the wetting ridge grows; and the friction force on the contact line due to viscoelastic braking increases. For soft substrates, thus, a critical  $\gamma_{\perp}$  does exist below which the substrate is not deformed sufficiently to affect inertial drop spreading (Fig. 2-13) [38]. This value depends on the balance between vertical force, velocity of the contact line, and viscous behavior of the PDMS. While  $\gamma_{\perp}$  is below the critical value, inertial spreading occurs, but a small ridge will start forming. I observed that when  $\gamma_{\perp}$  reached the critical value inertial spreading still continued for some time  $\Delta\tau$ . During this time the drop spread with a constant advancing angle. Eventually, the contact line velocity is low enough to allow for the formation of a high enough wetting ridge, and inertial spreading stops.

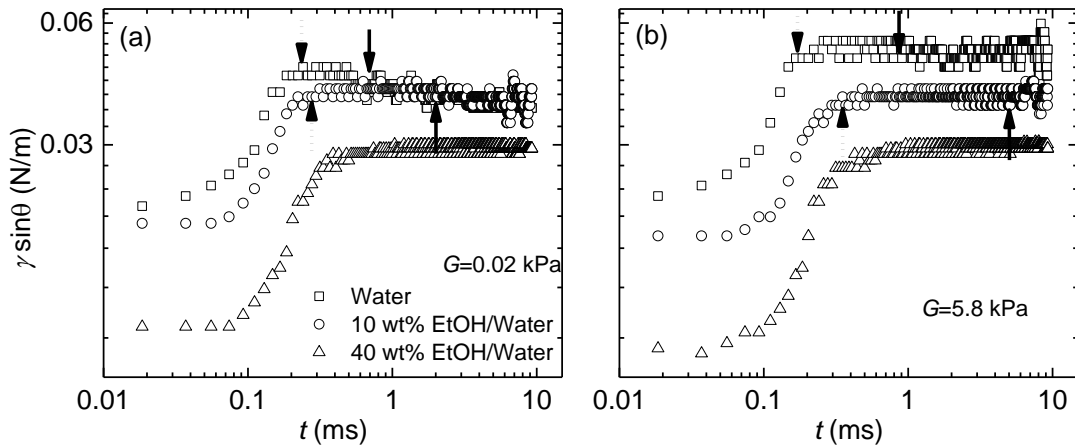


Figure 2-14 Vertical component of surface tension force  $\gamma_{\perp}$  during wetting on two soft substrates (a)  $G = 0.02$  kPa and (b)  $G = 5.8$  kPa. The radius of the drop is 1.0 mm. The dashed and solid arrows indicate the time to reach the maximum  $\gamma_{\perp}$  and the end of inertial wetting time between which  $\Delta\tau$  is defined.

Figure 2-14a-b shows the vertical component of surface tension force of droplets of three liquids on substrates with  $G = 0.02$  and 5.8 kPa.  $\gamma_{\perp}$  reached a

---

maximum value within 0.2 – 0.3 ms (indicated by dashed arrows) and thereafter remained constant at least until inertial spreading stopped (indicated by solid arrows). For the 10 wt% ethanol/water mixture and for water, the maximum  $\gamma_{\perp}$  was  $\sim 0.039$  and  $\sim 0.043$  N/m (equal or larger than the critical  $\gamma_{\perp}$ ), respectively, and the inertial time  $\tau_T$  was  $\sim 0.5$  and  $\sim 1.0$  ms on the substrate with  $G = 0.02$  kPa (Fig. 2-13). In contrast, the drop of 40 wt% water/ethanol had a maximum  $\gamma_{\perp}$  of  $\sim 0.028$  N/s (smaller than the critical  $\gamma_{\perp}$ ) and  $\tau_T$  was comparable to that on “rigid” surfaces (Fig. 2-13). A similar trend was also observed on the slightly harder substrates ( $G = 5.8$  kPa) (Fig. 2-14b). These results are consistent with the earlier hypothesis.

For liquids with a maximum  $\gamma_{\perp}$  larger than the critical value, Figure 2-14a-b also indicates that the inertial wetting time  $\tau_T$  is longer for liquids with smaller surface tension or on harder substrates and  $\tau_T$  is shorter for liquids with larger surface tension or on softer substrates. This is plausible, since pulling out a ridge of a defined height on similarly soft substrates is faster by applying a large rather than a small force. It should be pointed out that inertial spreading does not stop immediately when the vertical component of the surface tension force reaches a maximum  $\gamma_{\perp}$  larger than the critical value, and spreading continues for some time  $\Delta\tau$  (Fig. 2-14a-b). This depends on the fact that the material is not purely elastic, but viscoelastic. The two PDMS substrates considered here have  $G = 0.02$  and  $5.8$  kPa with respective phase angles  $\delta = 83.1$  and  $15.8^{\circ}$ . As mentioned above, also the time over which the force is applied plays a role. In fact, a complete model would include the time dependent vertical component of the surface tension force, the motion of the contact line and the viscoelastic response of the PDMS on the localized force due to the moving contact line. Such a model will be proposed in the later sections.

---

### 2.3.5 Inertial wetting time on “rigid” PDMS surfaces

---

If the substrate is relatively rigid or the surface tension of the liquid is relatively small, the formed wetting ridge could be too small to influence the dynamic wetting. Eventually, some surfaces will behave like “rigid” surfaces. Indeed, as shown in Fig. 2-13, the spreading of all liquids was similar to that on hard surfaces when  $G \gtrsim 204$  kPa or  $\gamma \lesssim 30.7$  mN/m. Since the early capillary driven wetting is compensated by inertial

force, the duration of wetting  $\tau$  for these cases should be close to the characteristic time scale of inertial phenomenon,  $\tau_i = \sqrt{\frac{\rho R_0^3}{\gamma}}$ . However, it was found that  $\tau$  was always larger than  $\tau_i$  for all these experiments. Similar results were also reported by Bianche *et al.* [54] and Bird *et al.* [55].

Bianche *et al.* proposed a model to predict  $\tau$  based on the transition from inertial to viscous wetting stage for complete wetting [54]. They concluded that the inertial wetting stops earlier for high than for low viscous liquids. However, in the experiments here, I did not observe the viscous wetting stage in all wetting experiments. These results indicate that Bianche *et al.*'s model is not applicable here.

Bird *et al.* suggested that the duration of inertial spreading was set by the capillary wave propagating along the droplet [55]. When a drop starts spreading, the capillary wave generated upon contact with the surface at the bottom of the drop propagates upwards to the top of the drop (see Fig. 2-7), and then back again. In the course of capillary wave dynamics, there is a critical wavelength,  $\lambda_c = 2\pi \sqrt{\frac{\gamma}{\rho - \rho'}}$ , below which the propagation of the capillary wave is only dominated by surface tension [76-78].  $\rho'$  is the density of surrounding fluid. For the air-water interface,  $\lambda_c$  is about 17 mm. This is much larger than the maximum size of droplets used here. In the simplest picture this surface wave can be considered to be the lowest order eigen mode of the drop. Lamb [77] did show that the frequency of the eigen modes of a freely suspended drop of a inviscid liquid surrounded by a much lower density fluid is given by

$$\omega = \frac{2\pi}{\tau_l} = \sqrt{\frac{l(l-1)(l+2)}{\rho R^3} \gamma} = \frac{\sqrt{l(l-1)(l+2)}}{\tau_i} \quad (2.4)$$

where  $l$  is the mode number ( $l = 2$  being the lowest mode and corresponding to ellipsoidal drop vibration). The period of the lowest mode,  $\tau_2$ , is thus expected to be

$$\tau_2 = \frac{2\pi}{2\sqrt{2}} \tau_i \approx 2.22 \tau_i \quad (2.5)$$

Figure 2-15 shows results from various drop sizes and liquids on soft substrates.  $\tau$  is linearly dependent on  $\tau_i$ , and  $\tau = (2.6 \pm 0.14)\tau_i$  from fitting the experimental data points. The linear dependence of the inertial wetting time  $\tau$  on the characteristic

time  $\tau_i$  is consistent, in a first approximation, with the picture of similar time scales of capillary wave propagation  $\tau_2$  and inertial wetting  $\tau$ . The difference between  $\tau$  and  $\tau_2$  may have two reasons. First, drop vibrations in contact with the surface were damped, which would result in  $\tau > \tau_2$ . Second, during spreading the contact radius of the drop constantly grew. These result in decreasing the drop resonance frequency and in slowing down the propagation of the capillary wave. This leads to  $\tau > \tau_2$ .

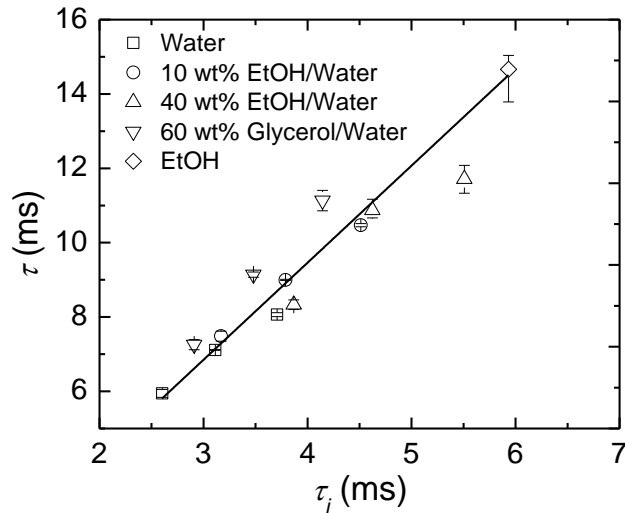


Figure 2-15 The actual inertial time  $\tau$  of various liquids is plotted as a function of the characteristic inertial time  $\tau_i$ . The slope of the linear fitting is  $2.6 \pm 0.14$ .

### 2.3.6 Effects of film thickness

Recently, Pericet-Camara *et al.* found that the vertical extrusion of the “wetting ridge” on soft substrates can be affected by the rigid solid supporting the PDMS film, if the film is thinner than a critical thickness [44]. This could influence spreading, as the friction force or viscoelastic dissipation due to the wetting ridge may be different for different thickness. In the experiments, measurements were done with soft PDMS films of  $d = 30, 100$  and  $200 \mu\text{m}$  thickness, as well as substrates that could be considered semi-infinite. As shown in Fig. 2-16, during the fast inertial spreading of water drops, both the exponent  $\alpha$  and the time  $\tau_T$  were independent on film thickness. This does make sense. During the fast spreading, or in other word, under high frequency stress - if we treat the spreading process as a rheology process - the substrate behaves as a rigid, non deformable substrate. The typical frequency here is



$\sim 10^5$  Hz, which would correspond to a shear modulus of  $\sim 10^6$  Pa (Fig. 2.5). Thus, the “wetting ridge” that could be formed is very shallow. In summary, I did not find any influence of film thickness on early wetting dynamics and wetting ridge formation in my experiments.

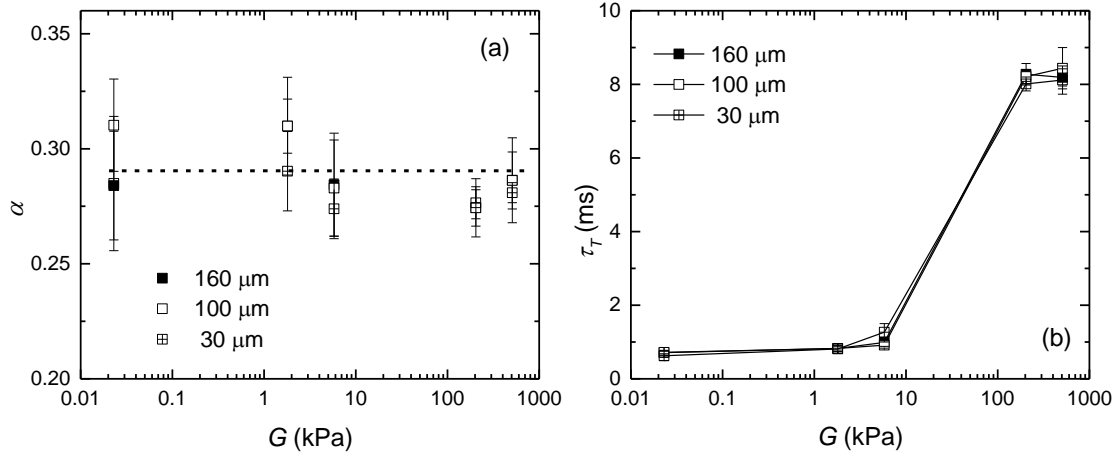


Figure 2-16 (a) The inertial exponent  $\alpha$  of 1.0 mm-radius water drop spreading on PDMS films with three different thickness. The corresponding inertial wetting time  $\tau_T$  is shown in (b).

## 2.4 Theoretical model

In this section, a simple model based on the balance of energy contributions during drop spreading will be presented. The theoretical model was developed in its main lines by Prof. Martin E.R Shanahan. I assisted him for model modifications and for its testing against my experimental results.

During the wetting, the main driving force is capillarity and the main braking (restraining) forces slowing down spreading are the kinetic energy of the spreading drop (i.e. inertia), viscous dissipation within the liquid, and viscoelastic dissipation in the deformed substrate. In early wetting dynamics, i.e. at the beginning of drop spreading, the Reynolds number is always larger than one, i.e.  $Re \gg 1$ , so that the viscous dissipation within the liquid could be neglected. Thus, the early wetting contains a fast inertial wetting stage and a slow viscoelastic wetting stage, which will be considered separately in the following sections.

### 2.4.1 Inertial wetting

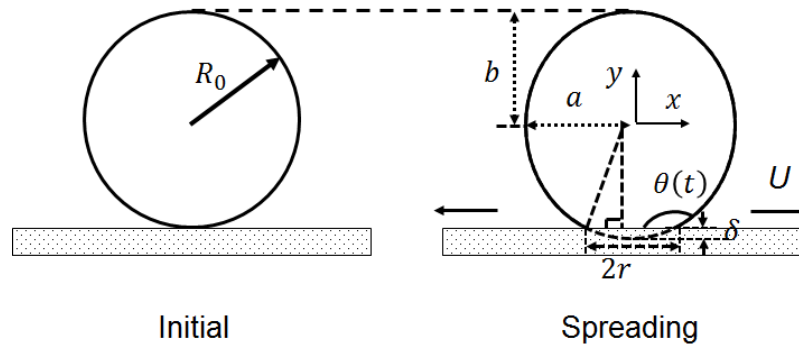


Figure 2-17 Schematic of a spreading drop on a surface with relevant notation.

In the literature, a number of partially empirical models were proposed to describe the early spreading of low viscosity drops on solid surfaces [54, 55, 79]. Bianco *et al.* treated the early wetting process on completely wetting surfaces as a liquid drop coalescence with a thin liquid film (precursor film) [54]. They derived a power law of  $r = K't^{0.5}$  which was confirmed by numerous experiments. However, this model is only applicable for completely wetting cases. Bird *et al.* found that the initial wetting on partial wetting surfaces is also dominated by inertia. They proposed a model based on energy balance during spreading, which predicts that the early inertial wetting follows a power law with the exponent depending on the equilibrium contact angle  $\theta_{eq}$  [55, 79]. However, this model could not give a clear description of the relationship between  $\alpha$  and  $\theta_{eq}$ , or show the limit value of  $\alpha$ . Here, a scaling discussion about the (early) inertial stage is engaged based on the existing work [54, 55, 79].

In the early wetting stage, the viscous dissipation in the drop and the viscoelastic dissipation in the surface are negligible. A dynamic balance is established between capillary and kinetic energy. Assuming that in the initial stages the drop remains essentially spherical, but for a slightly flattened contact region with the substrate (Fig. 2-17), the mass of liquid entrained is given by  $\sim k\rho r^4/R_0$  [54, 80, 81].  $\rho$  is liquid density and  $k$  is of order  $\pi/4$ . Given the changing form of the travelling liquid body, its average speed is of order  $\dot{r}/2$ , leading to a kinetic (inertial) spreading force term of

$$F_K \approx \frac{d}{dt} (\pi \rho r^4 \dot{r} / 8R_0) \quad (2.6)$$

To within the multiplicative constant  $\pi/8$ , which is anyway only approximate, this is of the form which has been shown previously [54, 55].

The capillary spreading force implemented here is slightly different from the form in the literature. The drop is initially spherical and the volume of the drop remains constant during the spreading. After the spreading starts, the bottom of the drop becomes flattened (Fig. 2-7). As a result, the spreading drop can be treated as a truncated prolate ellipsoid with a missing cap of height  $\delta$  and radius  $r$  (Fig. 2-17). The equatorial radius is  $a$  and the polar radius is  $b$ . With a simple geometrical relationship, the height of the cap can be estimated by

$$\delta \approx \frac{r^2}{2R_0} \text{ or } \delta \approx R_0(1 + \cos \theta) \quad (2.7)$$

Combining the above two equations, the dynamic contact angle can be written as

$$\cos \theta(t) \approx \frac{r^2}{2R_0^2} - 1 \quad (2.8)$$

Inserting equation (2.8) into equation (1.12), the capillary force can be written as

$$F_C \approx 2\pi r \gamma (\cos \theta_{eq} - \cos \theta(t)) \approx 2\pi r \gamma \left( 1 + \cos \theta_{eq} - \frac{r^2}{2R_0^2} \right) \quad (2.9)$$

The second approximate expression is only valid for small  $r$ , or equivalently for large  $\theta(t)$ . This condition is satisfied for in the experiments. Balancing  $F_K$  and  $F_C$  one obtains the governing equation of inertial wetting,

$$2\pi r \gamma \left( 1 + \cos \theta_{eq} - \frac{r^2}{2R_0^2} \right) - \frac{d}{dt} (\pi \rho r^4 \dot{r} / 8R_0) \approx 0 \quad (2.10)$$

In the very first instants,  $r \ll R_0$  and  $1 + \cos \theta_{eq} \gg \frac{r^2}{2R_0^2}$ . Equation (2.10) can then be simplified to

$$2\pi r \gamma (1 + \cos \theta_{eq}) - \frac{d}{dt} (\pi \rho r^4 \dot{r} / 8R_0) \approx 0 \quad (2.11)$$

The above equation recovers the classic scaling law  $r \sim K't^\alpha$  by Bianco *et al.*, where  $\alpha \approx 0.5$ . Clearly, as  $r$  increases, simple scaling becomes impossible, but the effective value of  $\alpha$  becomes smaller. The value of  $r/R_0$  for which  $\alpha$  is no longer acceptable depends on the value of  $\cos \theta_{eq}$ , which occurs earlier for larger values of

$\theta_{eq}$ . However, it is difficult to derive the exact relationship between  $\alpha$  and  $\theta_{eq}$ . Nevertheless, one can estimate the range of  $\alpha$ . As spreading proceeds, the contact angle decreases and approaches the equilibrium contact angle  $\theta_{eq}$ . For hydrophobic surfaces, the dynamic contact angle is nearly constant and is very close to the equilibrium contact angle [66]. Thus, taking the limit as  $\theta \rightarrow \theta_{eq}$ , one finds

$$\frac{d}{dt}(\pi\rho r^4\dot{r}/8R_0) \approx 0 \quad (2.12)$$

which suggests that the limiting lower value of  $\alpha$  should be 0.2. This is, at least qualitatively, in agreement with previous work [55], including the more recent contribution [52], but was derived on different assumptions.

#### 2.4.2 Viscoelastic wetting

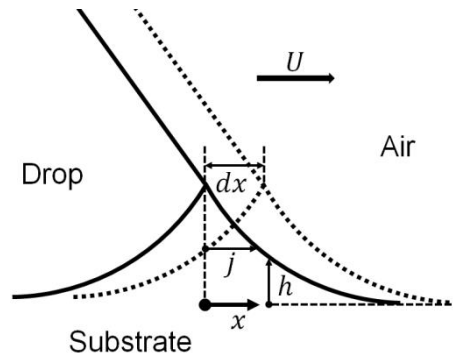


Figure 2-18 Zoom-in view of the moving contact line on soft substrate.

In the viscoelastic wetting stage, the driving surface energy is dissipated by viscoelastic friction in the soft film. It is well known that the wetting ridge near the contact line has a vertical displacement of  $h(x, \theta)$  and a radial displacement of  $j(x, \theta)$  (Fig.2-18). For a contact line moving a length of  $dx$  at speed  $U$ , the work done is [26]

$$F_{VE} = 2\pi r \gamma U \left( \left| \frac{dh}{dx} \right| \sin \theta + \left| \frac{dj}{dx} \right| \cos \theta \right) \quad (2.13)$$

The above equation can be further estimated as  $F_{VE} \approx \frac{r\gamma^2 U}{G\varepsilon}$  [26].  $\varepsilon$  is a cutoff length near the TPCL (typically of order  $\sim 0.1$  to  $\sim 1 \mu\text{m}$ ). For the viscoelastic dissipation, only a certain fraction  $\Delta$  ( $0 \leq \Delta \leq 1$ ) of the strain energy is dissipated and the remaining fraction  $(1 - \Delta)$  is recovered [82]. Thus, the effective viscoelastic dissipation energy is

$$F_{VEE} \approx \frac{r\gamma^2 U}{G\varepsilon} \Delta \quad (2.14)$$

For the extremely low speed viscoelastic wetting stage, Shanahan and Carré adopted a power law for the fraction of the viscoelastic energy dissipation,  $\Delta = (\frac{U}{U^*})^{\alpha''}$ , based on experimental adhesion results [26, 27, 33, 34, 37]. Where  $U^*$  is a characteristic speed and  $\alpha''$  has a value of 0.5-0.6. However, this is not directly applicable to the high spreading speeds arising in this work. Here, the standard linear solid model of viscoelasticity is adapted [83], in which the dissipation energy fraction can be estimated as  $\Delta \approx \frac{\varphi\omega\tau_R}{(1+\omega^2\tau_R^2)}$  and the viscoelastic dissipation term is obtained,  $F_{VEE} \approx \frac{r\gamma^2}{G} \frac{\varphi\omega\tau_R}{(1+\omega^2\tau_R^2)}$ .  $\varphi \approx \frac{G_u - G_r}{\sqrt{G_u G_r}}$  is a parameter depending on the unrelaxed ( $G_u$ ) and the relaxed ( $G_r$ ) shear modulus of the substrate and is of order unity,  $\tau_R$  is the relaxation time of the viscoelastic substrate, and  $\omega$  is the angular frequency from dynamic measurements. The angular frequency can be related approximately to spreading speed with  $\omega \approx \pi U/2\varepsilon = \pi\dot{r}/2\varepsilon$ .

Balancing  $F_C$  and  $F_{VE}$ , the new governing equation takes a form of

$$2\pi r\gamma \left( 1 + \cos \theta_{eq} - \frac{r^2}{2R_0^2} \right) - \frac{r\gamma^2}{G\varepsilon} \frac{\varphi\omega\tau_R}{(1+\omega^2\tau_R^2)} \approx 0 \quad (2.15)$$

Substituting for  $\omega$  and considering sufficiently low velocity, as is the case at the transition between inertial and viscoelastic spreading, Equation (2.15) can be simplified to

$$2R_0^2(1 + \cos \theta_{eq}) - r^2 \approx \frac{R_0^2\gamma\varphi\tau_R}{2G\varepsilon^2} \dot{r} \quad (2.16)$$

Redefining  $\frac{R_0^2\gamma\varphi\tau_R}{2G\varepsilon^2} = \psi$ , and  $2R_0^2(1 + \cos \theta_{eq}) = \xi^2$ , Equation (2.16) can be finally written as  $\xi^2 - r^2 \approx \psi\dot{r}$ . The solution of this differential equation is

$$\frac{1 - \frac{r}{\xi}}{1 + \frac{r}{\xi}} = e^{-\frac{2\xi}{\psi}t} \quad (2.17)$$

During the viscoelastic stage,  $r/\xi \ll 1$  and the left term of equation (2.17) can be expressed as  $\left(1 - \frac{r}{\xi}\right)^2$ . Thus, the final expression of the viscoelastic spreading law is

$$r \sim \xi \left( 1 - e^{-\frac{\xi}{\psi} t} \right) = R_0 \sqrt{2(1 + \cos \theta_{eq})} \left[ 1 - e^{-\left( \frac{\sqrt{2(1 + \cos \theta_{eq})} 2G \varepsilon^2}{\gamma \varphi \tau_R R_0} \right) t} \right] \quad (2.18)$$

This spreading equation predicts that in this viscoelastic stage, spreading is faster on substrates with larger  $G$ , when all other parameters remain the same.

---

### 2.4.3 Inertial to viscoelastic transition

---

The crossover from inertial to viscoelastic spreading takes place when inertial and viscoelastic spreading radii cross, i.e. when

$$K' t^\alpha \sim \xi \left( 1 - e^{-\frac{\xi}{\psi} t} \right) \quad (2.19)$$

Solving this equation for  $t$  should yield an estimate of the crossover time  $\tau_T$ . I must point out here that the above equations are only approximate solutions and that some of the parameters, such as  $\dot{r}$ ,  $\theta$ ,  $G$ , and  $\omega$ , vary during spreading while others, such as  $\varphi$  and  $\tau_R$ , are themselves simplifications whose value cannot be determined accurately. In fact, a whole spectrum of relaxation times is present at any given moment during drop spreading: the closer to the TPCL, the smaller is the relaxation time and the faster is the relaxation. Moreover, the power law for inertial wetting is partially empirical. There is still no theory that can be used to calculate  $K'$  and  $\alpha$ . Nevertheless, it is believed that the equations derived for the two spreading stages capture the main physics involved in the spreading of a low-viscosity drop on a viscoelastic substrates. There are two reasons for such a conclusion:

- (i) For inertial spreading, a scaling law with an explanation why the spreading exponent  $\alpha$  changes with the equilibrium contact angle  $\theta_{eq}$  was derived. The predicted limiting value of  $\alpha$  is consistent with all existing experimental findings.
- (ii) For viscoelastic spreading, the exponential decay links the most relevant rheological parameters of the material to the spreading dynamics. The influence of substrate viscoelasticity on wetting is captured by the derived wetting law.

---

Here, the crossover time was determined by asymptotically matching the experimental spreading radii with the power law,  $K't^\alpha$ , for the inertial stage and with equation (2.18) for the viscoelastic stage. The unknown parameters listed above were handled as follows:

1.  $K'$  and  $\alpha$  were fitted by LSM on experimental data.
2. I could not determine independently  $\varphi$  and  $\tau_R$ , thus the term  $\varphi\tau_R$  was chosen as a fitting parameter.
3.  $\xi$ , the drop contact radius at the end of the viscoelastic spreading stage, could not be determined as the viscoelastic wetting stage may last up to a few hours [38]. As a result, it was also determined from a fit to the experimental curves.
4. The frequency at the inertial to viscoelastic transition,  $\omega_T$ , was used in the calculation.  $\omega_T$  was calculated using the transition speed,  $\dot{r}_T$ , measured at the crossover between inertial and viscoelastic spreading, and a cutoff length of  $\varepsilon = 1 \mu\text{m}$ . Then, the corresponding  $G(\omega_T)$  from independent rheological measurements can be obtained in Fig. 2-5.

Since the transition between inertial and viscoelastic spreading was observed for liquids with a relatively high surface tension, the fitting was carried out only for these cases. Figure 2-19a shows the experimentally obtained spreading radius of water drops in the transition zone, along with the fitted curves for inertial and viscoelastic spreading vs time. The fitting parameters were set so that inertial and viscoelastic curves met at one point, i.e. at  $\tau_T$ . This is indicated by arrows. Figure 2-19b compares experimental and calculated  $\tau_T$  for all different liquids and substrates used. With the same liquid, the calculated  $\tau_T$  increased with  $G$ , which is consistent with experiments and with equation (2.18). The  $\tau_T$  obtained from fitting agree within an order of magnitude or better with experimental times. The agreement is best for the softer substrates, while for the more rigid substrates the calculated  $\tau_T$  deviates from the measured values. The more rigid substrates no longer behaved completely viscoelastic under the spreading drop and in this case the inertial spreading time was better described by the characteristic time  $\tau$  for rigid, undeformable substrates. Another clear trend in agreement with equation (2.18) is that  $\tau_T$  was larger for liquids with smaller surface tensions. In the range of low viscosities employed, I could not

find a relation between  $\tau_T$  and the viscosity of the liquid, as was found by Bianco *et al.* [54].

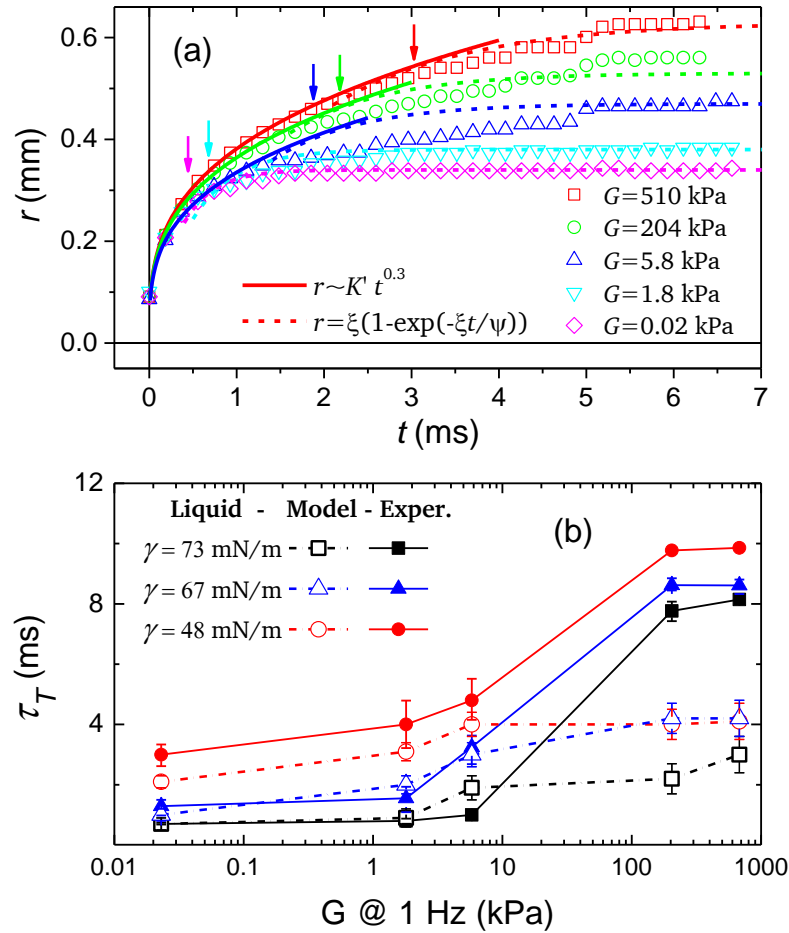


Figure 2-19 (a) Spreading radii of water drops (colour symbols) on different viscoelastic substrates and asymptotic fits to the inertial (solid lines) and viscoelastic (dashed lines) parts of the curves. Only each 10<sup>th</sup> data point is shown; (b) comparison of all calculated and measured  $\tau_T$  as function of  $G$ .

All the used or fitted parameters are listed in Table 2-2a-c. The fitted equilibrium contact radius,  $\xi$ , is in the order of 0.1 mm and decreases with  $G$  for each liquid. This matches my experimental observations. For relatively soft substrates, the “wetting ridge” is higher than for relatively rigid substrates, which leads to stronger viscoelastic dissipation and eventually a smaller wetting radius. The fitting parameter  $\varphi\tau_R$  has a value ranging from  $\sim 7 \cdot 10^{-5}$  to  $\sim 7 \cdot 10^{-7}$  s (see Table 2.2). If  $\varphi$  is taken to be



---

of order unity, the relaxation times derived from fitting are consistent with the estimated relaxation times of relatively rigid substrates ( $G \gtrsim 204$  kPa) using the Maxwell model. For relatively soft substrates ( $G < 204$  kPa), the fitted relaxation time is one to two orders of magnitude smaller than the estimated time. This is reasonable for such soft polymers as both  $\varphi$  and  $\tau_R$  change during drop spreading. In summary, the model captures the main physics of the dynamics of drop spreading and with reasonable fitting parameters the predicted  $\tau_T$  matches with experimental observations better than in the order of magnitude.

---

## 2.5 Summary

---

In this chapter, the early dynamic wetting of various liquids on soft substrates was studied. It was found that the early wetting dynamics on soft surfaces is also dominated by inertia. The spreading radius grew with spreading time according to a power law,  $r = K't^\alpha$ , with  $\alpha$  being only dependent on the equilibrium contact angle,  $\theta_{eq}$ . Since a “wetting ridge” was always formed near the contact line of a drop sitting on a soft substrate, it was hard to detect the actual contact angle and the Young’s equation was not directly applicable to soft substrates. Thus, the study of inertial wetting exponent provided a new method to characterize the wettability of soft substrates.

As the spreading proceeded, the wetting speed decreased. Thus, viscoelastic effects outweighed inertia and dominated the wetting dynamics in the following stage. The transition between the inertial and viscoelastic stages was dependent on substrate softness and on capillarity, which could be described by a simple model based on linear model of viscoelasticity proposed by Prof. Martin E.R. Shanahan.

Table 2-2 The fitting parameters for water, 60% glycerol/water and 10% ethanol/water drops spreading on PDMS substrates.

(a) Water drops spreading on PDMS substrates

Sample	$\dot{r}_T$ (m/s)	$r_T$ (m)	$\omega_T$ (rad/s)	$G(\omega_T)$ ‡(Pa)	$\mu_S(\omega_T)$ ‡(Pa s)	$\tau_R$ (s)‡	$\xi$ (m)	$\varphi\tau_R$ (s)	$t_T$ (Exp.*) (ms)	$t_T$ (The.*) (ms)
PDMS 1:10	0.072	4.8e-4	1.1e5	2.1e6	19	6.5e-5	6.3 e-4	5.7e-5	8.1	3.0
PDMS 1:20	0.084	4.0e-4	1.3e5	1.1e6	9	2.0e-5	5.3 e-4	1.7e-5	7.8	2.2
PDMS 1:50	0.097	3.4e-4	1.5e5	0.5 e6	4	4.4e-6	4.7 e-4	5.8e-6	1.0	1.9
PDMS 1:75	0.117	3.1e-4	1.8e5	0.4e6	3	8.4e-7	3.8 e-4	1.3e-6	0.8	0.9
PDMS 1:100	0.132	3.0e-4	2.1e5	0.3e6	2	5.4e-7	3.4 e-4	8.0e-7	0.7	0.7

\* Error bars are in the figures; † rheology data are affected by an error up to 10%; ‡ values were calculated with Maxwell model,  $\mu_S/G$ .

(b) 60% Glycerol/water drops spreading on PDMS substrates

Sample	$\dot{r}_T$ (m/s)	$r_T$ (m)	$\omega_T$ (rad/s)	$G(\omega_T)$ ‡(Pa)	$\mu_S(\omega_T)$ ‡(Pa s)	$\tau_R$ (s)‡	$\xi$ (m)	$\varphi\tau_R$ (s)	$t_T$ (Exp.*) (ms)	$t_T$ (The.*) (ms)
PDMS 1:10	0.030	6.1e-4	4.7e4	1.8e6	43	2.4e-5	6.2e-4	7.0e-5	8.6	4.2
PDMS 1:20	0.030	5.3e-4	4.7e4	0.9e6	20	2.2e-5	5.5e-4	3.0e-5	8.6	4.2
PDMS 1:50	0.040	4.0e-4	6.3e4	0.3e6	6	2.0e-5	4.5e-4	6.3e-6	3.25	3.0
PDMS 1:75	0.069	3.3e-4	1.1e5	0.3e6	4	1.4e-5	4.1e-4	3.5e-6	1.55	2.0
PDMS 1:100	0.075	3.0e-4	1.2e5	0.2e6	2	1.3e-5	3.1e-4	7.0e-7	1.29	1.0

\* Error bars are in the figures; † rheology data are affected by an error up to 10%; ‡ values were calculated with Maxwell model,  $\mu_S/G$ .

(c) 10% Ethanol/water drops spreading on PDMS substrates

Sample	$\dot{r}_T$ (m/s)	$r_T$ (m)	$\omega_T$ (rad/s)	$G(\omega_T)$ ‡(Pa)	$\mu_S(\omega_T)$ ‡(Pa s)	$\tau_R$ (s)‡	$\xi$ (m)	$\varphi\tau_R$ (s)	$t_T$ (Exp.*) (ms)	$t_T$ (The.*) (ms)
PDMS 1:10	0.036	6.8e-4	5.6e4	1.9 e6	35	1.8e-5	7.0e-4	1.1e-4	9.9	4.1
PDMS 1:20	0.033	6.3e-4	5.2e4	0.9e6	18	1.9e-5	6.5e-4	4.8e-5	9.8	4.0
PDMS 1:50	0.029	5.4e-4	4.5e4	0.3e6	8	3.1e-5	5.8e-4	1.1e-5	4.8	4.0
PDMS 1:75	0.030	4.9e-4	4.7e4	0.2e6	6	3.3e-5	5.1e-4	5.1e-6	4.0	3.1
PDMS 1:100	0.038	4.6e-4	6.0e4	0.1e6	3	3.0e-5	4.6e-4	1.7e-6	3.0	2.1

\* Error bars are in the figures; † rheology data are affected by an error up to 10%; ‡ values were calculated with Maxwell model,  $\mu_S/G$ .

---

---

### 3 Dynamic Wetting of Micron-sized Particles<sup>4</sup>

---

In this chapter, I present a study on the early wetting dynamics of single micron-sized particles at the water-air interface. A home-made inverted particle interaction apparatus (I-PIA) allowed me to combine high time resolution (10  $\mu$ s) with sensitive particle displacement (10 nm) and force (10 nN) measurements. Unlike the wetting of large solid surfaces, the small particle was driven into the liquid by capillary forces after contact, which was called “snap-in” process. Both the snap-in time  $t_s$  and the snap-in force  $F_s$  of hydrophilic and hydrophobic glass particles were measured. It was found that the snap-in time was dominated by inertia and it was independent of particle wettability. The snap-in force, which originates from the capillary force, was larger for hydrophilic particles than that for hydrophobic particles. After the snap-in process, particles did not reach the equilibrium state yet, and instead a slower particle wetting started. This wetting stage with a much slower wetting speed may last up to months.

---

#### 3.1 Motivation

---

One type of complex solids is small particles. Due to their small size, the surface forces outweigh the body forces, i.e. the surface area to volume ratio is much larger than unity and dominates the interaction with liquids. Understanding the interaction between particles and liquid-vapor interfaces is of great importance for industrial applications such as flotation processes, water purification, the deinking of paper, and so on [84-89]. In nature, most microorganisms live in contact with liquid-vapor interfaces [90]. For instance, it is well known that bacteria adhere to and move along water-air interfaces [91]. As a result, the interactions between solid particles and liquid-vapor interfaces also attracted considerable interest from environmental engineers and biologists [91-94].

Many techniques have been used to study particle interface interactions in the past years [84, 85, 95, 96]. The most commonly employed direct methods are

---

<sup>4</sup> This chapter is based on “L. Q. Chen, L.-O. Heim, D. S. Golovko, E. Bonaccorso, *Snap-in dynamics of single particles to water drops*, Appl. Phys. Lett. **101**, 031601 2012”.

---

microsphere tensiometry [97, 98], atomic force microscopy (AFM) or colloidal probe technique (CPT) [99-101], or optical techniques [86, 102-104]. This short list is by no means exhaustive. Among these methods, the direct measurement of particle-interface interactions (attractive or repulsive) is only accessible by AFM or CPT. Indeed, the interaction between small particles and bubbles, drops, or thin liquid films has been investigated in recent years [87, 88, 99, 105-116]. In these studies, particles with radius  $R$  between 0.5 and 20  $\mu\text{m}$  were attached to the end of cantilevers and moved towards to or retracted from air bubbles [87, 88, 99, 105, 109, 110, 115], oil drops [107, 108, 116-118] or thin films on solid surfaces [105, 106, 111]. Typically, the force-distance curves which characterize the interaction force between the particle and the interface were recorded. Based on the evaluation of cantilever deflection, the contact angle between particles and bubbles or drops could be obtained [87, 88, 99-101, 105, 106, 109, 110, 112, 113, 115].

In contrast, the dynamic wetting process, which takes place spontaneously when a particle touches a liquid-vapor interface and snaps into it, received little attention by direct force measurements. One reason is the limited time resolution of cantilever deflection measurements (order of tens of milliseconds or more). Optical techniques have a better time resolution (order of milliseconds [98, 103, 104]), but suffer from the drawback that interaction forces cannot be directly measured. The inverted particle interaction apparatus (abbreviated as I-PIA) used in this study offers a high time resolution up to 10  $\mu\text{s}$  or better, with which an accurate investigation of early dynamic wetting of single particles can be carried out.

---

## 3.2 Experiments

---

### 3.2.1 Hydrophilic and hydrophobic colloidal probes

---

In the experiments, I investigated the dynamic wetting of single glass particles (glass-beads, Kisker Biotech GmbH & Co. KG, Steinfurt, Germany) with radius  $R$  in the range between 22 and 86  $\mu\text{m}$ . The particles were sintered on tipless AFM cantilevers with the help of Dr. Lars-Oliver Heim in the group (processes shown in Fig. 3-1). First, a thermal glue drop (Epikote 1004, from Shell, melting point is 80°C) was deposited

on a thermal stage at 120°C under the microscope. The tips of AFM cantilevers were brought into contact with the glue drop under optical microscope control with a three-axes hydraulic micromanipulator (Model MMO-203, from Narishige Ltd., Japan). When the cantilever was retracted from the drop, the glue was transferred onto the tip. Then, the particle was attached to the AFM tip once it touched the tips. After that, the particle-decorated cantilevers (colloidal probes) were put into a high temperature oven (Therm Oncept, Germany) for 1 hour at 800°C. Figure. 3-2 shows a SEM image of a colloidal probe with a glass particle with radius 86  $\mu\text{m}$ .

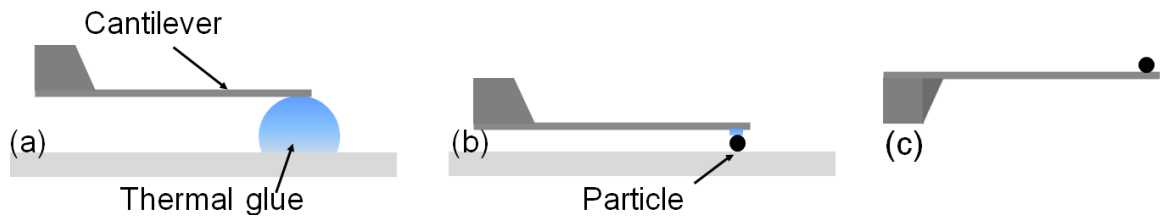


Figure 3-1 The processes of putting particles on cantilevers.

Before the measurements, the colloidal probes were first cleaned in acetone (Sigma-Aldrich, p.a.) and then in ethanol (Sigma-Aldrich, p.a.) for 2 min each. After rinsing in water for another 2 min, the colloidal probes were put on a clean glass slide and dried in an oven (Heraeus VTR5022, Gemini BV Labor) at 80°C.

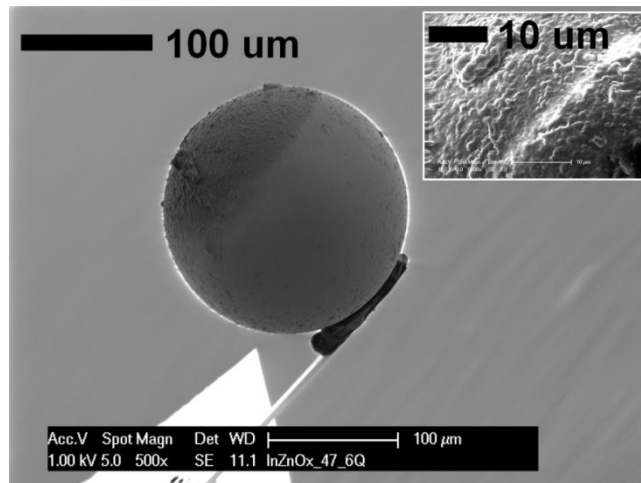


Figure 3-2 SEM image of a glass particle with radius  $\sim 86 \mu\text{m}$  glued onto a cantilever. The picture in the inset was taken on the surface of the particle.

In order to increase the wettability of particles, the cleaned colloidal probes were treated in oxygen plasma for 5 min (Femto, Diener Electronic GmbH, Germany).

---

In a second step, the very same hydrophilic particles were hydrophobized after the measurements. The colloidal probes were treated with oxygen plasma for another 5 min and then silanized by 1H,1H,2H,2H-Perfluorodecyltriethoxysilane (Sigma-Aldrich) in a desiccator at 100°C overnight. For flat clean glass substrates which can be fully wetted by water (contact angle close to zero), the contact angle with a water drop was increased to 107° after silanization. A similar modification was expected as well for the particles.

---

### 3.2.2 Spring constant of cantilevers

---

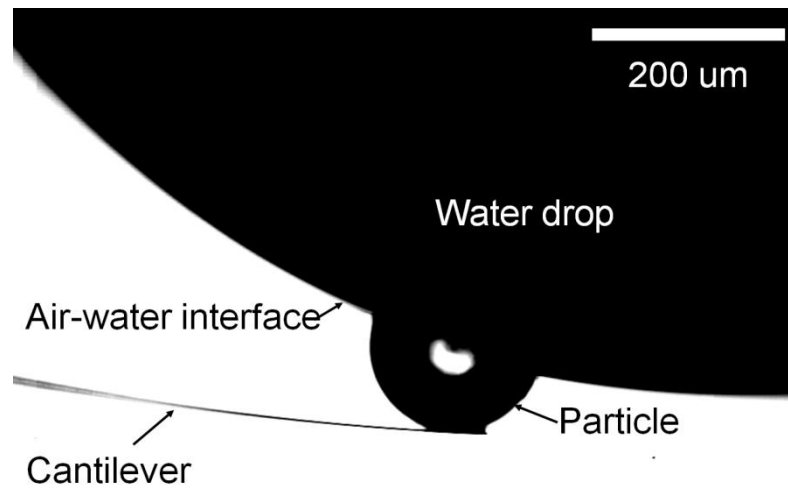


Figure 3-3 An inelastic bending of a soft cantilever with  $k \approx 0.004$  N/m. The particle radius is  $\sim 86\mu\text{m}$ .

To sense the movement of particles induced by capillary forces, cantilevers with spring constants in a certain range should be selected. If the spring constant of the cantilever is too small, the deflection of the cantilever will not be elastic, i.e. not anymore an ideal spring, as shown in Fig. 3-3. As a result, the capillary force can not be correctly detected by the bending of cantilever. The capillary force applied on the particles at the liquid-air interface scales as  $\gamma R$ , where  $\gamma$  is the surface tension of the liquid (water in our case). In the present measurements, the deflection of the cantilevers never exceeded 4% of its length, so that I could consider the cantilever as an ideal spring and use Hooke's law for calculating the force by  $F = kD$ .  $k$  is the cantilever spring constant and  $D$  is the cantilever deflection. The longest cantilevers

were 250  $\mu\text{m}$  long and the maximum deflection  $D_{Max}$  never exceeded 10  $\mu\text{m}$ . Thus, the smallest spring constants to be used are  $k_{Min} \sim \gamma R / D_{Max}$ , i.e., 0.16–0.63 N/m. On the other hand, the spring constant of the cantilever should not be too large, so that the deflection can still be measured. For the inverted particle interaction apparatus used here, the smallest deflection  $D_{Min}$  that can be detected was around 10 nm. Therefore, the largest spring constants could be used are  $k_{Max} \sim \frac{\gamma R}{D_{Min}} = 160 - 630$  N/m. In the experiments, I used cantilevers with spring constants  $k$  between 0.55 N/m (250  $\mu\text{m}$  length, 35  $\mu\text{m}$  width, and 2  $\mu\text{m}$  thickness, NSC12/tipless/noAL, MikroMasch, Tallinn, Estonia) and 3.1 N/m (221  $\mu\text{m}$  length, 29  $\mu\text{m}$  width, and 3  $\mu\text{m}$  thickness, TL-FM, Nanosensors, Neuchatel, Switzerland). The spring constants were selected also depending on the particles radius.

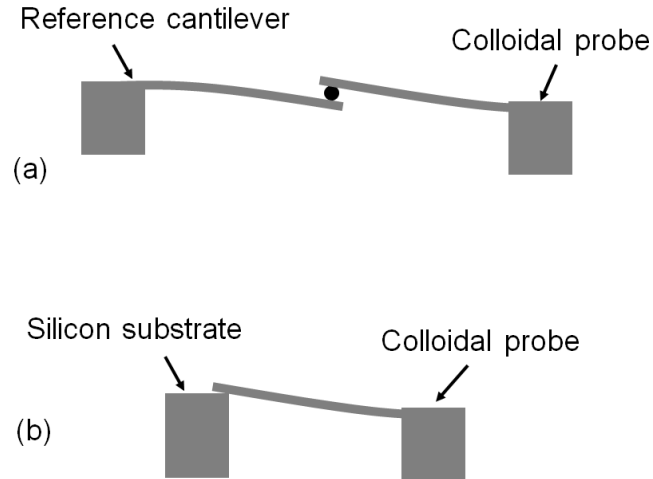


Figure 3-4 Schematic of the measurement of spring constant of colloidal probe. (a) The colloidal probe is pushed against the reference cantilever. (b) The colloidal probe is pushed against a rigid substrate.

The spring constants of the tipless cantilevers were measured with Dr. Lars-Oliver Heim by the thermal noise method [119] using a commercial Atomic Force Microscope (AFM, MFP-3D, Asylum Research, Santa Barbara, CA). When a particle was attached to the end of a cantilever, the spring constant of the colloidal probe was measured with a reference cantilever of known spring constant  $k_{ref}$ . As show in Fig. 3-4, the reference cantilever was fixed to the substrate, and the colloid probe was pushed against the tip of it. The sensitivity  $C_{ref}$  in this experiment was obtained from

the slope of the signal in the contact region. Repeating this experiment using a rigid silicon substrate instead of the reference cantilever leads to a different sensitivity  $C_R$ . Since the forces acting on the cantilevers during contact are equal, the spring constant of colloidal probe can be related to spring constant of the reference cantilever with [120, 121]

$$k = \frac{C_{ref} - C_R}{C_R} k_{ref} \quad (3.1)$$

### 3.2.3 Experimental setup

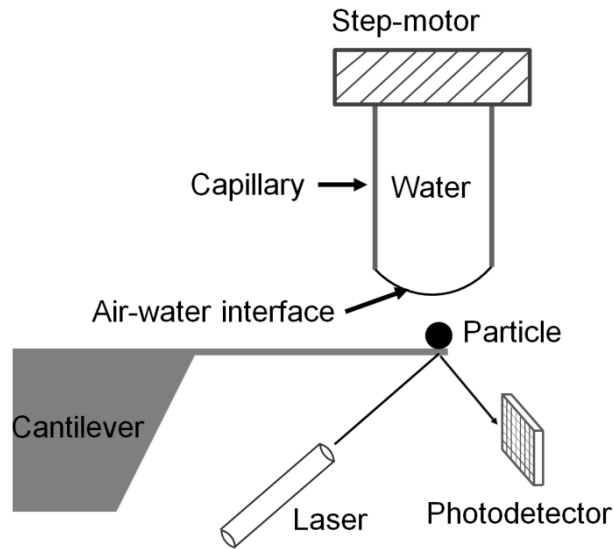


Figure 3-5 Schematic of the reversed particle interaction apparatus.

A homemade, inverted particle interaction apparatus was used to measure the dynamic wetting of single particles at the water-air interface (Figure 3-5). Millimeter sized water droplets were generated by a capillary tube, which was put above the cantilever. The capillary tube was attached to a step-motor with micrometer accuracy through which I could approach the water meniscus to the particle quasi-statically. A laser beam was pointed at the free end of the cantilever and the reflection of the beam was detected by a photodetector. By monitoring the position of the reflected laser spot, the deflection of the cantilever was detected with a sampling rate of at least 100 kHz corresponding to a time resolution of 10  $\mu$ s. To prevent influence of external



---

light, the setup was installed in a light-tight black box. More information about the setup can be found elsewhere [122, 123].

Before the measurements, the colloidal probe was calibrated with a hard silicon surface. Then, the dynamic wetting process of single particles with different sizes was detected. For each particle, at least 10 single measurements were done. The dynamic wetting process was also recorded with a high-speed camera at 10,000 fps, which offered a direct visualization.

---

### 3.3 Experimental results and discussion

---

#### 3.3.1 The dynamic wetting/snap-in process

---

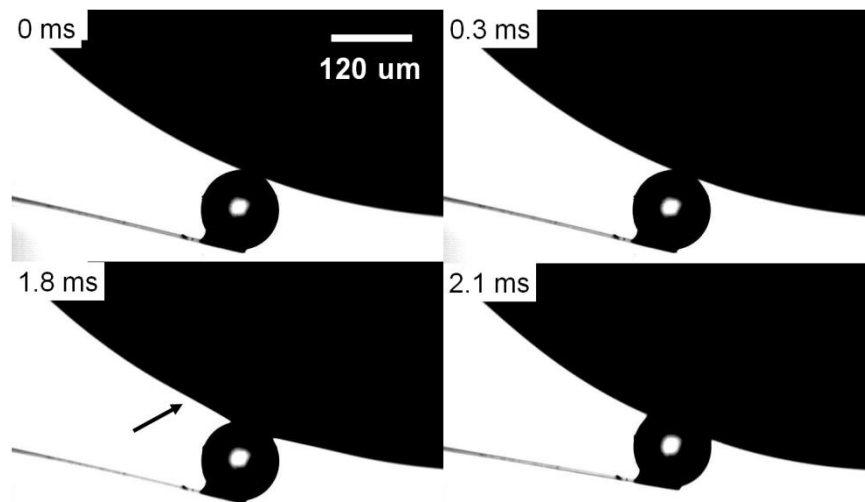


Figure 3-6 Snap-in process of a hydrophilic glass particle with radius of  $\sim 60 \mu\text{m}$  at the water-air interface.

Figure 3-6 shows the optical images of the wetting process of a single hydrophilic glass particle with a radius of  $\sim 60 \mu\text{m}$ . There were two wetting stages. First, once the particle touched the water-air interface, it was driven into the liquid very quickly. At the same time, a capillary wave was generated and propagated along the meniscus, as indicated by an arrow in Fig. 3-6. After  $\sim 2 \text{ ms}$ , wetting entered into a second stage and the water wetted the particle very slowly. It was impossible to analyze details of the wetting process from these images due to two reasons. On the one hand, the time resolution ( $\sim 0.1 \text{ ms}$ ) of the recorded movie did not allow to

---

capturing the very early wetting stage ( $<0.1$  ms). On the other hand, the space resolution of the image was poor ( $\sim 1 \mu\text{m}/\text{pixel}$ ) compared to the maximum cantilever deflection ( $\sim 2 \mu\text{m}$ ).

The early dynamic wetting/snap-in process can be precisely detected by I-PIA. Figure 3-7 shows the deflection of the cantilever with a hydrophilic (black symbols) and a hydrophobic (red symbols) particle measured with I-PIA. I monitored the cantilever bending over a time of  $\sim 6$  s. There are two time scales of wetting: a fast and a slow one (Fig. 3-7a). Similar results were also observed by Kaz *et al.* using a holographic microscope [103]. They analyzed their data with MKT model for the slow stage of wetting experiments for times  $t > 10$  ms and concluded that the slow wetting stage can last up to months. In my experiments, I did not observe equilibration after 6 s, which confirmed their results somehow.

Here, my interests were in the very early stage of wetting. Figure 3-7b shows a zoom-in look at the deflection data for times  $t < 100$  ms. It seems that the particles were driven into the liquid in less than 5 ms and after that the cantilever started to oscillate with a frequency of some hundreds of Hz ( $\sim 150$  Hz for the hydrophilic particle and  $\sim 230$  Hz for the hydrophobic particle). These oscillations were due to the excitation of capillary waves at the drop surface upon contact with the particles. For a drop with a volume of  $V$ , the resonance frequency of capillary wave on the surface scales as [124]

$$f \sim \sqrt{\frac{\gamma}{\rho V}} \quad (3.2)$$

Taking the radius of the capillary of  $\sim 1$  mm for estimation, the frequency is  $\sim 132$  Hz, which is similar to the ones observed in Figure 3-7b. A detailed study of the oscillation of sessile drops by AFM was carried out recently by McGuiggan *et al.* [124].

If further zoom-in the cantilever deflection curves for time  $t < 3$  ms, the very early dynamic wetting process can be observed. As shown in Fig. 3.7c, the dynamic wetting or snap-in process lasted only  $\sim 0.1$  ms and the particle plunged into the liquid with a speed of  $\sim 0.01$  m/s. After that, some other damped oscillations of the cantilever with a frequency of some kHz were found, arising from the snap-in process.

These oscillations were independent of the drop size and particle wettability, and corresponded to the damped resonance frequency of the cantilever.

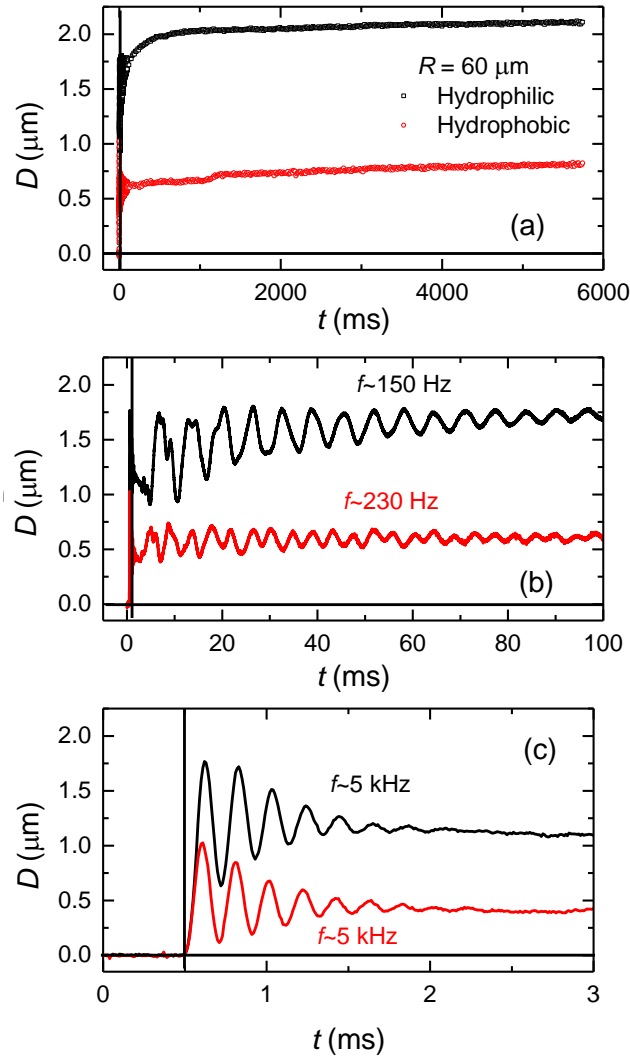


Figure 3-7 Cantilever deflection versus time during wetting for a hydrophilic (black symbols) and a hydrophobic (red symbols) particle. (a) Particle wetting process from  $t = 0$  to  $6$  s, showing a fast and a slow process; (b) Zoom-in from  $t = 0$  to  $100$  ms, showing the start of the slow wetting process for  $t > 1$  ms and the damped oscillations of the drop interface with a frequency  $f_{Drop} \approx 200$  kHz; (c) Zoom-in from  $t = 0$  to  $3$  ms, showing the fast wetting process for  $t < 1$  ms and the cantilever oscillations with a frequency  $f_{CL} \approx 5$  kHz. The particle radius is  $\sim 60 \mu\text{m}$  and the spring constant of the cantilever is  $\sim 3.0$  N/m.

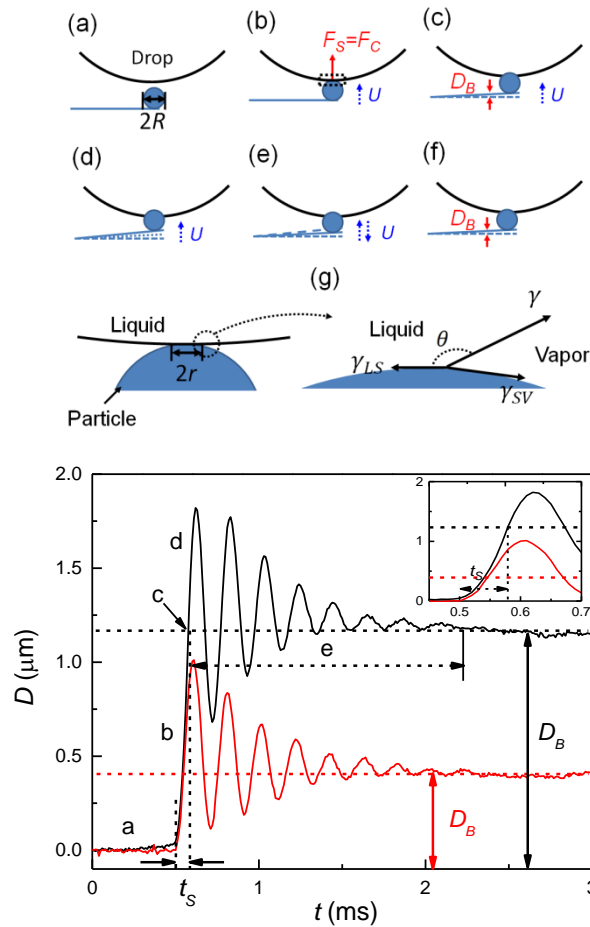


Figure 3-8 Top: (a)-(f) Schematic of the snap-in process of a particle by the water-air interface.  $U$  indicates the velocity of the particle. (g) Zoom in the initial contact area between the particle and water drop in (b). Bottom: Cantilever deflection versus time during the fast snap-in processes for a hydrophilic (black line) and a hydrophobic (red line) particle. The particle radius is  $\sim 60 \mu\text{m}$  and the cantilever spring constant is  $\sim 3.0 \text{ N/m}$ . The inset shows the snap-in time  $t_s$  in more detail.

Now, I would like to connect the cantilever deflection to the snap-in of a particle at the water-air interface. Figure 3-8 sketches the snap-in process (top) and corresponding cantilever deflection versus time (bottom) for the same hydrophilic and hydrophobic particles in Fig. 3-7. When the particle is far away from the interface, there is no force applied on the particle. The deflection of the cantilever is zero (Fig. 3-8a). Once the particle is brought into contact with the water-air interface, the initial contact angle between the liquid and particle is  $\theta \sim 180^\circ$  and the capillary force normal to the particle is still zero (Fig. 3-8g). However, the surface tension of the water,  $\gamma$ ,

---

interfacial tension between solid (particle) and vapor  $\gamma_{SV}$ , and interfacial tension between liquid (water) and solid (particle)  $\gamma_{LS}$  are not balanced. As a result, there is a net interfacial force parallel to the particle surface and it causes the liquid to wet the surface, similar to what happens on bulk flat surfaces [35, 36, 55]. During wetting, the contact angle  $\theta$  decreases and the normal component of the surface tension,  $\gamma \sin \theta$ , increases, and this leads to another net force,  $F_C = 2\pi r \gamma \sin \theta$  that drives the particle into the interface (Fig. 3-7 & 3-8b).  $r$  is the contact radius between the liquid and particle, as shown in Fig. 3.8g. At the same time, the cantilever is bent by this force (Fig. 3-8 right). After a time, the cantilever reaches a position with a deflection of  $D_B$ , where the capillary force is compensated by the elastic restoring force of the cantilever (Fig. 3-8c). However, the particle continues to move in the water drop due to its inertia (Fig. 3-8d-e & Fig. 3-8 right). Eventually, the cantilever reaches an equilibrium state with a cantilever deflection of  $D_B$  after 1-2 ms of damped oscillations (Fig. 3-8f & Fig. 3-8 right). The deflection of the hydrophilic colloidal probe is larger than that of hydrophobic colloidal probe. A similar trend is also found for  $D_B$ . This is because the capillary force applied on the hydrophilic particle is larger than that on the hydrophobic particle, which will be further discussed in later sections.

---

### 3.3.2 Snap-in time

---

From Fig. 3.7 and Fig. 3.8, it was found that the particle was driven into the water by the capillary force and the cantilever rested at a deflection  $D_B$  for a few milliseconds until the capillary wave starts to propagate along the water-air interface. Since the next wetting stage is much slower (up to weeks or months), the state with deflection of  $D_B$  could be treated as a quasi-equilibrium state. Thus, the time needed to reach the deflection  $D_B$  during the snap-in process was defined as the snap-in time,  $t_s$  (inset of Fig. 3.8 bottom). In the next step, the characteristic time scale of  $t_s$  was estimated with a scaling analysis.

During the snap-in process, the momentum change of the particle,  $\Delta M_p$ , which resists wetting is

$$\Delta M_p = m_p \frac{du}{dt} \quad (3.3)$$

Here  $m_p$  is the mass of the particle and  $u$  is the snap-in velocity. The capillary force due to the direct action of surface tension is

$$F_c = 2\pi R\gamma \sin \beta(t) \sin(\theta(t) + \beta(t)) \quad (3.4)$$

Where  $\beta(t)$  is the angle which describes the position of the three-phase contact line as shown in Fig. 3-9. Balancing these two terms, one can obtain the equation of motion

$$m_p \frac{dv}{dt} = 2\pi R\gamma \sin \beta(t) \sin(\theta(t) + \beta(t)) \quad (3.5)$$

Equation (3.5) cannot be solved as  $\theta(t)$  and  $\beta(t)$  are not known. Nevertheless, I carried out a scaling analysis. The momentum term can be scaled as  $\rho_p R^3 L^* / \tau_i^2$  and the capillary force is proportional to  $\gamma L^*$ . Where  $\rho_p$  is the density of particle,  $L^*$  is a characteristic length comparable to the particle radius and  $\tau_i$  is the characteristic inertial time. Balance these two terms yields the time scale of the snap-in process,

$$\tau_i \sim \sqrt{\frac{\rho_p R^3}{\gamma}} \quad (3.6)$$

The characteristic snap-in time obtained here has the similar format as the one for inertial wetting of liquids on bulk surfaces [35, 36, 55]. Equation (3.6) also predicts that  $\tau_i$  is independent on the wettability of the particles.

Figure 3-9 shows the snap-in time as a function of the characteristic time for particles with  $R$  between 22 and 86  $\mu\text{m}$ . The snap-in has a typical value of 0.1 ms, which is consistent with the calculated values from literatures for the interaction of particles and bubbles [125] or for capillary wetting [126].  $t_s$  is slightly larger than  $\tau_i$ . Fitting the data with a linear regression leads to a factor of  $1.2 \pm 0.13$ . One reason for this result could be that the inertial effects were underestimated as the inertia of the cantilever was not considered. The mass of the cantilever scales as  $\rho_c w d L$  and the momentum of the particle plus cantilever is proportional to  $(\rho_p R^3 + \rho_c w d L) L^* / \tau_i'^2$ .  $\rho_c$  is the density of the cantilever, and  $w$ ,  $d$  and  $L$  are the width, thickness and length of the cantilever. Rebalancing momentum term and capillary force results in a new characteristic inertial time scale  $\tau_i'$

$$\tau_i' \sim \sqrt{\frac{\rho_p R^3 + \rho_c w d L}{\gamma}} \quad (3.7)$$

The new characteristic inertial time is larger than the old one, i.e.  $\tau'_i > \tau_i$ . Taking some characteristic values of particle and cantilever dimensions ( $R \sim 50 \mu\text{m}$ ,  $w \sim 30 \mu\text{m}$ ,  $d \sim 2.5 \mu\text{m}$ ,  $L \sim 250 \mu\text{m}$  and  $\rho_c \sim 2500 \text{ kg/m}^3$ ), one obtains  $\tau'_i \sim 1.15\tau_i$ , which is close to the slope of the linear fit of experimental data.

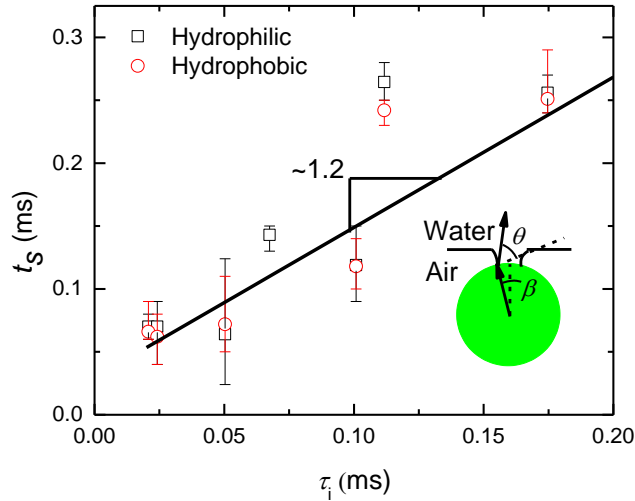


Figure 3-9 The snap-in time  $t_s$  of hydrophilic/hydrophobic particles with various sizes is plotted as a function of the characteristic inertial time  $\tau_i$ . The solid line is the best fitting line with a slope of  $1.2 \pm 0.13$ . The inset shows the relevant parameters.

Figure 3-9 also indicates that the snap-in time is independent on the wettability of particles. This is again consistent with the outcome of the scaling analysis. The early snap-in process is only dominated by the capillary force and by inertia. In a recent paper about dynamic wetting of low viscous liquids, Winkels *et al.* showed that the very early wetting dynamics is independent on wettability [52]. Here, a similar phenomenon was observed in the early dynamic wetting of single particles.

### 3.3.3 Snap-in force

The snap-in and oscillation process lasted only  $\sim 2$  ms. After that, the particle was trapped in a well defined position at the water-air interface, corresponding to a cantilever deflection of  $D_B$ . As shown in Fig. 3-7, for  $t > 2$  ms, the wetting of particle

proceeded with an extremely slow velocity ( $\sim 10^{-7}$  m/s) and the deflection of the cantilever increased accordingly slowly. In other words, the slow wetting stage has a time constant (months were reported in the literature) much larger than the time scale of the snap-in process ( $\sim 0.1$  ms). Therefore, I treated  $D_B$  as a “quasi-equilibrium” position with respect to the time scale considered. In section 3.3.1, it was found that  $D_B$  was dependent on the wettability of the particles, which indicates that the capillary driving force is different for different wettable surfaces. As a result, the elastic bending of the cantilever at the deflection  $D_B$  was further defined as the snap-in force,  $F_S$ . With Hook’s law, the snap-in force can be calculated with  $F_S = kD_B$ .

Figure 3-10 shows the snap-in force of hydrophilic and hydrophobic particles with different radii  $R$ .  $F_S$  was larger for hydrophilic than for hydrophobic particles if the size of the particles is the same. Moreover, the snap-in force increased with particle size. The source of snap-in force is the capillary force. However, it is impossible to directly relate the snap-in force with the capillary force since  $r$ ,  $\theta(t)$  and  $\beta(t)$  could be estimated only within a certain approximation, and moreover they change with time. Nevertheless, an order of magnitude estimation can be carried out. The capillary force  $F_C = 2\pi R\gamma \sin \beta \sin(\theta + \beta)$  has a maximum at  $\frac{dF_C}{d\beta} = 0$  [106]

$$\frac{dF_C}{d\beta} = 2\pi R\gamma \sin(\theta + 2\beta) = 0 \quad (3.8)$$

From equation (3.8), one obtains  $\theta + 2\beta = 180^\circ$ . Substituting  $\beta = 90^\circ - \frac{\theta}{2}$  into equation (3.4), one finds the maximum capillary force with a value of

$$F_{CMax} \sim \propto \gamma R \cos^2\left(\frac{\theta}{2}\right) \quad (3.9)$$

For estimation, I inserted the equilibrium contact angle of  $\sim 0^\circ$  and  $\sim 110^\circ$  measured on the flat hydrophilic and hydrophobic surfaces into equation (3.9). As shown in Figure 3-10,  $F_{CMax}$  and  $F_S$  agreed on the order of magnitude and showed a similar dependence on the particle radius and wettability. In fact, to the nearly doubled magnitude of  $F_S$  between a hydrophilic and a hydrophobic particle corresponded a nearly doubled magnitude of the calculated  $F_C$ . Similar relations are also known from literature [125].



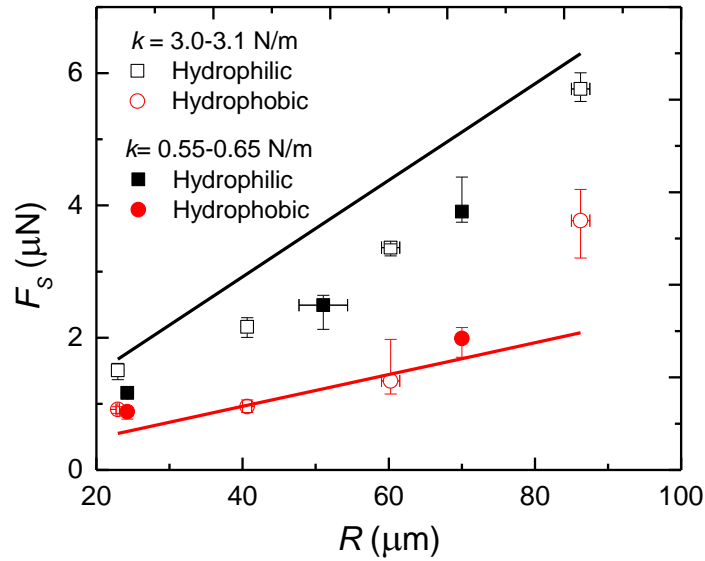


Figure 3-10 Snap-in force of hydrophilic/hydrophobic particles measured with two types of cantilevers with different stiffness as a function of particle radius  $R$ . The black and red solid lines represent the scaling capillary force  $\gamma R \cos^2(\frac{\theta}{2})$  for hydrophilic and hydrophobic particles, respectively.

### 3.4 Summary

Using the advantage of high time and space resolution of the inverted particle interaction apparatus, I studied the dynamic wetting of single colloidal particles at a water drop surface. The dynamic wetting proceeded in two stages: a fast snap-in stage followed by a slow wetting stage. In the snap-in stage, the dynamics was dominated by inertia. The snap-in time ( $\sim 0.1$  ms) was dependent on capillarity and inertia, but was independent on surface wettability. The snap-in force, and thus the adhesion, had a value of few micronewtons and was larger for hydrophilic surfaces. After the snap-in process, the particle was not yet in equilibrium. Wetting entered an extremely slow stage which might last up to weeks or months [103].



---

**Part II Effects of Surface Wettability, Liquid Viscosity and External  
Electric Field on Dynamic Wetting**

---



---

---

## 4 Early Dynamic Electrowetting of Aqueous Electrolyte Drops<sup>5</sup>

---

In the previous two chapters, I introduced my dynamic wetting studies with simple liquids on two types of complex surfaces: soft viscoelastic surfaces and small particles. Since this chapter, I will introduce dynamic wetting of simple and viscous liquids on simple, rigid surfaces. Specifically, the influence of external applied electric field, liquid viscosity and surface wettability on wetting dynamics will be discussed. This chapter presents a systematic study of early dynamic wetting of aqueous electrolyte (simple liquid) drops driven by an electric potential. It was found that spreading dynamics not only depended on surface wettability and applied potential, but also on the electrolyte concentration. Molecular dynamics (MD) simulations done in the group of Computational Physical Chemistry (CSI, Technische Universität Darmstadt) supported these observations. Based on MD simulation results on the ion distribution in spreading nanodrops under an applied potential, a simple model was proposed in collaboration with Dr. Günter K. Auernhammer (Max-Planck Institute for Polymer Research, Mainz) to explain the relation between applied potential, surface wettability, electrolyte concentration, and early drop spreading dynamics.

---

### 4.1 Motivation

---

As stated earlier, the fast development of high-speed video cameras has prompted a strong interest in investigating rapid dynamic wetting processes in recent years [18, 35, 36, 54, 55, 58-61, 79]. The main finding was that wetting may proceed in three stages, and that the dynamics follows a power law, as reviewed in the first chapter of this thesis.

Most of the spreading studies in the literature were carried out on grounded surfaces. In a most recent paper, Courbin *et al.* reported that the early spreading of a water drop on a completely wetting surface followed a power law with  $\alpha = 2/3$ , if an electric potential was applied between the drop and the surface [79]. The exponent was much larger than the maximum value,  $\alpha = 0.5$ , which was found on grounded

---

<sup>5</sup> This chapter is based on “L. Q. Chen, C. L. Li, N. F. A. van der Vegt, G. K. Auernhammer, E. Bonaccorso, *Initial electrospreeding of aqueous electrolyte drops*, Phys. Rev. Lett. **110**, 026103 2013”.

---

solid surfaces [54, 55]. Thus, a fundamental question naturally came up: How and to which extent could an external potential influence early drop spreading or wetting? In nature and in many technical applications, an electric potential can be spontaneously induced by charging surfaces via friction, i.e. by the triboelectric effect [127]. For example, in the printing process, the friction between the paper and machine could charge the paper and cause a potential difference between ink and paper. Practically, applying an electric potential to assist ink transfer has been used in gravure printing for more than half a century [128, 129]. In recent years, electrostatic modulation of the interfacial tension between a solid electrode and conducting liquids, which is known as electrowetting [130-132], was robustly applied in manipulating tiny liquid drops in microfluidics [133, 134]. Thus, understanding the influence of electric potential on dynamic wetting of aqueous electrolyte drops is crucial for both fundamental understanding and for industrial applications.

---

## 4.2 Experiments

---

### 4.2.1 Surfaces

---

To demonstrate that everyday surfaces can be easily charged and the induced electric potential influences the spreading dynamics, I used microscopy glass slides. Glass is an insulator. The slides were cleaned in acetone and in ethanol in an ultrasonic bath for 5 min each. After rinsing in Milli-Q water for 5 min, they were dried with nitrogen and further treated with oxygen plasma for 2 min. The equilibrium contact angle of water on the surface was  $\theta_{eq} \approx 0^\circ$ .

To systematically study the effects of electric potential on dynamic wetting, highly doped, conductive silicon wafers (Boron doped, (100) orientation, resistivity 1-20  $\Omega$ -cm, Crys Tec GmbH, Germany) were used. These silicon surfaces are covered by a native oxide layer with a thickness  $d_{ox} \approx 5$  nm. With the same cleaning treatment described above, completely wetting silicon surfaces were obtained. In order to vary the wettability, plasma treated clean silicon wafers were silanized with 3-Aminopropyltriethoxysilane, Hexamethyldisilazane, and 1H,1H,2H,2H-Perfluorodecyltriethoxysilane (Sigma-Aldrich) following a standard silanization procedure [1]. The thickness of the silane coating is  $d_{sil} \approx 2$  nm. The equilibrium ,

advancing, and receding contact angles of these surfaces with water drops were measured with a contact angle meter (Krüss, DSA 100, Germany), as listed in Table 4-1.

Table 4-1 Equilibrium, advancing, and receding contact angles of water on the four silicon substrates modified by different silanes.

Substrate	$\theta_{eq}$ (°)	$\theta_{Ad}$ (°)	$\theta_{Re}$ (°)
Silicon dioxide	~0	—	—
3-Aminopropyltriethoxysilane	63±4	88±2	46±3
Hexamethyldisilazane	90±2	106±2	83±3
1H,1H,2H,2H-Perfluorodecyltriethoxysilane	107±3	116±3	100±2

#### 4.2.2 Liquids

In the experiments, I studied early dynamic wetting of five aqueous NaF solutions - prepared with MilliQ water - with concentrations of  $c \approx 0.001, 0.01, 0.04,$  and  $0.091$  mol/kg, respectively. The surface tension of these liquids varies by less than  $1$  mN/m ( $\gamma \approx 72$  mN/m) [135] and the viscosity of all solutions is similar ( $\mu \approx 0.89$  mPa · s). The solutions have similar permittivity, but quite different conductivity (Table 4-2).

Table 4-2 Properties of the five electrolyte solutions. The electrical permittivity as a function of electrolyte concentration was calculated with an empirical expression from Ref.137.

NaF concentration $c$ (mol/kg)	Conductivity (mS/cm, at 25°C) [136]	Permittivity (F/m) [137]
0	$5.5 \times 10^{-5}$	$7.08 \times 10^{-10}$
0.001	$9.7 \times 10^{-2}$	$6.99 \times 10^{-10}$
0.01	0.92	$6.98 \times 10^{-10}$
0.04	5.13	$6.93 \times 10^{-10}$
0.091	7.67	$6.82 \times 10^{-10}$

---

### 4.2.3 Experimental setup

---

The experimental setup was the same as the one shown in section 2.2.3. The needle (inner radius  $r_n = 400 \mu m$ ) through which drops were generated was kept at a distance  $d = 2 \text{ mm}$  from the surface. A direct current (DC) voltage was applied between the needle and the surface (Fig. 4-1), and the voltage  $\phi$  varied from 0 to 1,000 V.

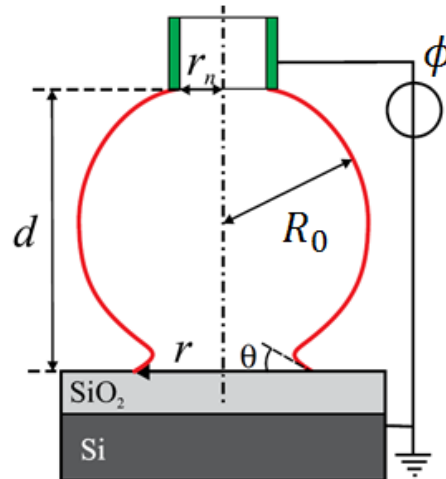


Figure 4-1 Sketch of the setup: a drop of initial radius  $R_0$  hangs from a needle with inner radius  $r_n = 400 \mu m$ . The needle is at a distance  $d = 2 \text{ mm}$  from the surface. Between the needle and the surface a potential  $\phi$  is applied.

---

### 4.2.4 Drop spreading experiments and data analysis

---

A high-speed video camera (FASTCAM SA-1, Photron Inc., USA) was used to capture the dynamic wetting process. The drop spreading process was first recorded with a frame rate of 54,000 fps. To have a higher time resolution, I focused on the contact area and recorded the very early process with a recording speed up to 200,000 fps (the limit frequency of the camera). The resolution of the recorded image was  $10 \mu m$  per pixel. Using the self-programmed MATLAB<sup>®</sup> (MathWorks Inc., USA) algorithm, the growth of contact radius was extracted from the images. Since the early dynamic wetting was dominated by inertia, the experimental data was fitted with a power law using the least square method (LSM).



---

---

## 4.3 Experimental results

---

### 4.3.1 Early spreading on randomly charged surface

---

Here, I firstly show that natural surfaces can be easily charged and that the charges on the surface influence wetting. A glass slide was cleaned as described before and performed the wetting experiments with drops of water immediately after.

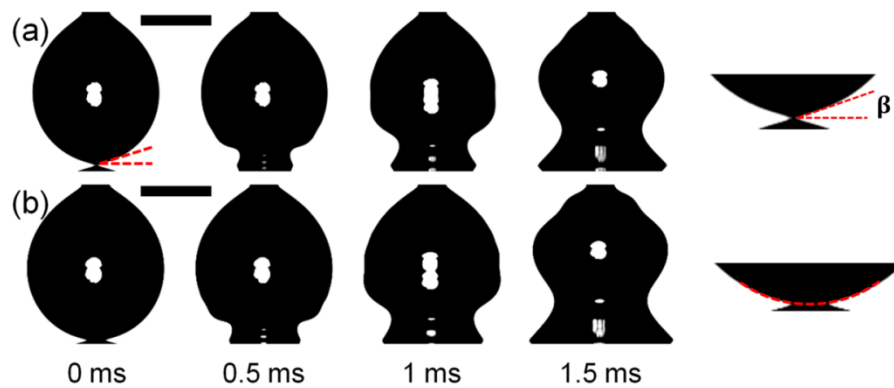


Figure 4-2 High-speed video images of water drops spreading on completely wetting (a) charged glass and (b) uncharged glass. The last image in Figure. 4-2 a&b is the zoom-in view of the initial contact area.  $\beta$  is the angle formed between the conical lower end of the drop and the glass surface. The scale bar is 1 mm.

At a distance larger than  $100 \mu\text{m}$  from the glass surface, the water droplet had a spherical shape. However, upon further approaching the surface the lower cap of the drop deformed into a cone shape with an angle  $\beta \sim 15^\circ$  (Fig. 4-2a). This happened at a distances of few tens micrometers above the surface. There are two possible explanations for the formation of the cone. First, the surface could be charged during the cleaning process. That caused a potential difference between the drop and surface, which can lead to electrocapillary instabilities [138, 139]. I repeated the droplet generation experiments with connecting the needle to ground. The cone was formed again when the drop approached the surface. However, the cone was not observed

after the surface was uncharged<sup>6</sup>. This indicates that the surface was charged during the cleaning process. Another possibility is that the drop-surface attraction by interfacial forces induced the deformation when they became very close. The interaction between a droplet and flat surface scales as  $F \sim -\frac{A_H R_0}{D^2}$  [127], where  $A_H$  is the Hamaker constant ( $A_H \sim 6.34 \times 10^{-20}$  J for the interaction between water and glass [140]) and  $D$  is the separation between droplet and surface. However, this force is several orders of magnitude less than the capillary force  $\gamma R_0$  at separations of several micrometers. Thus, surface forces cannot deform the droplet to such an extent.

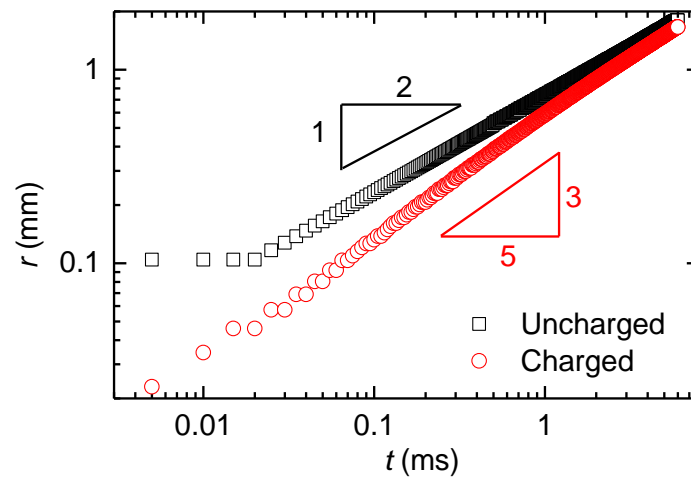


Figure 4-3 Log-log plots of water drop spreading radius  $r$  vs. spreading time  $t$  of Figs. 4-2a and 4-2b.

When the tip of the cone shaped drop touched the surface, it instantly spread out, as illustrated in Fig. 4-2a. The spreading radius  $r$  as a function of spreading time  $t$  in log-log plot is presented in Fig. 4-3. The spreading followed a power law with the exponent being  $\sim 0.6$ . On randomly charged insulating glass surfaces, the measured exponents were between  $1/2$  and  $2/3$ . In contrast, water droplets did not spread out immediately after contacting uncharged surfaces. After some tens of milliseconds only they began to wet the surface. The initial contact radius was larger on the uncharged than on the charged surfaces (Fig. 4-2a & b). The delayed spreading may be due to a

<sup>6</sup> The surface was put in a sealed petridish for at least 2 hours during which a natural discharging process was expected. This was confirmed by droplet generation experiments.

thin air film entrapped between drop and surface, which was beyond the present work. The log-log plot in Fig.4-3b indicates that the spreading on the uncharged surface follows a power law with  $\alpha \sim 0.5$ , which is consistent with the value on a complete wetting surface as predicted theoretically [54] and demonstrated experimentally [54, 55]. In summary, it was found that surface charges make wetting faster, even if the charging of the surface was not controlled.

### 4.3.2 Early spreading under electric potential

In the previous section, I showed that surface charges which could also be induced by an applied electric potential, enhanced the wetting. This finding raises a number of questions. How and to which extent does electric potential influence the wetting dynamics? Does the concentration of the salt in electrolyte solutions influence the spreading? How does the surface wettability play a role in the wetting process? In order to answer these questions, a systematic study of early drop spreading with various aqueous electrolyte solutions was carried out on four surfaces with different wettability and changing electric potential.

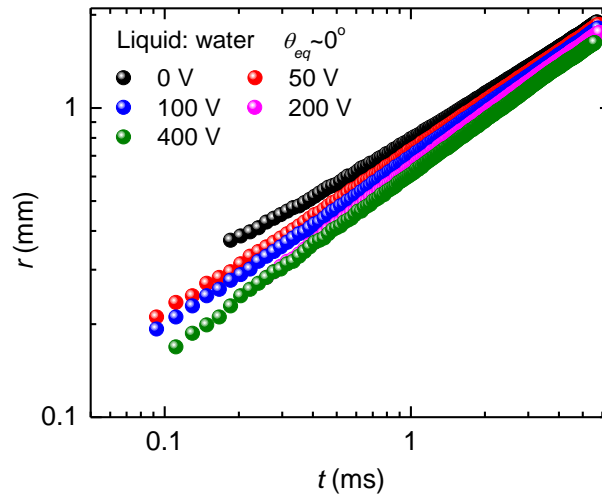


Figure 4-4 The spreading radius  $r$  of a pure water drop vs. time  $t$  (log-log scale) on a completely wetting surface for  $\phi = 0, 50, 100, 200, 400$  V.

Figure 4-4 shows the log-log plot of  $r$  versus  $t$  of a water drop spreading on completely wetting surfaces with  $\theta_{eq} \approx 0^\circ$  under  $\phi = 0, 50, 100, 200, 400$  V,

respectively.  $\beta$  increased with increasing voltage and the corresponding initial spreading radius decreased. However, the electrospreading exponent, which was called  $\alpha'$  to distinguish it from the spreading exponent  $\alpha$  (with  $\phi = 0$  V), increased with  $\phi$  irrespective of the wettability of surfaces. This agrees with the findings from electrowetting literature [130-132]. The spreading on relatively hydrophilic surfaces was always faster than on relatively hydrophobic surfaces. Moreover, it was also found that  $\alpha'$  increased with electrolyte concentration when the wettability of the surface and the applied voltage were kept the same.

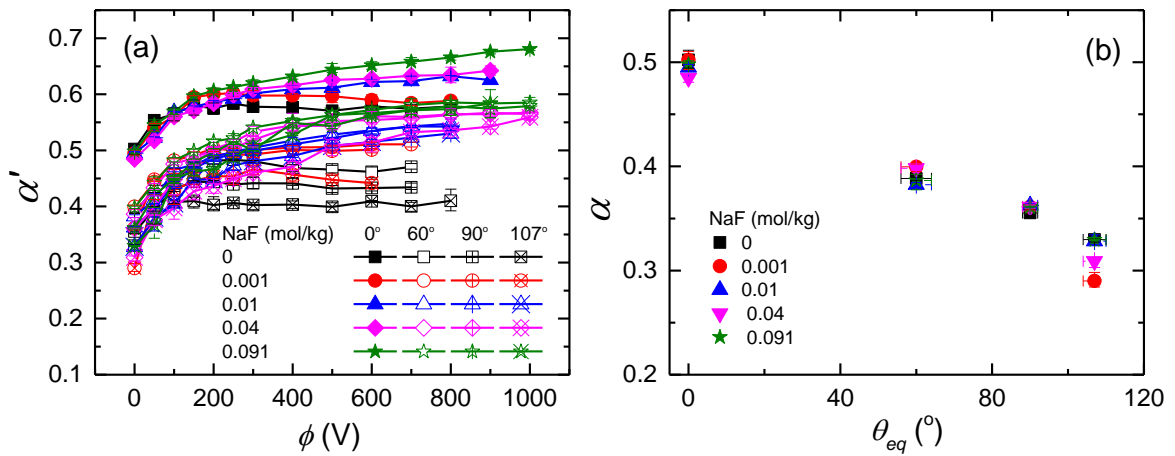


Figure 4-5 (a) Exponent  $\alpha'$  as function of the applied voltage  $\phi$  for four wettable surfaces and for five aqueous electrolyte concentrations. (b) Relationship between exponent  $\alpha$  and the wettability of the surfaces with  $\phi = 0$  V.

Figure 4-5a shows the electrospreading exponent  $\alpha'$  as a function of applied voltage, surface wettability and electrolyte concentration. When no potential was applied, the exponent  $\alpha$  was only dependent on surface wettability, i.e.  $\theta_{eq}$  (Fig. 4-5b). In the experiment,  $\alpha$  was larger for relatively hydrophilic than for relatively hydrophobic surfaces (Fig. 4-5b), which is consistent with results reported in literature [55]. Upon increasing  $\phi$ , the exponent increased. The increase was more pronounced for higher NaF concentrations. It was also found that the exponent was independent of the polarity of  $\phi$ . For pure water and for the lowest electrolyte concentration (0.001 mol/kg), the exponent increased until  $\phi \approx 200$  and 300 V, respectively. With further increases of  $\phi$ ,  $\alpha'$  remained constant or reached saturation (Fig. 4-5 and Fig. S1). However, for higher electrolyte concentrations, the exponent

increased with  $\phi$ , but did not reach saturation even at  $\phi \approx 1,000$  V. This electrowetting behaviour differs from other electrowetting experiments which showed to be unaffected by the electrolyte concentration. Electrowetting is said to work also for electrolyte-free water, given that the frequency of the applied potential is below some kHz [131]. In my experiments, the dynamic wetting of the drop depended on surface wettability, the magnitude of the applied potential, and the electrolyte concentration.

### 4.3.3 Drop recoiling

For water and water with NaF of 0.001-0.04 mol/kg, I observed that the drops recoiled after the first contact with the surface when the applied voltage was larger than a critical value  $\sim 800$  V (Fig. 4-6). This is because the local curvature in the liquid thread results in a high pressure which prevented the contact when the cone angle was larger than  $\sim 31^\circ$  [141]. Similar results were also observed for oppositely charged drops coming into contact [141, 142]. After  $\sim 0.18$  ms, the recoiled drop contacted the surface again and then spread out. However, the growth of spreading radius after the second contact did not follow a power law any more, as shown in Figure 4-7.

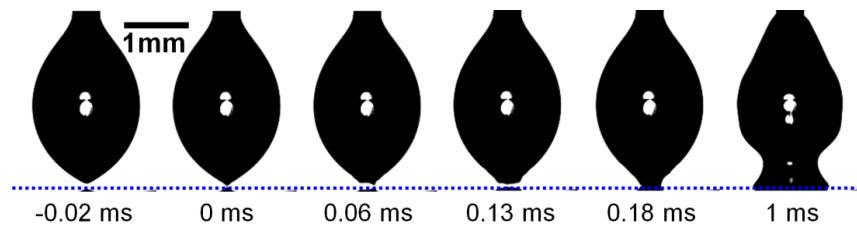


Figure 4-6 A water drop recoils after contact with the surface with  $\phi = 800$  V.

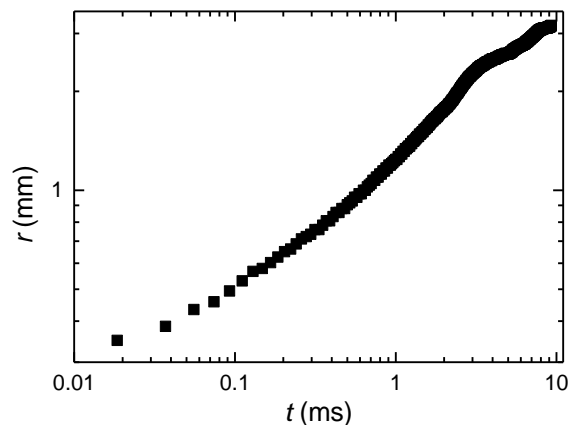


Figure 4-7 Log-log plot of spreading radius  $r$  vs.  $t$  for the wetting case in Figure 4-6.

---

## 4.4 MD Simulation from CPC

---

In the experiment, the five aqueous electrolyte solutions had similar surface tension, viscosity, only slightly different permittivity, but strongly different conductivity (see Table 4-2). Thus, one possibility is that the molecular processes at or near the solid-liquid interface affected early electrospreeding dynamics [143-145]. Indeed, few groups found that ionic processes influenced electrowetting in recent years [143]. Since the high speed imaging technique cannot capture these processes at the sub-micrometer or even lower scale, I asked support from the CPC group by Molecular Dynamics (MD) simulations. The MD simulations of dynamic wetting of aqueous electrolyte nanodrops were done by Dr. Chunli Li.

---

### 4.4.1 MD Simulation method

---

The simulations were carried out by using the package GROMACS [146]. The temperature was set to 300 K according to the experimental condition. A 4.5 nm-radius nanodrop containing more than  $10^4$  water molecules with 200 Na<sup>+</sup> and F<sup>-</sup> ion pairs was used (first snapshot of Fig. 4.8a & b). The composition of the nanodrop corresponded to a bulk electrolyte concentration of  $c \approx 0.5$  mol/kg. In order to have good statistics, the NaF concentration in simulation was slightly larger than the maximum concentration in the experiments. The silicon substrate contained 5 layers of silicon atoms with 36,000 atoms in total that were fixed during simulations and were modeled as Lennard-Jones (LJ) particles with  $\sigma_{Si-Si} = 0.34$  nm and  $\varepsilon_{Si-Si} = 2.45$  kJ/mol [147].  $\sigma_i$  is the LJ size parameter and  $\varepsilon_i$  is the LJ well depth. The extended simple point charge (SPC/E) model was used for water [148]. For Na<sup>+</sup> and F<sup>-</sup>, she used  $\sigma_{Na-Na} = 0.29$  nm,  $\varepsilon_{Na-Na} = 0.52$  kJ/mol,  $\sigma_{F-F} = 0.31$  nm, and  $\varepsilon_{F-F} = 0.31$  kJ/mol [149]. For calculating the LJ forces between unlike atoms, the Lorentz-Berthelot mixing rules were applied [150]. An external electric field of 0.1 V/nm was applied perpendicular to the surface. This value was in the range of previous MD simulations of spreading drops [145] and of electrowetting experiments.

---

#### 4.4.2 Spreading of electrolyte nanodrops

---

Figure 4-8 shows the snapshots of spreading process of electrolyte nanodrops without (Fig. 4-8a) and with (Fig. 4-8b) external electric field. Prior to touching the surface the nanodrop was spherical, as shown in the first snapshot in Fig. 4.8a & b. We did not observe the formation of a cone shape at the lower part of the drop under the electric field, as in the millimeter-sized drops in macroscopic experiments. One possible reason is that the deformation is hard to observe at the nano scale, since the thermal vibration of the nanodrop is very strong. As a result, the electrocapillary instability could be masked.

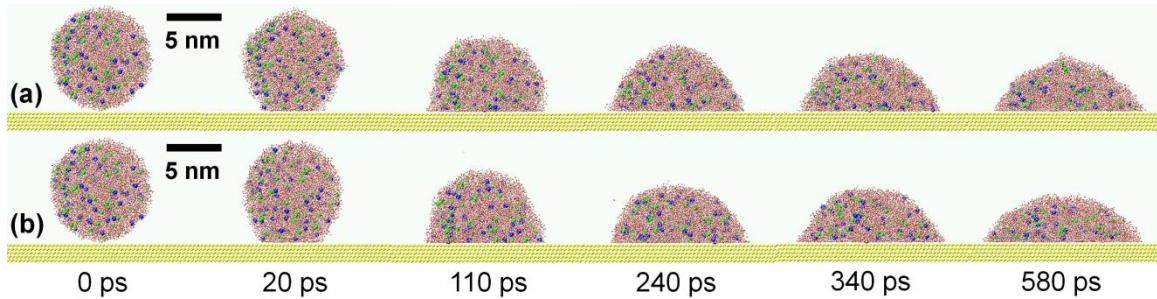


Figure 4-8 Snapshots of aqueous electrolyte nanodrops spreading on silicon surface without (a) and with (b) external electric field. Blue particles are Na<sup>+</sup> ions and green particles are F<sup>-</sup> ions.

Once the drop touched the surface, it spread spontaneously (Fig. 4-8). The spreading was fast at the beginning and became slower after  $\sim 200$  ps. The drops reached equilibrium ( $\theta_{eq}$  and  $r_{eq}$ ) after  $\sim 600$  ps.  $r_{eq}$  was larger with applied electric field ( $r_{eq} \approx 6.9$  nm) than without ( $r_{eq} \approx 6.3$  nm) it, which indicates the external electric field enhanced wetting.

The growth of the spreading radius with time is shown in Fig. 4-9. Spreading can be divided into three stages. In the first stage ( $t \lesssim 180$  ps), the spreading was extremely fast. The data of both drops without and with electric field could be fitted with a power law  $r \sim t^\alpha$ . The exponent  $\alpha$  was  $\sim 0.31 \pm 0.01$ , which is close to the exponent of inertial power law for comparably wetting surfaces [35, 55]. This indicates that the first wetting stage of nanodrops is also dominated by inertia, and the applied field has no influence on spreading until this point. Since a viscous stage is

known to follow an inertial wetting stage [35, 55], it was expected a similar phenomenon at the nanoscale as well. Indeed, in the second stage ( $180 \lesssim t \lesssim 600$  ps), the spreading radius grew with time according to  $r \sim t^{0.08 \pm 0.01}$  without electric field, which is consistent with viscous spreading dynamics [54, 58, 61]. With applied electric field, we also found a power law dynamics with  $r \sim t^{0.15 \pm 0.01}$ . The simulations thus revealed a larger spreading exponent during the second stage only, while in the experiments the spreading exponent was larger during the first stage. A possible explanation is that fast spreading at the nanoscale was too short to observe the influence of ion migration induced by the applied field. The average inertial spreading speed was  $\sim 10$  m/s in simulations and  $\sim 1$  m/s in experiments, which was closer to the viscous spreading speed of the nanodrops. In the third stage, the nanodrops were in equilibrium. A larger wetted area was found with applied electric field.

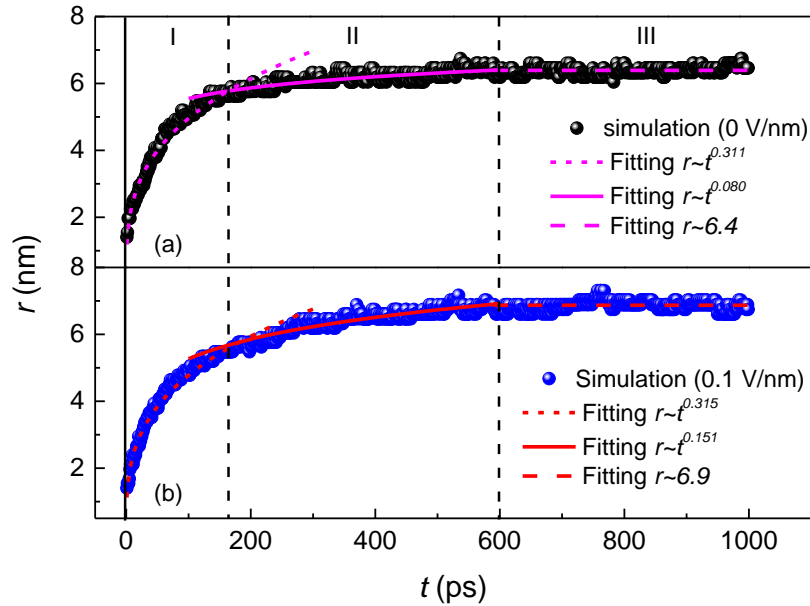


Figure 4-9 Spreading radius  $r$  vs. spreading time  $t$ : equilibrium of the drop reached after  $\sim 600$  ps (a) without electric field ( $r_{eq} \approx 6.3$  nm) and (b) with electric field of  $0.1$  V/nm ( $r_{eq} \approx 6.9$  nm). The two dashed black lines separate the regions of inertial spreading (I), viscous spreading (II), and equilibrium (III). The other lines are power law fits of the spreading radius.



Though the physical scales of nanodrop simulations were orders of magnitude smaller than those scales of experiments, the physics of spreading was similar in both cases: it was characterized by fast inertial and slow viscous stages. Further, the simulations confirmed the experiments: spreading of aqueous drops on surfaces under the influence of an applied electric field yielded a larger spreading exponent and the wetted area at equilibrium was larger compared to the case with no applied field.

#### 4.4.3 Electric double layer near the interface

When a charged surface is immersed in electrolyte solution, the electric field induced by surface charges attracts counterions to the liquid-solid interface. The counterions attracted directly to the surface neutralize the surface charges and reduce the electric potential. Therefore, the concentration of counterions decreases far from the interface. Eventually, there is a layer of counterions beyond which the electric potential is close to zero, as shown in Fig. 4-10. This counterions layer is called “electric double layer” (EDL) or Debye length. For aqueous electrolyte solutions, the thickness of the EDL can be estimated by [127]

$$d_{EDL} \approx \frac{0.304}{\sqrt{c}} \quad (4.1)$$

For the five solutions used in the experiment, the thickness of the EDL is shown in Table 4-3.

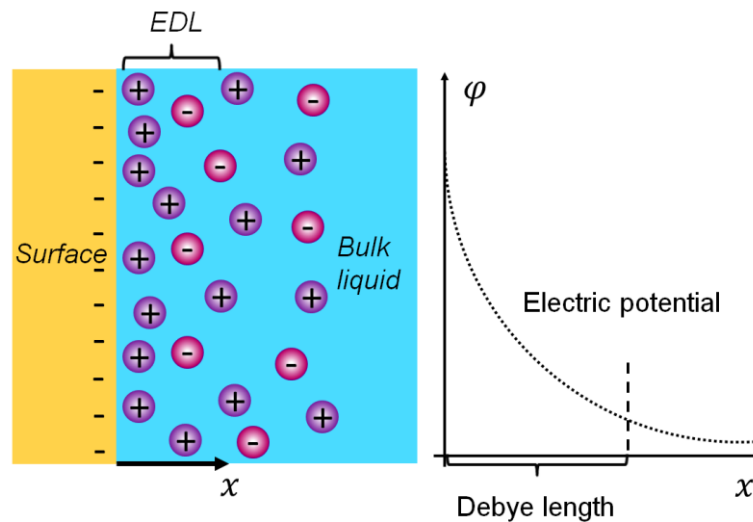


Figure 4-10 Schematic of the electric double layer (left) and the corresponding electric potential (right) near a negatively charged surface.

Table 4-3 The thickness of the electric double layer for five aqueous NaF solutions.

NaF concentration (mol/kg)	Debye length (nm)
0	$\geq 100$
0.001	$\sim 10$
0.01	$\sim 3$
0.04	$\sim 1.5$
0.091	$\sim 1$

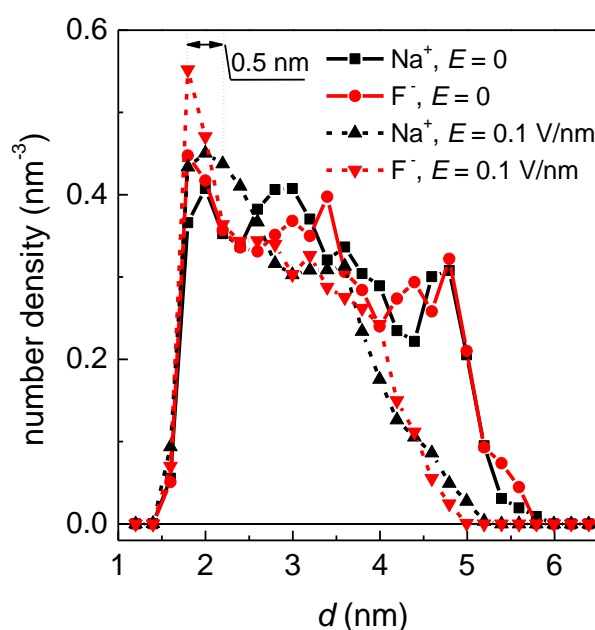


Figure 4-11 Number density distribution of  $\text{Na}^+$  (square) and  $\text{F}^-$  (circle) in a water nanodrop with respect to the distance  $d$  to the silicon surface at equilibrium, with (dashed lines) and without (solid lines) an applied electrical field of 0.1 V/nm.

It was also expected that the electric double layer formed during spreading. Thus, we calculated the average ion number density in the equilibrated nanodrops, from  $\sim 500$  to  $\sim 1,000$  ps. Figure 4-11 shows the number density of  $\text{Na}^+$  and  $\text{F}^-$  ions as a function of the distance to silicon surface. Without electric field, both  $\text{Na}^+$  and  $\text{F}^-$  ions were homogeneously distributed in the nanodrop. However, with the applied electric field, close to the positively charged surface the density of  $\text{F}^-$  increased by  $\sim 22\%$ , while that of  $\text{Na}^+$  increased by  $\sim 12.5\%$  within 0.5 nm from the surface. With

---

$d \gtrsim 0.5$  nm, both  $F^-$  and  $Na^+$  concentrations were nearly constant. Ions moved to the liquid-solid interface and away from the liquid-air interface during spreading, as observed also by Daub *et al.* [143]. From the number density profile, we recognized that anions and cations formed electric double layers close to the interface, with alternating layers of cations and anions, even in the absence of an applied electric field. Upon applying the field, however, the number of ions in the layers closer to the charged surface increased.

---

#### 4.5 Scaling model

---

Till now, the only successful model proposed to describe the inertial wetting dynamics on partial wetting surfaces was done by Bird *et al.* [55]. The scaling model presents in the following section is a modified one based on Bird's model by considering additionally the electrostatic energy.

For dynamic wetting on uncharged surfaces, the only driving force is from the change of surface energy. While the surface is charged or an electric potential is applied, an electric double layer is formed. Since the double layer can be treated as a plate-plate capacitor [127], the electrostatic energy stored in the capacitor serves as additional driving energy. According to the MD simulations, the local ion density ( $Na^+$  and  $F^-$ ) increased by 12.5-22% near the solid-liquid interface in  $\sim 500$  ps when a potential was applied (Fig. 4-11). In the experiments, inertial spreading lasted several milliseconds. For this reason, it seems justified to assume that the building up of the electric double layer by ion migration is much faster compared to spreading in the experiments. Thus, the new energy balance is

$$\int_V \frac{1}{2} \rho |\vec{u}(\vec{x}, t)|^2 dV = \gamma [A(0) - A(t) + \pi r(t)^2 \cos \theta_{eq}] + \Delta E_e \quad (4.2)$$

Where  $\vec{u}(\vec{r}, t)$  is the velocity field as a function of position  $\vec{r}$  and time  $t$ ,  $V$  is the volume of the drop.  $A(0) - A(t)$  is the change of the area of the liquid-air interface during spreading that can be expressed as  $\pi r(t)^2 F(\theta_{eq})$ , with  $F$  some function depending on drop geometry.  $\pi r(t)^2 \cos \theta_{eq}$  is the change of the liquid-solid interface area during spreading, depending on contact angle and on applied potential.  $\Delta E_e$  is the variation of electrostatic energy of the drop during spreading. I assumed that the

drop is a good conductor and thus the electric field inside is zero, except for the region close to the surface, i.e. the extent of the electric double layer with thickness  $d_{EDL}$ . Therefore, I take that  $\Delta E_e$  scales as  $\pi r(t)^2 C' \phi^2$ .  $C' = \frac{\varepsilon_0 \varepsilon_l}{d_{EDL}}$  is the capacitance per unit area of the electric double layer, strongly depending on electrolyte concentration.  $\varepsilon_0$  and  $\varepsilon_l$  are the permittivities of vacuum and liquid, respectively. For any given electrolyte concentration the voltage drop across the double layer has to be corrected for the voltage drops across the oxide layer of thickness  $d_{ox}$  and the silane monolayer with thickness of  $d_{sil}$ . I account for this by scaling  $\phi$  with a constant  $m$ . Substituting it into equation (4.2) and adapting the self-similar velocity field as suggested by Bird *et al.*, a new power law is obtained

$$r = K''' t^{\alpha'} \quad (4.3)$$

Where  $K'''$  is a coefficient and the exponent

$$\alpha' \propto \sqrt{F(\theta_{eq}) + \cos \theta_{eq} + \frac{1}{2} \frac{\varepsilon_0 \varepsilon_l}{d_{EDL}} \frac{(m\phi)^2}{\gamma}} \quad (4.4)$$

From equation (4.4), one finds that the electrospreeding exponent  $\alpha'$  depends on the equilibrium contact angle and on four other parameters: surface tension and permittivity of the liquids, thickness of the electric double layer, and applied potential. For the five electrolyte solutions used, surface tension and permittivity were nearly the same (see Table 4-2). The thickness of electric double layer depends on the electrolyte concentration. With increasing concentration the thickness decreases, as shown in Table 4-2. Thus, the exponent increased with the surface wettability, applied potential, and electrolyte concentration. This is fully consistent with the experimental results shown in Fig. 4-5.

Equation (4.4) also indicates that the degree of enhancement of spreading should be independent of surface wettability. With uncharged surfaces, the exponent only depends on the equilibrium contact angle  $\theta_{eq}$ , i.e.  $\alpha \propto \sqrt{F(\theta_{eq}) + \cos \theta_{eq}}$ . By substituting  $\alpha$  into equation (4.4), one obtains

$$\alpha'^2 - \alpha^2 = \frac{\frac{1}{2} \frac{\varepsilon_0 \varepsilon_L}{d_{EDL}} (m\phi)^2}{\gamma} \quad (4.5)$$

Fig. 4.12 plots  $\alpha'^2 - \alpha^2$  as a function of  $\phi^2$ . As expected, the data points from different wettable surfaces collapsed onto a single curve for each of the five electrolytes. This is consistent with the model.

It must be pointed out here that there is a saturation of  $\alpha'$  for pure water at  $\phi \gtrsim 200 V$  and for water with  $c \approx 0.001 \text{ mol/kg NaF}$  at  $\phi \gtrsim 300 V$ , but not at higher electrolyte concentrations (Fig. 4.5 and Fig. 4.12). This phenomenon is similar to electrowetting, where a saturation of the contact angle is observed as a function of the applied potential but is not yet understood [151]. The saturation of the spreading exponent observed in the experiments depended on salt concentration and applied potential. This is still an open question and will require further investigations. The value of  $\alpha'^2 - \alpha^2$  and the slope of the  $\alpha'^2 - \alpha^2$  vs.  $\phi^2$  curves is higher for drops with higher electrolyte concentration, as one would expect from equation (4.5). A more quantitative description of the dependence must also be addressed in future work.

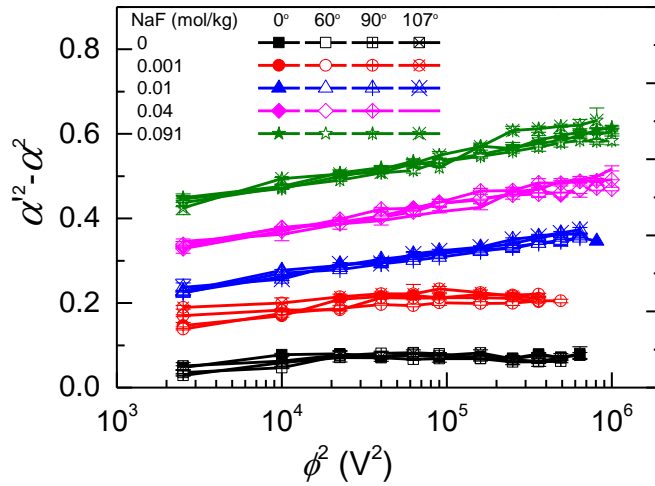


Figure 4-12  $\alpha'^2 - \alpha^2$  vs.  $\phi^2$ . , replotted from Fig. 4-5a with corresponding symbols.

For clarity of representation, differently colored data sets are offset vertically by the value of 0.1.

---

---

## 4.6 Summary

---

The early stage of dynamic wetting of aqueous electrolyte drops on various wettable surfaces was investigated under different applied potentials. The initial electrospreading radius followed a power law with an exponent increasing with the potential. This indicates that electrostatic effects did not only control the equilibrium contact angle, like in electrowetting, but also the speed of spreading and thus wetting dynamics. Moreover, the electrolyte concentration influenced the wetting exponent as well. Based on experimental and simulation results, a model at the level of a scaling law accounting for energy conservation was proposed to capture the dependence between the wetting exponent and surface wettability, applied potential, and electrolyte concentration.

---

## 5 Effects of Surface Wettability and Liquid Viscosity on Dynamic Wetting

---

In this chapter, I will present the effects of surface wettability and liquid viscosity on wetting dynamics. In particular, dynamic wetting of various viscous liquids on solid surfaces with different wettability was investigated. In order to show the viscous effects, aqueous solutions with surface tensions similar to water but very different viscosities (maximum 60 times) were used. To identify the effects of surface wettability, surfaces with equilibrium contact angles from  $\sim 0^\circ$  to  $\sim 110^\circ$  were studied. The experimental results indicated that both liquid viscosity and surface wettability influence the wetting dynamics. In the inertial wetting stage, the inertial wetting coefficient was influenced by both surface wettability and liquid viscosity, while the inertial exponent was only dependent on the surface wettability. These findings will be discussed based on the analysis of the effective mass of the moving drop. The duration of the inertial wetting was longer for highly viscous liquids than for low viscous liquids due to viscous damping. The viscous wetting stage was only observed on surfaces with  $\theta_{eq}$  smaller than a critical value  $\theta_c$ , which depended on viscosity. A scaling analysis was developed based on Navier-Stokes equations and the proposed  $\theta_c$  matches with experimental observations.

---

### 5.1 Motivation

---

As reviewed in the first chapter, dynamic wetting may proceed with three stages. About 1 to 100  $\mu s$  after the drop contacts the surface, inertia of the moving drop resists the capillary force that drives spreading. The spreading dynamics follows a power law  $r = Kt^{0.5}$ , which is independent of the liquid viscosity and surface wettability [52, 54].  $r$  is the spreading radius,  $t$  is the spreading time and  $K$  is a coefficient. With time between  $\sim 0.1$  to 10 ms, wetting is still dominated by inertia. However, the surface wettability starts to influence spreading and the spreading radius grows with time according to another power law,  $r = K't^\alpha$  [35, 36, 55].  $K'$  is another coefficient and the exponent  $\alpha$  is only dependent on surface wettability, i.e.  $\theta_{eq}$ . Experimental study showed that  $\alpha$  increases from  $\sim 0.25$  for  $\theta_{eq} \approx 120^\circ$  to  $\sim 0.5$  for  $\theta_{eq} \approx 0^\circ$  [35, 36, 55]. On very hydrophilic surfaces ( $\theta_{eq} \ll \sim 57.3^\circ$  or 1 radian) or

---

completely wetting surfaces ( $\theta_{eq} \approx 0^\circ$ ), a slow wetting stage was observed after the inertial stages. In this stage, the viscous friction inside the drop is the main source opposing capillarity. The wetting dynamics follows the Tanner's law:  $r = R_0 \left( \frac{\gamma}{\mu R_0} \right)^{0.1} t^{0.1}$  [1, 18, 57, 58].

In literature, much efforts were devoted to study the influence of surface properties, such as wettability [52, 54, 55], softness [35, 36] and solubility [66] on dynamic wetting. In contrast, the influence of liquid properties, such as viscosity, has attracted little attention [152]. Intrinsically, one would expect that highly viscous liquids spread slower than low viscous liquids. Thus, a natural question is if liquid viscosity influences the early dynamic wetting? If it does, how and to which extent? The viscous wetting stage, well described by Tanner's law, was only observed on very hydrophilic and completely wetting surfaces [54, 58, 59, 61]. Does it also exist on partial wetting surfaces? Keeping these questions in mind, a study of the influence of surface wettability and liquid viscosity on dynamic wetting was carried out.

---

## 5.2 Experiments

---

### 5.2.1 Surfaces and liquids

---

Five types of wettable surfaces were prepared using a variety of coatings (Table 5-1). Smooth glass slides were cleaned in acetone (Sigma-Aldrich, p.a.) and then ethanol (Sigma-Aldrich, p.a.) in an ultrasonic bath for 5 min each. After rinsing in Milli-Q water, the surfaces were dried with nitrogen. With treatment of oxygen plasma (Femto, Diener Electronic GmbH, Germany) for another 5 min, completely wetting surfaces were obtained, i.e. surface 1. The other two hydrophilic surfaces, surface 2 and surface 3, were prepared following a standard silanization procedure [1]. The two hydrophobic surfaces, surface 4 and surface 5, were fabricated by silanization of oxygen plasma treated glass slides in a vapour phase in a desiccator at 100 °C overnight. Wetting experiments were done with pure water and four water-glycerol mixtures. These liquids have a similar surface tension (the difference is less than 17%) but a remarkably different viscosity. The maximum viscosity is 60 times that of water (Table 5-1). The equilibrium contact angles of these liquids on the five



used surfaces were measured after each wetting experiment and are also shown in Table 5-1.

Table 5-1 Physical properties of the liquids and corresponding equilibrium contact angles on substrates modified by different types of coatings.

Surfaces	$\theta_{eq}$ (°)				
Wt. % glycerol	0	40	60	75	80
Viscosity $\mu$ (cP) [153]	1.0	3.7	10.7	35.5	60.1
Density $\rho$ (kg/m <sup>3</sup> ) [154]	998.2	1099.3	1153.8	1194.9	1208.5
Surface tension $\gamma$ (mN/m) [155]	72.8	69.2	67.2	63.5	62.3
1. Silicon dioxide	0	0	0	0	0
2. Triethoxysilylbutyraldehyde	41±4	41±6	34±5	40±7	41±5
3. 3-Aminopropyltriethoxysilane	63±5	56±5	57±10	54±3	60±11
4. 1, 1, 1, 3, 3, 3-Hexamethyldisilazan	92±5	85±3	92±6	87±8	104±5
5. 1H,1H,2H,2H-Perfluorodecyltriethoxysilane	112±4	105±6	107±5	109±11	110±6

### 5.2.2 Observation of the wetting process

Pendant drops with radii  $R_0$  of 0.5-1.2 mm were generated and quasi-statically approached to the surfaces using a syringe pump (the approaching speed was ~0.1 mm/s before drops touched the surface). Both the needle and substrate were grounded to prevent the influence of electrostatics on spreading [79, 156]. The spreading process was recorded using a high-speed camera (FASTCAM SA-1, Photron Inc.). The early wetting stage was recorded a rate of 54,000 fps and the later wetting stage was recorded with 10,000 fps. Each wetting experiment was repeated at least 6 times. In total, I analyzed more than 350 experiments.

### 5.2.3 Data analysis

The spreading radius  $r$  was extracted from the recorded movies with an ad-hoc developed MATLAB (MathWorks Inc.) algorithm. Since the early wetting dynamics is

dominated by inertia, the Pearson product-moment correlation coefficient,  $\zeta$ , was used to check the power law relationship between  $r$  and  $t$ .

$$\zeta = \frac{\sum_{i=1}^n (r'_i - \bar{r}') (t'_i - \bar{t}')}{\sqrt{\sum_{i=1}^n (r'_i - \bar{r}')^2} \sqrt{\sum_{i=1}^n (t'_i - \bar{t}')^2}}, r' = \log r, t' = \log t, \bar{r}' = \frac{1}{n} \sum_{i=1}^n r'_i, \bar{t}' = \frac{1}{n} \sum_{i=1}^n t'_i$$

$\zeta$  has a value between -1 and 1.  $\zeta$  equals to 1 or -1 corresponds to a very good linear relationship between  $\log r$  and  $\log t$ , i.e. a very strong power law relationship between  $r$  and  $t$ .

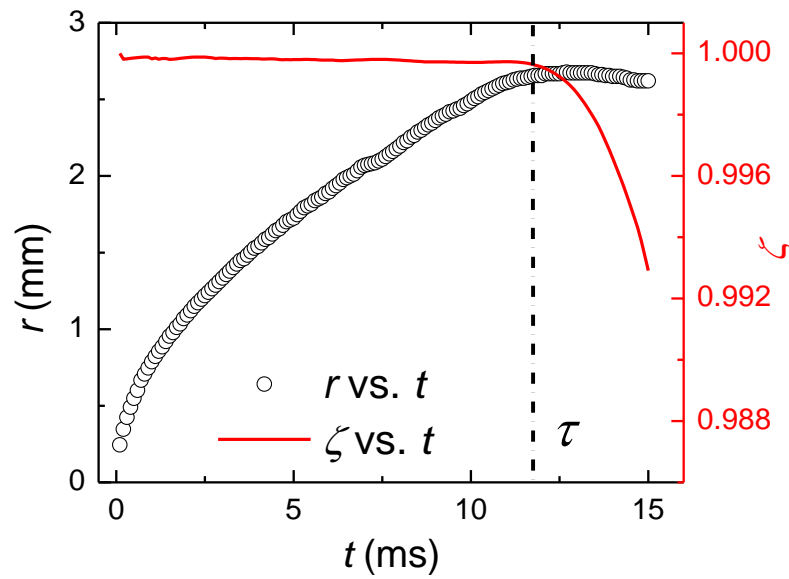


Figure 5-1 Spreading radius  $r$  and the linear correlation coefficient  $\zeta$  between  $\log r$  and  $\log t$  as a function of time  $t$ . The substrate is silicon oxide and the drop is water with  $R_0 \approx 1.2$  mm.

The inertial wetting time was determined from the curve of  $\zeta$  vs.  $t$ . For example, Fig. 5-1 shows the spreading radius  $r$  and corresponding  $\zeta$  as a function of time  $t$  for the spreading of a water drop on a completely wetting surface.  $\zeta$  is  $\sim 1$  when  $t$  is smaller than a characteristic time  $\tau \approx 12$  ms, beyond which  $\zeta$  starts to diverge. This indicates that the wetting with  $t \leq \tau$  follows a power law,  $r = K't^\alpha$ , and the wetting is dominated by inertia. Thus, the experimental data with  $t \leq \tau$  was fitted by a power law using the least square method (LSM). Since viscous wetting may proceed after the inertial wetting stage [1, 18, 58], the remaining spreading data was also fitted with power law.

---

## 5.3 Results and discussion

---

### 5.3.1 Effects of surface wettability

---

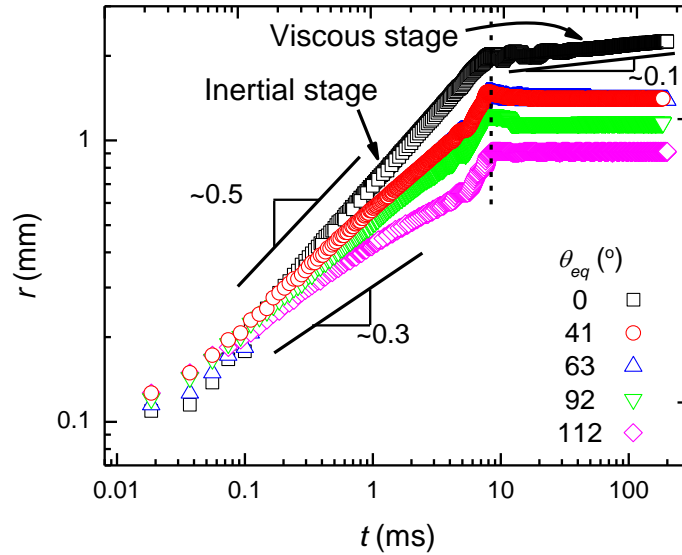


Figure 5-2 Log-log plot of spreading radius  $r$  as a function of time  $t$  of water drops on five wettability surfaces. Drop radius was always  $R_0 \approx 0.9$  mm.

Figure 5-2 shows the log-log plot of  $r$  vs.  $t$  of water drops spreading on five surfaces with different wettability. Drops spread faster on relatively hydrophilic surfaces than on relatively hydrophobic surfaces. The wetting followed a power law  $r = K't^\alpha$  for  $t \lesssim 8$  ms. The slope, i.e.  $\alpha$ , was dependent on the surface wettability and increased from  $\sim 0.3$  to  $\sim 0.5$  while  $\theta_{eq}$  decreases from  $\sim 112^\circ$  to  $\sim 0^\circ$ , which was consistent with previous studies [36, 54, 55, 66]. On partially wettability surfaces (here  $\theta_{eq} \gtrsim 41^\circ$ ), water drops reached equilibrium after the inertial wetting stage, as shown in Figure 5-2. In contrast, on completely wetting surfaces, a slower wetting process was observed for  $t \gtrsim 8$  ms. The power law fitting of the data gave a slope of  $\sim 0.1$ , which indicates that spreading was dominated by viscous dissipation [1, 18, 58, 61]. Generally, it was found that the surface wettability influenced both inertial and viscous wetting stages.

---

### 5.3.2 Effects of liquid viscosity

---

Figure 5-3 displays the growth of spreading radius as a function of time for various liquids on a partial wetting surface ( $\theta_{eq} = 63^\circ$ ). Early spreading was also dominated by inertia and followed a power law with  $\alpha \sim 0.44$  for all liquids. However, the growth of spreading radius was slower for liquids with higher viscosity. This shows that the inertial coefficient  $K'$  decreased with  $\mu$ . Moreover, the inertial wetting time  $\tau$  slightly increased from  $\sim 8$  ms to  $\sim 10$  ms as  $\mu$  increased from 1 cP to 60.1 cP.

For low viscous liquids with  $\mu \lesssim 10.7$  cP, no viscous wetting was observed and the drops reached equilibrium after inertial wetting. For liquids with  $\mu \gtrsim 35.5$  cP, the drops were not at equilibrium after the inertial stage, and they further spread according to the viscous power law,  $r \sim t^{0.1}$ . In summary, I observed that the liquid viscosity influenced inertial and viscous wetting dynamics.

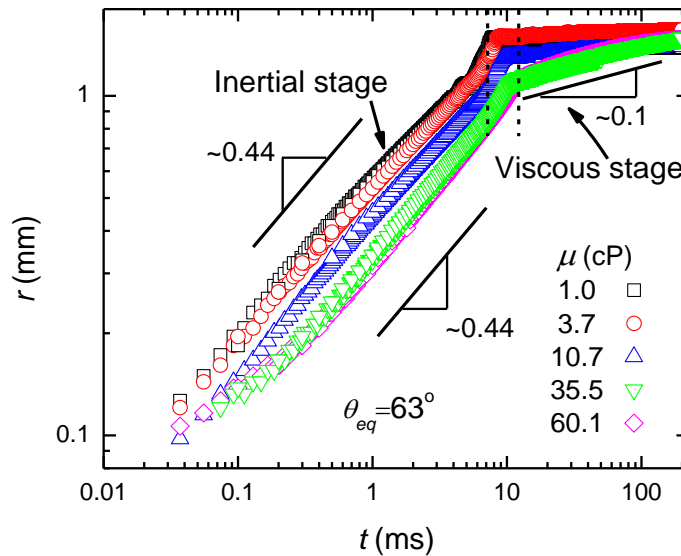


Figure 5-3 Log-log plot of spreading radius  $r$  as a function of time  $t$  of various liquids on a partial surface ( $\theta_{eq} \approx 63^\circ$ ). Drop radius was always  $R_0 \approx 0.9$  mm.

---

### 5.3.3 Inertial wetting

---

#### *Inertial wetting exponent*

The experimental data for  $t \lesssim \tau$  was fitted with the power law  $r = K't^\alpha$ , using the LSM. The inertial wetting is well known that the exponent is only dependent on

the chemical interaction between liquids and surfaces, i.e.  $\theta_{eq}$  [9, 36, 55]. Figure 5-4a summarizes  $\alpha$  of different liquid drops spreading on various surfaces.  $\alpha$  has a value of 0.3-0.5 and decreases with  $\theta_{eq}$  regardless of drop viscosity, density, and size. This is consistent with theoretical predictions [35, 55] and experimental results [35, 54, 55, 66] in the literature. Most recently, Legendre and Maglio reported in a theoretical and simulation paper that if the early wetting was dominated by viscous dissipation, the spreading should follow a power with  $\alpha = 2/3$  [157]. However, in my experiments, I found that the maximum  $\alpha$  for all liquids was 0.5 and that  $\alpha$  was only dependent on  $\theta_{eq}$ . This confirms that the early stage of spreading or wetting is dominated by inertia.

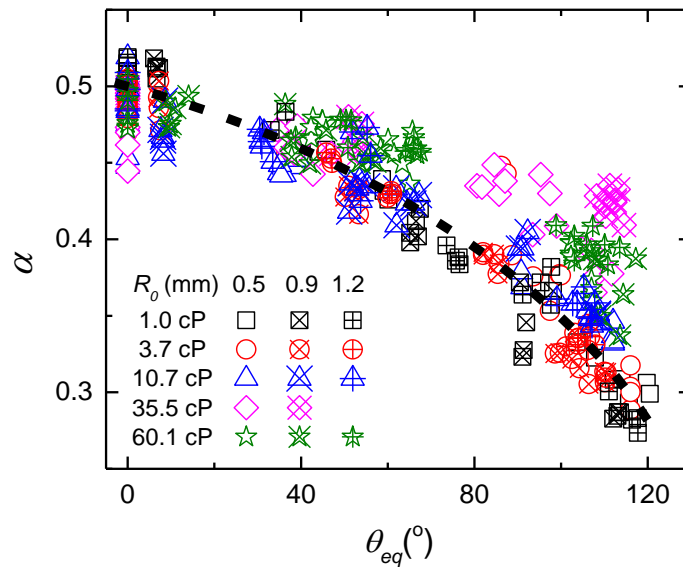


Figure 5-4  $\alpha$  as a function of  $\theta_{eq}$  for drops with five different viscosity and three sizes. Dashed line is a guide for eyes.

#### *Inertial wetting coefficient*

Figure 5-5a-c shows the coefficient  $K'$  for all spreading experiments. With the same surface and liquid,  $K'$  was larger for larger drops, which is an evidence for inertial wetting and was also observed by Bird *et al.* [55]. For a specific drop size,  $K'$  was smaller for higher viscous liquids. Moreover, with increasing  $\theta_{eq}$ ,  $K'$  decreased (Figure 5-5b-d). Generally,  $K'$  was determined by drop size, liquid viscosity, and surface wettability, i.e.  $K' = K'(R_0, \mu, \theta_{eq})$ .

Figure 5-5d shows the normalized inertial coefficient,  $C = \frac{Kt\tau_i^\alpha}{R_0}$ , from the normalized power law,  $\frac{r}{R_0} = C\left(\frac{t}{\tau_i}\right)^\alpha$ , as a function of  $\theta_{eq}$  and  $\mu$  for three different drop sizes.  $\tau_i = \sqrt{\frac{\rho R_0^3}{\gamma}}$  is the characteristic inertial time. The coefficient for different drop sizes collapsed into five curves, each of which corresponding to one viscosity, and each curve decreased with  $\theta_{eq}$ . This is a further evidence that the early wetting dynamics is dominated by inertia, but it is influenced by liquid viscosity and surface wettability as well.

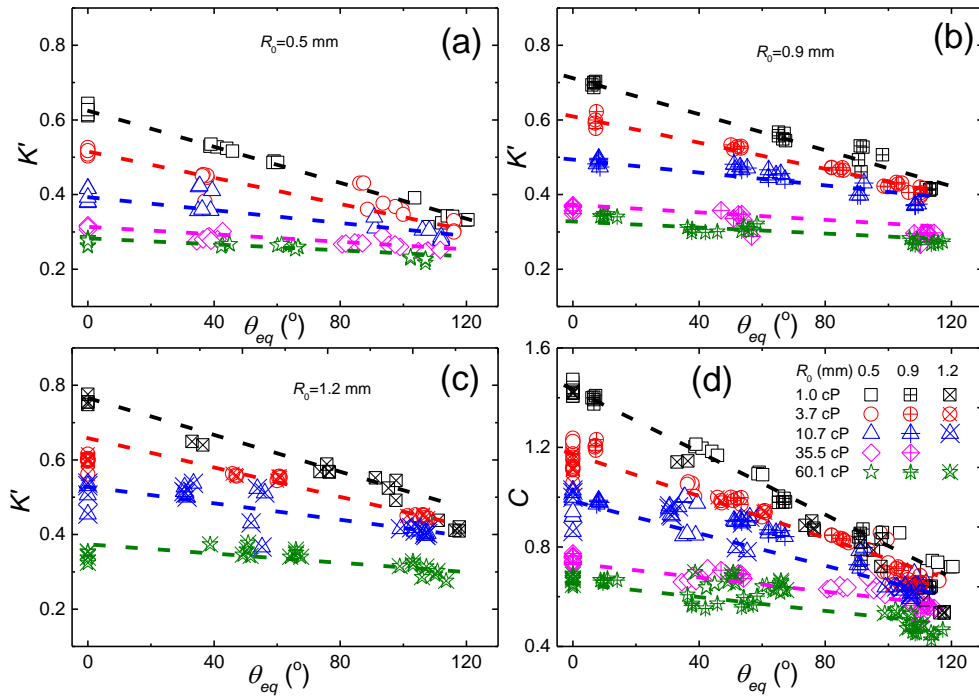


Figure 5-5 (a)-(c) coefficient of power law  $K'$  as function of  $\theta_{eq}$  and  $\mu$  for three drop sizes. (d) Normalized inertial coefficient  $C$  as a function of  $\theta_{eq}$  and  $\mu$ . The dashed lines are guides for the eye.

Now, the question is how do surface wettability and liquid viscosity influence the inertial wetting coefficient? In the paper by Bird *et al.*, the authors derived the power law for inertial wetting based on energy conservation [55]. They considered that the change of surface energy during spreading was transferred into the kinetic

energy of the moving drop within a self-similar velocity field over a length scale of  $l_v \propto \left(\frac{\gamma t^2}{\rho}\right)^{1/3}$ . In other words, the effective mass of the moving drop scales as  $\rho l_v^3$ . Thus, one possibility is that surface wettability and liquid viscosity influence the effective mass of spreading drops, i.e. the scale of the velocity field  $l_v$ .

In order to estimate the dimensions of the velocity field, I tracked the profiles of the spreading drops. As illustrated in Fig. 5-6, I overlapped the surface profiles of a spreading drop at time  $t$  and  $t + \Delta t$ . I found a length scale above the surface,  $l$ , below which the liquid in the drop spread during  $\Delta t$ . Thus,  $l$  can be treated as a length scale characterizing the velocity field at time  $t + \Delta t$ . However, it was found that  $\Delta t$  should not be too small to still allow identifying the changing profiles. The minimum time step that used to extract  $l$  from the experimental data is  $\Delta t = 0.1$  ms.

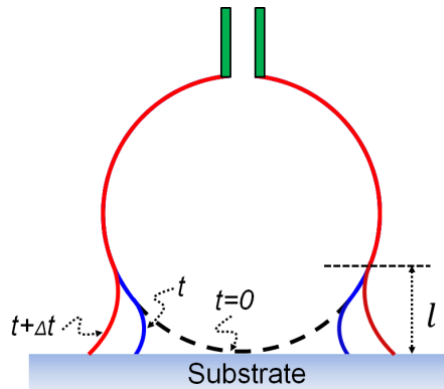


Figure 5-6 Schematic of the change of the drop surface profile during spreading.

Figure 5-7a shows  $l$  versus  $t$  for a 0.9 mm-radius water drop spreading on various surfaces. Indeed,  $l$  initially grew with  $t$  according to  $l = k' \left(\frac{\gamma t^2}{\rho}\right)^{1/3}$  on all five surfaces. Similar trends were also observed for liquids with different viscosities (Fig. 5-7b). These confirm the assumption by Bird *et al.* [55] that liquid flows within a self-similar velocity field with  $l_v \propto \left(\frac{\gamma t^2}{\rho}\right)^{1/3}$ . However, the process describing the developing velocity field was related to surface wettability and liquid viscosity, i.e.  $k' = k'(\theta_{eq}, \mu)$ . As shown in Fig. 5-7a & b,  $k'$  is smaller for more hydrophobic surfaces and for more viscous liquids.

After a characteristic time  $t_M$ , which is always smaller than  $\tau$ ,  $l$  reached a maximum extension  $l_M$  and then kept nearly constant until the end of inertial wetting. Both  $t_M$  and  $l_M$  are also dependent on  $\theta_{eq}$  and  $\mu$ , as summarized in Fig. 5-7c and Fig. 5-7d, respectively. For the same liquid, both  $t_M$  and  $l_M$  increased with  $\theta_{eq}$ , i.e. it took longer to reach the maximum extension of the velocity field on hydrophobic surfaces, and the corresponding  $l_M$  was larger (Fig. 5-7c). For the same surfaces, both  $t_M$  and  $l_M$  were larger for higher viscous liquids. In summary, the velocity field in the spreading drop develops in a self-similar way, which is controlled by surface wettability and liquid viscosity.

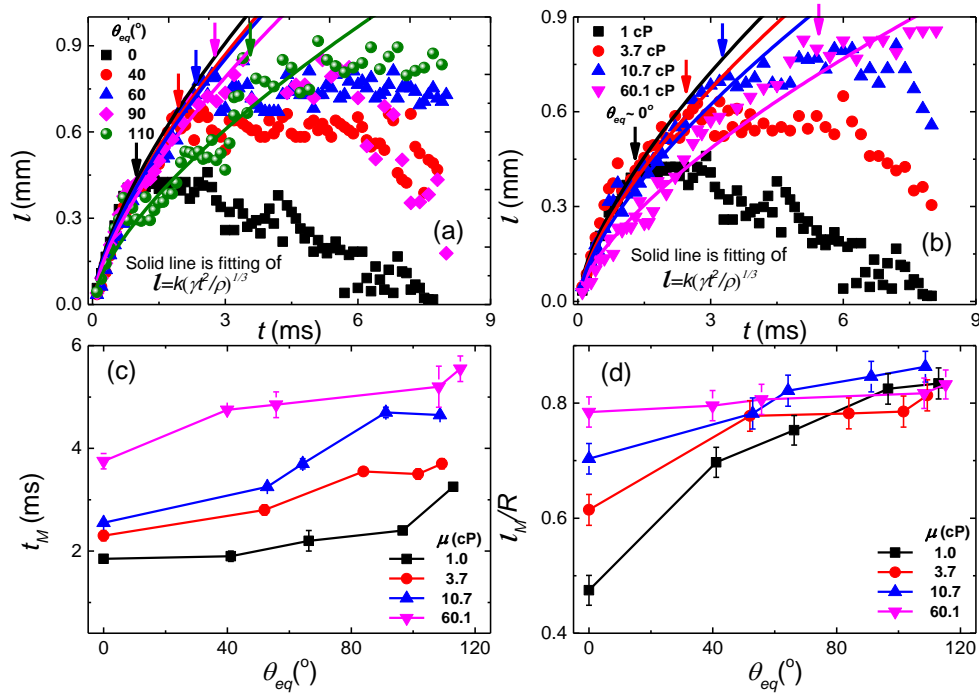


Figure 5-7 (a) The extension of the velocity field  $l$  as a function of spreading time  $t$  for water on various wettable surfaces. (b) The extension of the velocity field  $l$  as a function of spreading time  $t$  for different liquids on a completely wetting surface. The arrows in (a) and (b) indicate the maximum length scale  $l_M$ . (c) The time  $t_M$  needed to reach the maximum length scale as a function of  $\theta_{eq}$  and liquid viscosity. (d)  $l_M$  as a function of  $\theta_{eq}$  and liquid viscosity. Drop radius was always  $R_0 \approx 0.9$  mm.



---

Since  $\theta_{eq}$  and  $\mu$  influence the development of the self-similar velocity field during drop spreading, they eventually influence the inertial power law. However, this effect is difficult to integrate into the inertial wetting power law. Instead of a quantitative analysis, a qualitative explanation is given here. For spreading with a large value of  $t_M$  and  $l_M$ , i.e. for wetting of highly viscous liquids or on hydrophobic surfaces, the effective mass of the spreading drop is large, and hence the spreading velocity will be slower, as the driving capillary force is always similar during the whole inertial wetting stage. Since the early wetting dynamics is dominated by inertia and the inertial exponent  $\alpha$  is independent of  $\mu$ , a smaller coefficient  $C$  or  $K'$  can reasonably be expected. This argument is consistent with our observation in Fig. 5-5a-d.

Most recently, Carlson and co-workers considered the influence of surface wettability and liquid viscosity on dynamic wetting by introducing additional energy dissipations such as contact line friction due to molecular process, viscous dissipation in the liquid, as well as a diffusive dissipation [158-160]. However, these contributions are hard to be directly integrated into the inertial wetting power law as well.

#### *Inertial wetting time*

The inertial wetting of these liquids lasted only from a few to few tens of milliseconds, depending on drop size. Then the drop reached equilibrium or entered into the slower viscous wetting stage. Figure 5-8a shows the inertial time  $\tau$  as a function of  $\theta_{eq}$  for four different liquids. Similar to other studies [36, 54, 55], I found that inertial time  $\tau$  was independent of  $\theta_{eq}$  and was always larger than the characteristic inertial time  $\tau_i = \sqrt{\frac{\rho R_0^3}{\gamma}}$ . Moreover, I also observed that  $\tau$  was larger for higher viscous liquids. Biance *et al.* suggested that the inertial wetting stops at the crossover from the inertial to the viscous wetting stage [54]. They found that inertial wetting is shorter for higher viscous liquids, which contradicts the results observed here. Another model to explain the duration of inertial wetting was proposed by Bird *et al.* [55]: inertial wetting lasts as long as the capillary waves propagate along the drop. Based on the vibration model of suspended drops proposed by Lamb [77], I

found the actual inertial time  $\tau \approx 2.22\tau_i$  for low viscosity liquids, as discussed in Chapter 2. Figure 5-8b summarizes the inertial wetting time  $\tau$  as a function of  $\tau_i$  for various drop sizes and liquids.  $\tau$  linearly increased with  $\tau_i$  and was very close to the theoretical prediction for low viscosity liquids, such as water. For higher viscosity liquids,  $\tau$  was larger than the prediction and increased with  $\mu$  (for the most viscous liquid,  $\tau \approx 4.0\tau_i$ ). This phenomenon may due to the viscous damping of the capillary wave propagation. In Lamb's model [77], the vibrating drop was treated as a spring, as the liquid was considered to be inviscid. For the vibration of viscous drops, the viscous damping effects will causes a decreases of the vibration frequency [161], and hence results in  $\tau > 2.22\tau_i$ .

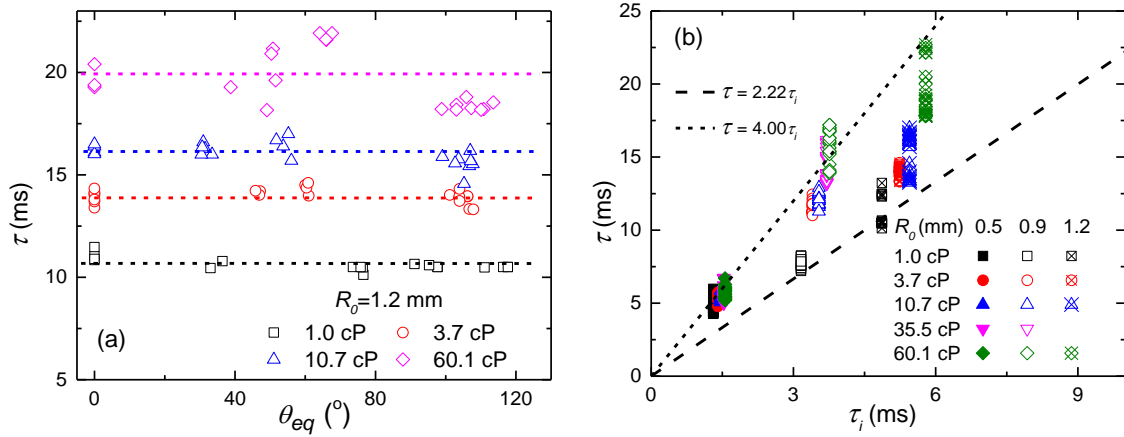


Figure 5-8 (a) Inertial wetting time  $\tau$  as a function of  $\theta_{eq}$  for four liquids with different viscosity on completely wetting surfaces. The drop size  $R_0$  is 1.2 mm (b)  $\tau$  as a function of  $\tau_i$  for various liquids with different drop sizes.

### 5.3.4 Viscous wetting

With ongoing spreading, the inertial resistance lessens and the viscous dissipation in the drop may become dominant [54, 55]. However, the viscous wetting stage was only observed on surfaces with an equilibrium contact angle smaller than a critical value  $\theta_c$  for each liquid. As illustrated in Figure 5-9,  $\theta_c$  increased with  $\mu$ . Since the Reynolds number compares inertial and viscous forces, I analyzed  $Re$  during the spreading. Due to the symmetry of the spreading, the two dimensional Navier-Stokes (N-S) equations with the incompressibility condition were applied,

$$\rho \left( u \frac{\partial u}{\partial x} + v \frac{\partial u}{\partial y} \right) = -\frac{\partial p}{\partial x} + \mu \left( \frac{\partial^2 u}{\partial x^2} + \frac{\partial^2 u}{\partial y^2} \right) \quad (5.1)$$

$$\rho \left( u \frac{\partial v}{\partial x} + v \frac{\partial v}{\partial y} \right) = -\frac{\partial p}{\partial y} + \mu \left( \frac{\partial^2 v}{\partial x^2} + \frac{\partial^2 v}{\partial y^2} \right) \quad (5.2)$$

$$\frac{\partial u}{\partial x} + \frac{\partial v}{\partial y} = 0 \quad (5.3)$$

Where  $u$  and  $v$  are the velocity components in the tangential and the vertical directions, respectively.  $p$  is the pressure. The left terms in equation (5.1) and (5.2) are inertial terms and the last terms in equation (5.1) and (5.2) are viscous terms. Let  $U^*$  and  $V^*$  be the characteristic velocities, and  $R^*$  and  $H^*$  the characteristic length of contact radius and height of the spreading drop. From the nondimensional form of equation (5.3) one obtains

$$V^* = \varepsilon_a U^*, \quad \text{with } \varepsilon_a = \frac{H^*}{R^*} \quad (5.4)$$

With the above expression, the inertial and viscous terms in equation (5.1) can be further estimated as

$$\rho u \frac{\partial u}{\partial x} \sim \rho v \frac{\partial u}{\partial y} \sim \frac{\rho U^{*2}}{R^*} \quad (5.5)$$

$$\mu \frac{\partial^2 u}{\partial x^2} \sim \frac{\mu U^*}{R^{*2}}, \quad \text{and} \quad \mu \frac{\partial^2 u}{\partial y^2} \sim \frac{\mu U^*}{\varepsilon_a^2 R^{*2}} \quad (5.6)$$

In the inertial stage,  $R^* \sim H^* \sim R_0$ ,  $\mu \frac{\partial^2 u}{\partial x^2} \sim \mu \frac{\partial^2 u}{\partial y^2} \sim \frac{\mu U^*}{R^{*2}}$ . In the viscous stage, the drop height is always much smaller than the contact radius [1, 18, 57], i.e.  $\varepsilon_a \ll 1$ , which leads to  $\mu \frac{\partial^2 u}{\partial x^2} \ll \mu \frac{\partial^2 u}{\partial y^2}$ . Thus, the Reynolds number in both wetting stages takes the same form

$$Re \sim \frac{\rho u \frac{\partial u}{\partial x}}{\mu \frac{\partial^2 u}{\partial y^2}} \sim \varepsilon_a^2 \frac{\rho U^* R^*}{\mu} \quad (5.7)$$

At the end of the inertial wetting stage,  $R^* \sim R_0$  and the characteristic tangential velocity scales as  $U^* \sim \sqrt{\frac{\gamma}{\rho R_0}}$ . The viscous wetting can only be observed while the viscous force dominate over the inertial force

$$Re \sim \varepsilon_a^2 \frac{\rho U^* R^*}{\mu} \sim \varepsilon_a^2 \frac{\rho}{\mu} \sqrt{\frac{\gamma R_0}{\rho}} < 1 \quad (5.8)$$

Solving equation (5.8), one finds that a viscous spreading drop should have a shape of  $\varepsilon_a < \frac{\mu^{1/2}}{(\rho R_0 \gamma)^{1/4}}$ . Making a reasonable assumption that the shape of the drop is hemispherical and the contact angle is close to  $\theta_{eq}$ , I finally obtain the criteria for surface wettability for viscous wetting

$$\theta_{eq} < \theta_c = \sin^{-1} \frac{2\varepsilon_{ac}}{1 + \varepsilon_{ac}^2}, \quad \text{and } \varepsilon_{ac} = \frac{\mu^{1/2}}{(\rho R_0 \gamma)^{1/4}} \quad (5.9)$$

As shown in Figure 5-9, the critical  $\theta_c$  predicted in equation (5.9) (red dashed line) matches our experimental results very well.

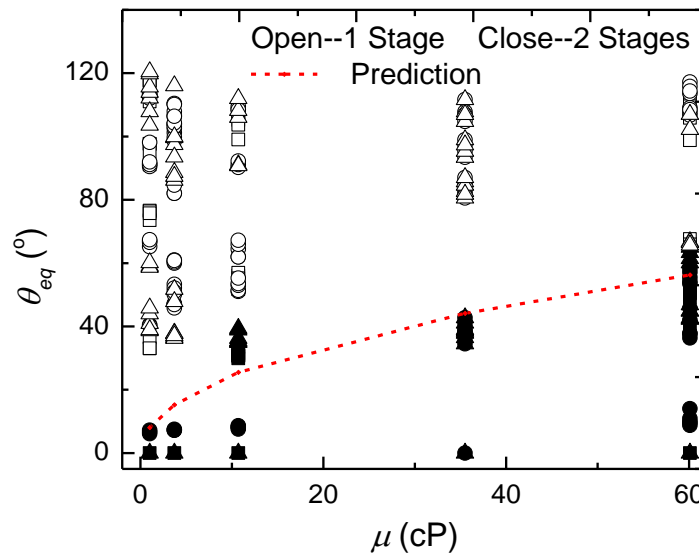


Figure 5-9 Wetting phase diagram of drops spreading on solid surfaces as a function of liquid viscosity  $\mu$  and equilibrium contact angle  $\theta_{eq}$ . Symbol shapes indicate different drop size  $R_0$ : ( $\blacksquare$ ,  $\square$ ) 1.2 mm, ( $\bullet$ ,  $\circ$ ) 0.9 mm and ( $\blacktriangle$ ,  $\triangle$ ) 0.5 mm. The open symbols denote that one stage was observed and the closed symbols denote that two stages were observed. The red dashed line represents  $\theta_c = \sin^{-1} \frac{2\varepsilon_{ac}}{1 + \varepsilon_{ac}^2}$ .

---

---

## 5.4 Summary

---

Both surface wettability and liquid viscosity influence inertial and viscous wetting. During the inertial wetting stage, the inertial exponent only depends on surface wettability, while the inertial wetting coefficient is controlled by both surface wettability and liquid viscosity. This is because the effective mass of the spreading drop is influenced by the surface wettability and the liquid viscosity. On the other hand, the viscous wetting stage only exists on surfaces with equilibrium contact angle smaller than a critical value, which depends on the liquid viscosity. Based on the two dimensional Navier-Stokes (N-S) equation, a scaling analysis was proposed to interpret these experimental results.

---

---

## 6 Conclusion

---

In this work, dynamic wetting of simple liquids on complex surfaces and viscous liquids on simple surfaces has been investigated. The early wetting dynamics was always dominated by capillarity and inertia, i.e. the change of surface energy was transferred into the kinetic energy, but influenced by surface and liquid properties, and external forces.

- On bulk flat surfaces, the inertial wetting was slower for higher viscous liquids or on more hydrophobic surfaces, as both increases of liquid viscosity and surface hydrophobicity increased the effective moving mass of drop. On rigid surfaces, inertial wetting lasted as long as the capillary waves propagate along the drop. Since viscous damping could decrease the frequency of capillary waves, inertial wetting was longer for higher viscous liquids. The inertial wetting was shorter on relatively soft substrates than that on rigid surfaces. This was due to the “viscoelastic braking” induced by the “wetting ridge” near the contact line.
- The inertial wetting of flat rigid surfaces could be enhanced by applying an external electric field, as the electrostatic energy served as additional driving force. The wetting speed was not only dependent on the surface wettability and on the applied potential but also on the electrolyte concentration.
- For small particles, the particles were driven into the liquid spontaneously by capillary force. The capillary force was larger for hydrophilic particles than for hydrophobic particles.

The above findings do not only provide us the fundamental knowledge of early wetting dynamics but also tell us how to actively control the early wetting process.

After the inertial wetting stage, wetting stopped or proceeded with another dynamics depending on the liquid viscosity, surface wettability and surface softness. On rigid surfaces, wetting only continued on specifically wettable surfaces, i.e. on surfaces showing a characteristic contact angle, whose value was dependent also on the liquid viscosity. This wetting stage was dominated by viscous dissipation in the drop and could be observed only while the viscous force dominated over the inertial force. On soft substrates, viscoelastic dissipation was the main source to resist



spreading in the second wetting stage. It was only observed for liquids with high surface tension on very soft substrates.

---

## 7 References

---

1. de Gennes, P. G.; Brochard-Wyart, F.; Quere, D., *Capillarity and wetting phenomena: drops, bubbles, pearls, waves*. Springer: New York, **2004**.
2. de Laplace, P. S., *Traité de Mécanique Céleste*. Paris, France, **1805**.
3. Young, T., An essay on the cohesion of fluids. *Phil. Trans. R. Soc. Lond.* **1805**, 95, 65-87.
4. Förch, R.; Schönherr, H.; Jenkins, A. T. A., *Surface design: applications in bioscience and nanotechnology*. Wiley-VCH: **2009**.
5. Roach, P.; Shirtcliffe, N. J.; Newton, M. I., Progress in superhydrophobic surface development. *Soft Matter* **2008**, 4, (2), 224-240.
6. Good, R. J., Contact angle, wetting, and adhesion: a critical review. *J. Adhes. Sci. Technol.* **1992**, 6, (12), 1269-1302.
7. Wenzel, R. N., Resistance of solid surfaces to wetting by water. *Ind. Eng. Chem.* **1936**, 28, 988-994.
8. Cassie, A. B. D.; Baxter, S., Wettability of porous surfaces. *Trans. Faraday Soc.* **1944**, 40, 546-551.
9. Bico, J.; Thiele, U.; Quere, D., Wetting of textured surfaces. *Colloid Surf. A-Physicochem. Eng. Asp.* **2002**, 206, (1-3), 41-46.
10. Quere, D., Non-sticking drops. *Rep. Prog. Phys.* **2005**, 68, (11), 2495-2532.
11. Quere, D., Wetting and roughness. *Ann. Rev. Mater. Res.*, **2008**, 38, 71-99.
12. Li, X. M.; Reinhoudt, D.; Crego-Calama, M., What do we need for a superhydrophobic surface? A review on the recent progress in the preparation of superhydrophobic surfaces. *Chem. Soc. Rev.* **2007**, 36, (8), 1350-1368.
13. Sbragaglia, M.; Peters, A. M.; Pirat, C.; Borkent, B. M.; Lammertink, R. G. H.; Wessling, M.; Lohse, D., Spontaneous breakdown of superhydrophobicity. *Phys. Rev. Lett.* **2007**, 99, (15), 156001.
14. Chen, L. Q., *Micromachined superhydrophobic surfaces* Hong Kong Univ. of Sci. & Technol.: **2009**.
15. Chen, L. Q.; Lee, Y.-K., New dimensionless number for superhydrophobicity study of micron/submicron patterned surfaces. In *23rd IEEE International Conference on Micro Electro Mechanical Systems (MEMS 2010)*, **2010**, 1051-1054.
16. Ausserre, D.; Picard, A. M.; Leger, L., Existence and role of the precursor film in the spreading of polymer liquids. *Phys. Rev. Lett.* **1986**, 57, (21), 2671-2674.
17. Beaglehole, D., Profiles of the precursor of spreading drops of siloxane oil on glass, fused silica, and mica. *J. Phys. Chem.* **1989**, 93, 893-899.
18. de Gennes, P. G., Wetting: statics and dynamics. *Rev. Mod. Phys.* **1985**, 57, (3), 827-863.
19. Hardy, W., The spreading of fluids on glass. *Philos. Mag.* **1919**, 38, 49.
20. Hoang, A.; Kavehpour, H. P., Dynamics of nanoscale precursor film near a moving contact line of spreading drops. *Phys. Rev. Lett.* **2011**, 106, (25), 254501.
21. Kavehpour, H. P.; Ovryn, B.; McKinley, G. H., Microscopic and macroscopic structure of the precursor layer in spreading viscous drops. *Phys. Rev. Lett.* **2003**, 91, (19), 196104.
22. Leger, L.; Erman, M.; Guinetpicard, A. M.; Ausserre, D.; Strazielle, C., Precursor film profiles of spreading liquid drops. *Phys. Rev. Lett.* **1988**, 60, (23), 2390-2393.



23. Morton, K.; Tsui, O. K. C.; Tung, C. K.; Sturm, J. C.; Chou, S. Y.; Austin, R., The anti-lotus leaf effect in nanohydrodynamic bump arrays. *New J. Phys.* **2010**, *12*, 085008.
24. Rühle, M.; Dosch, H.; Mittemeijer, E. J.; Van de Voorde, M. H., *European white book on fundamental research in material science*. Max-Planck-Institut für Metallforschung: Stuttgart, **2001**.
25. Rusanov, A. I., *Kolloidn. Zh.* **1975**, *37*, 678-704.
26. Shanahan, M. E. R., The spreading dynamics of a liquid drop on a viscoelastic solid. *J. Phys. D-Appl. Phys.* **1988**, *21*, (6), 981-985.
27. Shanahan, M. E. R.; Carre, A., Viscoelastic dissipation in wetting and adhesion phenomena. *Langmuir* **1995**, *11*, (4), 1396-1402.
28. White, L. R., The contact angle on an elastic substrate. 1. The role of disjoining pressure in the surface mechanics. *J. Colloid Interface Sci.* **2003**, *258*, (1), 82-96.
29. Hopcroft, M. A.; Nix, W. D.; Kenny, T. W., What is the Young's modulus of silicon? *J. Microelectromech. Syst.* **2010**, *19*, (2), 229-238.
30. Chen, E. J.; Novakofski, J.; Jenkins, W. K.; O'Brien, W. D., Young's modulus measurements of soft tissues with application to elasticity imaging. *IEEE Trans. Ultrason. Ferroelectr. Freq. Control* **1996**, *43*, (1), 191-194.
31. Samani, A.; Bishop, J.; Luginbuhl, C.; Plewes, D. B., Measuring the elastic modulus of ex vivo small tissue samples. *Phys. Med. Biol.* **2003**, *48*, (14), 2183-2198.
32. Sandrin, L.; Tanter, M.; Gennisson, J. L.; Catheline, S.; Fink, M., Shear elasticity probe for soft tissues with 1-D transient elastography. *IEEE Trans. Ultrason. Ferroelectr. Freq. Control* **2002**, *49*, (4), 436-446.
33. Carre, A.; Gastel, J. C.; Shanahan, M. E. R., Viscoelastic effects in the spreading of liquids. *Nature* **1996**, *379*, (6564), 432-434.
34. Carre, A.; Shanahan, M. E. R., Direct evidence for viscosity-independent spreading on a soft solid. *Langmuir* **1995**, *11*, (1), 24-26.
35. Chen, L.; Bonaccorso, E.; Shanahan, M. E. R., Inertial to viscoelastic transition in early drop spreading on soft surfaces. *Langmuir : the ACS journal of surfaces and colloids* **2013**, *29*, (6), 1893-8.
36. Chen, L. Q.; Auernhammer, G. K.; Bonaccorso, E., Short time wetting dynamics on soft surfaces. *Soft Matter* **2011**, *7*, (19), 9084-9089.
37. Shanahan, M. E. R.; Carre, A., Anomalous spreading of liquid drops on an elastomeric surface. *Langmuir* **1994**, *10*, (6), 1647-1649.
38. Chen, L. Q.; Li, Z. G., Bouncing droplets on nonsuperhydrophobic surfaces. *Phys. Rev. E* **2010**, *82*, (1), 016308.
39. Chen, L. Q.; Wu, J.; Li, Z. G.; Yao, S. H., Evolution of entrapped air under bouncing droplets on viscoelastic surfaces. *Colloid Surf. A-Physicochem. Eng. Asp.* **2011**, *384*, (1-3), 726-732.
40. Rioboo, R.; Voue, M.; Adao, H.; Conti, J.; Vaillant, A.; Seveno, D.; De Coninck, J., Drop impact on soft surfaces: beyond the static contact angles. *Langmuir* **2010**, *26*, (7), 4873-4879.
41. Sokuler, M.; Auernhammer, G. K.; Roth, M.; Liu, C. J.; Bonaccorso, E.; Butt, H. J., The softer the better: fast condensation on soft surfaces. *Langmuir* **2010**, *26*, (3), 1544-1547.
42. Lopes, M. C.; Bonaccorso, E., Evaporation control of sessile water drops by soft viscoelastic surfaces. *Soft Matter* **2012**, *8*, (30), 7875-7881.

43. Lopes, M. C.; Bonaccorso, E., Influence of the substrate elasticity on particle deposition patterns from evaporating water-silica suspension droplets. *Soft Matter* **2013**, *9*, 7942-7950.
44. Pericet-Camara, R.; Auernhammer, G. K.; Koynov, K.; Lorenzoni, S.; Raiteri, R.; Bonaccorso, E., Solid-supported thin elastomer films deformed by microdrops. *Soft Matter* **2009**, *5*, (19), 3611-3617.
45. Extrand, C. W.; Kumagai, Y., Contact angles and hysteresis on soft surfaces. *J. Colloid Interface Sci.* **1996**, *184*, (1), 191-200.
46. Pu, G.; Guo, J. H.; Gwin, L. E.; Severtson, S. J., Mechanical pinning of liquids through inelastic wetting ridge formation on thermally stripped acrylic polymers. *Langmuir* **2007**, *23*, (24), 12142-12146.
47. Saiz, E.; Tomsia, A. P.; Cannon, R. M., Ridging effects on wetting and spreading of liquids on solids. *Acta Mater.* **1998**, *46*, (7), 2349-2361.
48. Jerison, E. R.; Xu, Y.; Wilen, L. A.; Dufresne, E. R., Deformation of an elastic substrate by a three-phase contact line. *Phys. Rev. Lett.* **2011**, *106*, (18), 186103.
49. Style, R. W.; Boltyanskiy, R.; Che, Y.; Wettlaufer, J. S.; Wilen, L. A.; Dufresne, E. R., Universal deformation of soft substrates near a contact line and the direct measurement of solid surface stresses. *Phys. Rev. Lett.* **2013**, *110*, 066103.
50. Marchand, A.; Das, S.; Snoeijer, J. H.; Andreotti, B., Capillary pressure and contact line force on a soft solid. *Phys. Rev. Lett.* **2012**, *108*, (9), 094301.
51. Pericet-Camara, R.; Best, A.; Butt, H. J.; Bonaccorso, E., Effect of capillary pressure and surface tension on the deformation of elastic surfaces by sessile liquid microdrops: An experimental investigation. *Langmuir* **2008**, *24*, (19), 10565-10568.
52. Winkels, K. G.; Weijs, J. H.; Eddi, A.; Snoeijer, J. H., Initial spreading of low-viscosity drops on partially wetting surfaces. *Phys. Rev. E* **2012**, *85*, (5), 055301.
53. Chen, L. Q.; Heim, L. O.; Golovko, D. S.; Bonaccorso, E., Snap-in dynamics of single particles to water drops. *Appl. Phys. Lett.* **2012**, *101*, (3), 031601.
54. Biance, A. L.; Clanet, C.; Quere, D., First steps in the spreading of a liquid droplet. *Phys. Rev. E* **2004**, *69*, (1), 016301.
55. Bird, J. C.; Mandre, S.; Stone, H. A., Short-time dynamics of partial wetting. *Phys. Rev. Lett.* **2008**, *100*, (23), 234501.
56. Keller, J. B.; Milewski, P. A.; Vanden-Broeck, J. M., Merging and wetting driven by surface tension. *Eur. J. Mech. B-Fluids* **2000**, *19*, (4), 491-502.
57. Huh, C.; Scriven, L. E., Hydrodynamic model of steady movement of a solid/liquid/fluid contact line. *J. Colloid Interface Sci.* **1971**, *35*, (1), 85-101.
58. Tanner, L. H., The spreading of silicone oil drops on horizontal surfaces. *J. Phys. D-Appl. Phys.* **1979**, *12*, (9), 1473-1484.
59. Cazabat, A. M.; Stuart, M. A. C., Dynamics of wetting: effects of surface roughness. *J. Phys. Chem.* **1986**, *90*, (22), 5845-5849.
60. Lavi, B.; Marmur, A., The exponential power law: partial wetting kinetics and dynamic contact angles. *Colloid Surf. A-Physicochem. Eng. Asp.* **2004**, *250*, (1-3), 409-414.
61. Marmur, A.; Lelah, M. D., The spreading of aqueous surfactant solutions on glass. *Chem. Eng. Commun.* **1981**, *13*, (1-3), 133-143.
62. Blake, T. D.; Haynes, J. M., Kinetics of liquid/liquid displacement. *J. Colloid Interface Sci.* **1969**, *30*, (3), 421-423.
63. S, G.; J., L. K.; H., E., *The theory of rate process*. McGraw Hill: New York, **1941**.

64. Blake, T. D., The physics of moving wetting lines. *J. Colloid Interface Sci.* **2006**, 299, (1), 1-13.
65. Carre, A.; Shanahan, M. E. R., Viscoelastic braking of a running drop. *Langmuir* **2001**, 17, (10), 2982-2985.
66. Muralidhar, P.; Bonaccorso, E.; Auernhammer, G. K.; Butt, H. J., Fast dynamic wetting of polymer surfaces by miscible and immiscible liquids. *Colloid Polym. Sci.* **2011**, 289, (14), 1609-1615.
67. Roth, M.; D'Acunzi, M.; Vollmer, D.; Auernhammer, G. K., Viscoelastic rheology of colloid-liquid crystal composites. *J. Chem. Phys.* **2010**, 132, (12), 124702.
68. Deng, Q.; Anilkumar, A. V.; Wang, T. G., The role of viscosity and surface tension in bubble entrapment during drop impact onto a deep liquid pool. *J. Fluid Mech.* **2007**, 578, 119-138.
69. Vazquez, G.; Alvarez, E.; Navaza, J. M., Surface tension of alcohol water + water from 20 to 50 .degree.C. *J. Chem. Eng. Data* **1995**, 40, (3), 611-614.
70. Wensink, E. J. W.; Hoffmann, A. C.; van Maaren, P. J.; van der Spoel, D., Dynamic properties of water/alcohol mixtures studied by computer simulation. *J. Chem. Phys.* **2003**, 119, (14), 7308-7317.
71. Soboleva, O. A.; Raud, E. A.; Summ, B. D., Initial stage of the spreading of a drop over a solid surface. *Kolloidn. Zh.* **1991**, 53, (6), 1106-1110.
72. Lester, G. R., Contact Angles Of Liquids At Deformable Solid Surfaces. *Journal Of Colloid Science* **1961**, 16, (4), 315-326.
73. Rusanov, A. I., Theory of Wetting of Elastically Deformed Bodies.1. Deformation with a Finite Contact-Angle. *Colloid J. USSR* **1975**, 37, (4), 614-622.
74. Shanahan, M. E. R.; de Gennes, P. G., *Equilibrium of the triple line solid/liquid/fluid of a sessile drop*. Elsevier Applied Science: London, **1987**.
75. White, L. R., The contact angle on an elastic substrate. 1. The role of disjoining pressure in the surface mechanics. *J. Colloid. Interface Sci.* **2003**, 258, (1), 82-96.
76. Kenyon, K. E., Capillary Waves Understood by an Elementary Method. *J. Oceanogr.* **1998**, 54, 343-346.
77. Lamb, H., *Hydrodynamics*. Dover: New York, **1932**.
78. Kenyon, K. E., Capillary waves understood by an elementary method. *J. Oceanogr.* **1998**, 54, 343-346.
79. Courbin, L.; Bird, J. C.; Reyssat, M.; Stone, H. A., Dynamics of wetting: from inertial spreading to viscous imbibition. *J. Phys.-Condes. Matter* **2009**, 21, (46).
80. Duchemin, L.; Eggers, J.; Josserand, C., Inviscid coalescence of drops. *J. Fluid Mech.* **2003**, 487, 167-178.
81. Eggers, J.; Lister, J. R.; Stone, H. A., Coalescence of liquid drops. *J. Fluid Mech.* **1999**, 401, 293-310.
82. Zaghzi, N.; Carre, A.; Shanahan, M. E. R.; Papirer, E.; Schultz, J., A study of spontaneous rubber/metal adhesion. I. The rolling cylinder test. *J. Polym. Sci. Pt. B-Polym. Phys.* **1987**, 25, (11), 2393-2402.
83. Ward, I. M., *Mechanical properties of solid polymers*. Wiley Interscience: New York, **1979**.
84. Claesson, P. M.; Ederth, T.; Bergeron, V.; Rutland, M. W., Techniques for measuring surface forces. *Adv. Colloid Interface Sci.* **1996**, 67, 119-183.
85. Nguyen, A. V.; Pugh, R. J.; Jameson, G. J., *Colloidal particles at liquid interfaces*. Cambridge University Press: Cambridge, **2006**.

86. Philippoff, W., Some dynamic phenomena in flotation. *Trans. Am. Inst. Min. Metall. Eng.* **1952**, 193, (4), 386–390.
87. Pitois, O.; Chateau, X., Small particle at a fluid interface: effect of contact angle hysteresis on force and work of detachment. *Langmuir* **2002**, 18, (25), 9751-9756.
88. Preuss, M.; Butt, H. J., Direct measurement of forces between particles and bubbles. *Int. J. Miner. Process.* **1999**, 56, (1-4), 99-115.
89. Ralston, J.; Fornasiero, D.; Hayes, R., Bubble-particle attachment and detachment in flotation. *Int. J. Miner. Process.* **1999**, 56, (1-4), 133-164.
90. Fletcher, D. C. S. A. M., *Bacterial adhesion: mechanisms and physiological significance*. Plenum: New York, **1985**.
91. Marshall, K. C.; Cruickshank, R., Cell surface hydrophobicity and the orientation of certain bacteria at interfaces. *Archiv Fur Mikrobiologie* **1973**, 91, (1), 29-40.
92. Powelson, D. K.; Mills, A. L., *Appl. Environ. Microbiol.* **1996**, 62, (7), 2593–2597.
93. Schafer, A.; Harms, H.; Zehnder, A. J. B., Bacterial accumulation at the air-water interface. *Environ. Sci. Technol.* **1998**, 32, (23), 3704-3712.
94. Shang, J. Y.; Flury, M.; Deng, Y. J., Force measurements between particles and the air-water interface: Implications for particle mobilization in unsaturated porous media. *Water Resour. Res.* **2009**, 45, W06420.
95. Albijanic, B.; Ozdemir, O.; Nguyen, A. V.; Bradshaw, D., A review of induction and attachment times of wetting thin films between air bubbles and particles and its relevance in the separation of particles by flotation. *Adv. Colloid Interface Sci.* **2010**, 159, (1), 1-21.
96. McGorty, R.; Fung, J.; Kaz, D.; Manoharan, V. N., Colloidal self-assembly at an interface. *Mater. Today* **2010**, 13, (6), 34-42.
97. Hartland, S.; Ramakrishnan, S.; Hartley, R. W., Oscillation of drops and spheres at fluid-liquid interfaces. *Chem. Eng. Sci.* **1975**, 30, (9), 1141-1148.
98. Nguyen, A. V.; Schulze, H. J.; Stechemesser, H.; Zobel, G., Contact time during impact of a spherical particle against a plane gas-liquid interface: Experiment. *Int. J. Miner. Process.* **1997**, 50, (1-2), 113-125.
99. Butt, H. J., A technique for measuring the force between a colloidal particle in water and a bubble. *J. Colloid Interface Sci.* **1994**, 166, (1), 109-117.
100. Ducker, W. A.; Xu, Z. G.; Israelachvili, J. N., Measurements of hydrophobic and DLVO forces in bubble-surface interactions in aqueous solutions. *Langmuir* **1994**, 10, (9), 3279-3289.
101. Fielden, M. L.; Hayes, R. A.; Ralston, J., Surface and capillary forces affecting air bubble-particle interactions in aqueous electrolyte. *Langmuir* **1996**, 12, (15), 3721-3727.
102. Derjaguin, B. V.; Kussakov, M., *Acta Phys. Chim. URSS* **1939**, 10, 386.
103. Kaz, D. M.; McGorty, R.; Mani, M.; Brenner, M. P.; Manoharan, V. N., Physical ageing of the contact line on colloidal particles at liquid interfaces. *Nat. Mater.* **2012**, 11, (2), 138-142.
104. Nikolov, A. D.; Wasan, D. T., A novel method to study particle-air/liquid surface interactions. *Colloid Surf. A-Physicochem. Eng. Asp.* **2004**, 250, (1-3), 89-95.
105. Ally, J.; Kappl, M.; Butt, H. J.; Amirfazli, A., Detachment force of particles from air-liquid interfaces of films and bubbles. *Langmuir* **2010**, 26, (23), 18135-18143.

- 
106. Ally, J.; Vittorias, E.; Amirfazli, A.; Kappl, M.; Bonaccorso, E.; McNamee, C. E.; Butt, H. J., Interaction of a microsphere with a solid-supported liquid film. *Langmuir* **2010**, 26, (14), 11797-11803.
107. Chan, D. Y. C.; Dagastine, R. R.; White, L. R., Forces between a rigid probe particle and a liquid interface - I. The repulsive case. *J. Colloid Interface Sci.* **2001**, 236, (1), 141-154.
108. Dagastine, R. R.; White, L. R., Forces between a rigid probe particle and a liquid interface - II. The general case. *J. Colloid Interface Sci.* **2002**, 247, (2), 310-320.
109. Gillies, G.; Buscher, K.; Preuss, M.; Kappl, M.; Butt, H. J.; Graf, K., Contact angles and wetting behaviour of single micron-sized particles. *J. Phys.-Condes. Matter* **2005**, 17, (9), S445-S464.
110. Gillies, G.; Kappl, M.; Butt, H. J., Direct measurements of particle-bubble interactions. *Adv. Colloid Interface Sci.* **2005**, 114, 165-172.
111. Mate, C. M.; Novotny, V. J., Molecular conformation and disjoining pressure of polymeric liquid films *J. Chem. Phys.* **1991**, 94, (12), 8420-8427.
112. Nguyen, A. V.; Evans, G. M.; Nalaskowski, J.; Miller, J. D., Hydrodynamic interaction between an air bubble and a particle: atomic force microscopy measurements. *Exp. Therm. Fluid Sci.* **2004**, 28, (5), 387-394.
113. Nguyen, A. V.; Nalaskowski, J.; Miller, J. D., A study of bubble-particle interaction using atomic force microscopy. *Miner. Eng.* **2003**, 16, (11), 1173-1181.
114. Nguyen, A. V.; Nalaskowski, J.; Miller, J. D., Bubble-particle interaction measured by atomic force microscopy. *J. Chem. Eng. Jpn.* **2004**, 37, (2), 231-237.
115. Preuss, M.; Butt, H. J., Measuring the contact angle of individual colloidal particles. *J. Colloid Interface Sci.* **1998**, 208, (2), 468-477.
116. Webber, G. B.; Manica, R.; Edwards, S. A.; Carnie, S. L.; Stevens, G. W.; Grieser, F.; Dagastine, R. R.; Chan, D. Y. C., Dynamic forces between a moving particle and a deformable drop. *J. Phys. Chem. C* **2008**, 112, (2), 567-574.
117. Aston, D. E.; Berg, J. C., Quantitative analysis of fluid interface-atomic force microscopy. *J. Colloid Interface Sci.* **2001**, 235, (1), 162-169.
118. Snyder, B. A.; Aston, D. E.; Berg, J. C., Particle-drop interactions examined with an atomic force microscope. *Langmuir* **1997**, 13, (3), 590-593.
119. Hutter, J. L.; Bechhoefer, J., Calibration of atomic-force microscope tips. *Rev. Sci. Instrum.* **1993**, 64, (11), 3342-3342.
120. Ecke, S.; Raiteri, R.; Bonaccorso, E.; Reiner, C.; Deiseroth, H. J.; Butt, H. J., Measuring normal and friction forces acting on individual fine particles. *Rev. Sci. Instrum.* **2001**, 72, (11), 4164-4170.
121. Gibson, C. T.; Watson, G. S.; Myhra, S., Determination of the spring constants of probes for force microscopy/spectroscopy. *Nanotechnology* **1996**, 7, (3), 259-262.
122. Bonaccorso, E.; Butt, H. J., Microdrops on atomic force microscope cantilevers: Evaporation of water and spring constant calibration. *J. Phys. Chem. B* **2005**, 109, (1), 253-263.
123. Haschke, T.; Bonaccorso, E.; Butt, H. J.; Lautenschlager, D.; Schonfeld, F.; Wiechert, W., Sessile-drop-induced bending of atomic force microscope cantilevers: a model system for monitoring microdrop evaporation. *J. Micromech. Microeng.* **2006**, 16, (11), 2273-2280.

- 
124. McGuiggan, P. M.; Grave, D. A.; Wallace, J. S.; Cheng, S. F.; Prosperetti, A.; Robbins, M. O., Dynamics of a disturbed sessile drop measured by atomic force microscopy (AFM). *Langmuir* **2011**, *27*, (19), 11966-11972.
125. Phan, C. A.; Nguyen, A. V.; Evans, G. A., Combining hydrodynamics and molecular kinetics to predict dewetting between a small bubble and a solid surface. *J. Colloid Interface Sci.* **2006**, *296*, (2), 669-676.
126. Quere, D., Inertial capillarity. *Europhys. Lett.* **1997**, *39*, (5), 533-538.
127. Butt, H.-J.; Michael, K., *Physics and chemistry of interfaces*. Wiley-VCH: Germany, **2006**.
128. Crowley, J. M.; Till, H. R.; Radulski, C. A.; Ahuja, S. K., Electrostatic control of flow-induced smearing in the transfer of liquid ink images. *J. Electrostat.* **1997**, *40-1*, 585-590.
129. George, H. F., Electrostatically assisted ink transfer in gravure printing. *ACS Symposium Series* **1982**, (200), 359-370.
130. Berge, B., *C. R. Acad. Sci.* **1993**, *317* (2), 157-163
131. Mugele, F.; Baret, J. C., Electrowetting: from basics to applications. *J. Phys.-Condes. Matter* **2005**, *17*, (28), R705-R774.
132. Quilliet, C.; Berge, B., Electrowetting: a recent outbreak. *Curr. Opin. Colloid Interface Sci.* **2001**, *6*, (1), 34-39.
133. Pollack, M. G.; Fair, R. B.; Shenderov, A. D., Electrowetting-based actuation of liquid droplets for microfluidic applications. *Appl. Phys. Lett.* **2000**, *77*, (11), 1725-1726.
134. Prins, M. W. J.; Welters, W. J. J.; Weekamp, J. W., Fluid control in multichannel structures by electrocapillary pressure. *Science* **2001**, *291*, (5502), 277-280.
135. Weissenborn, P. K.; Pugh, R. J., Surface tension of aqueous solutions of electrolytes: Relationship with ion hydration, oxygen solubility, and bubble coalescence. *J. Colloid Interface Sci.* **1996**, *184*, (2), 550-563.
136. McCleskey, R. B., Electrical conductivity of electrolytes found In natural waters from (5 to 90) degrees C. *J. Chem. Eng. Data* **2011**, *56*, (2), 317-327.
137. Butt, H. J., Electrostatic interaction in scanning probe microscopy when imaging in electrolyte solutions. *Nanotechnology* **1992**, *3*, (2), 60-68.
138. Melcher, J. R.; Taylor, G. I., *Electrohydrodynamics: a review of the role of interfacial shear stresses*. *Annu. Rev. Fluid Mech.* **1969**, *1*, 111-146
139. Saville, D. A., Electrohydrodynamics: the Taylor-Melcher leaky dielectric model. *Annu. Rev. Fluid Mech.* **1997**, *29*, 27-64.
140. Bradford, S. A.; Torkzaban, S., Colloid transport and retention in unsaturated porous media: A review of interface-, collector-, and pore-scale processes and models. *Vadose Zone J.* **2008**, *7*, (2), 667-681.
141. Bird, J. C.; Ristenpart, W. D.; Belmonte, A.; Stone, H. A., Critical angle for electrically driven coalescence of two conical droplets. *Phys. Rev. Lett.* **2009**, *103*, (16), 164502.
142. Ristenpart, W. D.; Bird, J. C.; Belmonte, A.; Dollar, F.; Stone, H. A., Non-coalescence of oppositely charged drops. *Nature* **2009**, *461*, (7262), 377-380.
143. Daub, C. D.; Bratko, D.; Luzar, A., Electric control of wetting by salty nanodrops: molecular dynamics simulations. *J. Phys. Chem. C* **2011**, *115*, (45), 22393-22399.

- 
144. Liu, J.; Wang, M. R.; Chen, S.; Robbins, M. O., Uncovering molecular mechanisms of electrowetting and saturation with simulations. *Phys. Rev. Lett.* **2012**, 108, (21) 216101.
145. Yuan, Q. Z.; Zhao, Y. P., Precursor film in dynamic wetting, electrowetting, and electro-elasto-capillarity. *Phys. Rev. Lett.* **2010**, 104, (24) 246101.
146. Hess, B.; Kutzner, C.; van der Spoel, D.; Lindahl, E., GROMACS 4: Algorithms for highly efficient, load-balanced, and scalable molecular simulation. *J. Chem. Theory Comput.* **2008**, 4, (3), 435-447.
147. Jorgensen, W. L.; Maxwell, D. S.; TiradoRives, J., Development and testing of the OPLS all-atom force field on conformational energetics and properties of organic liquids. *J. Am. Chem. Soc.* **1996**, 118, (45), 11225-11236.
148. Berendsen, H. J. C.; Grigera, J. R.; Straatsma, T. P., The missing term in effective pair potentials. *J. Phys. Chem.* **1987**, 91, (24), 6269-6271.
149. Kalcher, I.; Dzubiella, J., Structure-thermodynamics relation of electrolyte solutions. *J. Chem. Phys.* **2009**, 130, (13) 134507.
150. Allen, M. P.; Tildesley, D. J., *Computer simulation of liquids*. Clarendon Press: Oxford, **1989**.
151. Sedev, R., Electrowetting: electrocapillarity, saturation, and dynamics. *Eur. Phys. J.-Spec. Top.* **2011**, 197, (1), 307-319.
152. Eddi, A.; Winkels, K. G.; Snoeijer, J. H., Short time dynamics of viscous drop spreading. *Phys. Fluids* **2013**, 25, (1) 013102.
153. Segur, J. B.; Oberstar, H. E., Viscosity of glycerol and its aqueous solutions. *Ind. Eng. Chem.* **1951**, 43, (9), 2117-2120.
154. Association, G. P., *Physical properties of glycerine and its solutions*. Glycerine Producers' Association: New York, **1963**.
155. Khossravi, D.; Connors, K. A., Solvent effects on chemical processes. 3. Surface tension of binary aqueous organic solvents. *J. Solut. Chem.* **1993**, 22, (4), 321-330.
156. Chen, L. Q.; Li, C. L.; van der Vegt, N. F. A.; Auernhammer, G. K.; Bonaccorso, E., Initial electrospreeding of aqueous electrolyte drops. *Phys. Rev. Lett.* **2013**, 110, (2) 026103.
157. Legendre, D.; Maglio, M., Numerical simulation of spreading drops. *Colloids and Surfaces A: Physicochem. Eng. Aspects* **2013**, 432 29-37.
158. Carlson, A.; Bellani, G.; Amberg, G., Universality in dynamic wetting dominated by contact-line friction. *Phys. Rev. E* **2012**, 85, (4) 045302.
159. Carlson, A.; Do-Quang, M.; Amberg, G., Modeling of dynamic wetting far from equilibrium. *Phys. Fluids* **2009**, 21, (12) 121701.
160. Carlson, A.; Do-Quang, M.; Amberg, G., Dissipation in rapid dynamic wetting. *J. Fluid Mech.* **2011**, 682, 213-240.
161. Baret, J. C.; Decre, M. M. J.; Mugele, F., Self-excited drop oscillations in electrowetting. *Langmuir* **2007**, 23, (9), 5173-5179.

---

---

## 8 Curriculum Vitae

---

Name: Longquan Chen

Date of Birth: 19/05/1985

Place of Birth: Mianyang, Sichuan Province, China

### Education

09/2010-11/2013 **PhD Study**, Department of Mechanical Engineering, Technische Universität Darmstadt, Germany

09/2007-07/2009 **Master Study**, Department of Mechanical Engineering, Hong Kong University of Science and Technology, Hong Kong

09/2003-07/2007 **Bachelor Study**, Applied Physics, Chongqing University, China

### Working Experience

Since 09/2010 **Research associate** at the Center of Smart Interfaces, Technische Universität Darmstadt, Germany

08/2009 -08/2010 **Research assistant** at the Small Scale Transport & Nonlinear Phenomena Lab, Department of Mechanical Engineering, Hong Kong University of Science and Technology, Hong Kong

09/2007-07/2009 **Research assistant** at the MEMS/NEMS Group, Department of Mechanical Engineering, Hong Kong University of Science and Technology, Hong Kong

### Publication List

*Publications during PhD study*

1. Wang X., Chen L.Q., Bonaccorso E., Venzmer J., “Dynamic Wetting of Hydrophobic Polymers by Aqueous Surfactant and Superspreader Solutions,” *Langmuir*, DOI: 10.1021/la403994y, in press (2013).
2. Chen L.Q., Bonaccorso E., “Electrowetting — From statics to dynamics,” *Adv. Colloid Interface Sci.*, DOI: 10.1016/j.cis.2013.09.007, in press (2013).



- 
3. Geissler A.‡, Chen L.Q.‡, Zhang K, Bonaccorso E., Biesalski M., “Superhydrophobic surfaces fabricated from nano- and microstructured cellulose stearoyl esters,” *Chem. Commun.* **49**, 4962 2013. (‡Authors contributed equally to this work)
  4. Chen L.Q., Bonaccorso E., Shanahan M.E.R., “Inertial to viscoelastic transition in early drop spreading on soft surfaces,” *Langmuir* **29**, 1893 2013.
  5. Chen L.Q., Li C.L., van der Vegt N.F.A., Auernhammer G.K., Bonaccorso E., “Initial electrospreeding of aqueous electrolyte drops,” *Phys. Rev. Lett.* **110**, 026103 2013.
  6. Chen L.Q., Heim L.-O., Golovko D.S., Bonaccorso E., “Snap-in dynamics of single particles to water drops,” *Appl. Phys. Lett.* **101**, 031601 2012.
  7. Chen L.Q., Auernhammer G.K., Bonaccorso E., “Short time Wetting Dynamics on Soft Surfaces,” *Soft Matter* **7**, 9084 2011.
  8. Chen L.Q., Xiao Z.Y., Chan P.C.H., Lee Y.-K., Li Z.G., “A Comparative Study of Droplet Impact Dynamics on a Dual-scaled Superhydrophobic Surface and Lotus Leaf,” *Appl. Surf. Sci.* **257**, 8857 2011.

*Publications before PhD study*

1. Chen L.Q., Wu J., Li Z.G., Yao S.H., “Evolution of entrapped air under bouncing droplets on viscoelastic surfaces,” *Colloids & Surfaces A: Physicochem. Eng. Asp.* **1** 726 2011.
2. Chen L.Q., Wang X., Wen W.J., Li Z.G., “Critical Droplet Volume for Spontaneous Capillary Wrapping,” *Appl. Phys. Lett.* **97** 1 2010.
3. Chen L.Q., Xiao Z.Y., Chan P.C.H., Lee Y.-K., “Static and Dynamic Characterization of Robust Superhydrophobic Surfaces Built from Nano-flowers on Silicon Micro-Post Arrays,” *J. Micromech. Microeng.* **20** 105001 2010.
4. Chen L.Q., Li Z.G., “Bouncing Droplets on Nonsuperhydrophobic Surfaces,” *Phys. Rev. E* **82**, 016308 2010.
5. Chen L.Q., Lee Y.-K., “New Dimensionless Number for Superhydrophobicity Study of Micron/Submicron Patterned Surfaces,” *23<sup>rd</sup> IEEE International Conf. on Micro Electro Mechanical System (IEEE MEMS 2010)*, Hong Kong, pp.1051-1054, 24-28 Jan 2010.

---

6. Chen L.Q., Xiao Z.Y., Chan P.C.H., Lee Y.-K., “Dual-Scaled Superhydrophobic Nano-Flower Surfaces,” *15<sup>th</sup> International Conf. on Solid-State Sensors, Actuators and Microsystem (Transducers 2009)*, Denver, CO, USA, pp.441-444, 21-25 Jun 2009.

### **Conference Presentations**

- 2013.03 the 9<sup>th</sup> Zsigmondy Kolloquium, Meeting of the German Colloid Society, Essen, Germany (Oral)
- 2012.06 the 86<sup>th</sup> ACS Colloid and Surface Science Symposium, Baltimore, USA (Oral)
- 2012.03 the 8<sup>th</sup> Zsigmondy Kolloquium, Meeting of the German Colloid Society, Darmstadt, Germany (Oral)
- 2011.05 the 18<sup>th</sup> Ostwald Kolloquium, Mainz, Germany (Poster)
- 2010.01 the 23<sup>th</sup> IEEE International Conference on Micro Electro Mechanical Systems, Hong Kong (Poster)
- 2009.06 the 15<sup>th</sup> International Conference on Solid-State Sensors, Actuators and Microsystems, Denver, USA (Poster)

### **Awards**

- 2012 **Chinese Government Award for Outstanding Self-financed Students Abroad** (only 489 talents granted all over the world)
- 2005 Outstanding Student of Chongqing University, China
- 2005 **National Scholarship for Academic Excellence, China**
- 2004 – 2006 Outstanding Student Award of College of Mathematics and Physics, Chongqing University, China

### **Academic Services**

- Reviewer for Langmuir, ACS
- Reviewer for Fibers and Polymers, Springer
- Reviewer for Applied Physics A, Springer
- Reviewer for Journal of the Taiwan Institute of Chemical Engineers, Elsevier (JTICE)
- Reviewer for Turkish Journal of Chemistry